

TOWARDS THE NIR DETECTION OF EXOPLANETS

by

Jason James Neal

A thesis submitted in conformity with the requirements  
for the degree of Doctor of Philosophy  
Graduate Department of Departamento de Física e Astronomia  
University of Porto

## **Dedication**

*To Jessica, Timothy, Amelia*

*For always supporting me*

## Acknowledgements

J.J.N. acknowledges support from FCT though the PhD::Space fellowship PD/BD/52700/2014.

This work was financed by FEDER - Fundo Europeu de Desenvolvimento Regional funds through the COMPETE 2020 - Programa Operacional Competitividade e Internacionalização (POCI), and by Portuguese funds through FCT - Fundação para a Ciência e a Tecnologia in the framework of the project POCI-01-0145-FEDER-028953 and POCI-01-0145-FEDER-032113.”

This work was also supported by Fundação para a Ciência e a Tecnologia (FCT) (Portugal) research grants through national funds and from FEDER through COMPETE2020 by the following grants: UID/FIS/04434/2013 & POCI-01-0145-FEDER-007672, PTDC/FIS-AST/1526/2014 & POCI-01-0145-FEDER-016886, and PTDC/FIS-AST/7073/2014 & POCI-01-0145-FEDER-016880.

## **Resumo**

Thesis abstract in Portuguese

## **Abstract**

Thesis abstract

# Todo list

■	read and quote . . . . .	1
■	Figure: example to point to . . . . .	2
■	finish this . . . . .	3
■	Add original caption to 1.2 . . . . .	3
■	Move location / adjust from paper . . . . .	6
■	this section is completed i think . . . . .	8
■	this section is completed i think . . . . .	9
■	FINISH . . . . .	9
■	FINISH . . . . .	9
■	ADAPT THis section to explain the models more generally. Move the usage back to Reduction section . . . . .	9
■	telluric model correction methods original . . . . .	10
■	Look at . . . . .	10
■	a good reference that mentions the uv and optical uses could be good? . . . . .	10
■	. . . . .	12
■	I don't know where I am going with this section. . . . .	13
■	. . . . .	13
■	FIXup this table . . . . .	14
■	fix Figure 3.3 . . . . .	14
■	move . . . . .	14
■	Check if it is mentioned how these get corrected/ if the impact the wavelength solution. . . . .	15
■	Note: Useful information about MIR reduction in the VISIR manual . . . . .	15
■	Reword . . . . .	16
■	Pedro it is my understanding that the ESO pipeline did not exist/was not publicly available when you created DRACS, correct? . . . . .	16
■	is footnote correct "instruments optics" . . . . .	18
■	Check optimal extraction parameters, may have reduced the extraction width by too much?? Need to check changing it. . . . .	20
■	finish this sentence in caption . . . . .	21
■	CHANGE the figure here . . . . .	22
■	check this statement . . . . .	22

█ citation . . . . .	23
█ citation . . . . .	23
Figure: An image of some reduced spectra from eta Tel and Barnard's star??? . . . . .	23
█ fix-up get a good citation, number of lines . . . . .	24
█ paper for harps Th-Ar lines . . . . .	24
█ cite cires manual, and a paper about sky lines? . . . . .	24
Figure: example figures illustrating this method . . . . .	25
Figure: Example of coordinates and the fit. Can I calculate some errors on the polynomial coord fit.	25
█ explain the fit Figure 3.8 . . . . .	26
Figure: Would a table of polynomial wavelength solutions along with errors be any use? . . . . .	27
█ Add pictures of wavelength calibrations . . . . .	27
Figure: Diagram of idea of combined detector fitting? . . . . .	27
Figure: comparison between a Gasgano wavelength solution and the manual one. This has not been done by me before... . . . . .	28
█ See Solene's paper regarding Telluric correction with models and reference spectra . . . . .	28
█ See solenes paper for material here . . . . .	29
█ Expand this section. . . . .	29
█ Should this be more in the introduction? . . . . .	29
Figure: The telluric spectrum around 2 $\mu\text{m}$ showing the 2.1 $\mu\text{m}$ window of low telluric absorption . . . . .	29
█ Add telluric spectra for nIR band? the plot from Molecfit? . . . . .	30
█ Still uneven line coverage on all detectors in this small range . . . . .	30
█ H <sub>2</sub> O corrections . . . . .	30
█ ADAPT this section to the usage of the models. . . . .	30
█ telluric model correction methods original . . . . .	30
█ ADD non-H <sub>2</sub> O fitting corrections. . . . .	32
Figure: Plots showing some examples the telluric correction with and without H <sub>2</sub> O separated . . . . .	32
█ Rotate orbital parameter table. . . . .	34
█ I still assume this is a mistake . . . . .	35
█ Check why the ordering number is incorrect for HD202206. If it is correct like this and is numbered incorrectly in the header then we should mention this. . . . .	35
█ rotate table? . . . . .	35
█ I am not sure if this is the best location for this section. . . . .	35
█ equations for companion rv with the masses still included. include 180 degree angle phase change also . . . . .	36
█ Fix caption position here . . . . .	36
█ recalculate values that are less than 1 . . . . .	36
█ put in advanced concepts chapter??? . . . . .	38
█ this ignores $\gamma$ . . . . .	38
Figure: simulated example of combined binary spectra, and the subtraction, with a clear companion visible . . . . .	38
█ Should I predict when the best time to observe these targets are? e.g. in 2020 x and x will have sufficient RV change in one period to achieve a detection. . . . .	42
█ change RV scale for hd4747 orbit . . . . .	42

■ Fix plot titles . . . . .	42
■ Check M2sini labels - can we get M2 only for those that we know . . . . .	42
■ Should RV of companion be scale by m2sini only or m2 if known? . . . . .	42
■ Increase size of diff amp plots to two . . . . .	46
■ They get a result??? . . . . .	49
■ move . . . . .	49
Figure: includegraphics images/HD211847 example pcolors.pdf . . . . .	55
Figure: includegraphics images/HD211847 example pcolors.pdf . . . . .	55
Figure: images HD211847 result pcolors.pdf . . . . .	59
Figure: images/visualize result residuals.pdf . . . . .	59
Figure: images/inject recovery hd30501.pdf . . . . .	60
Figure: images/chisq shape investigation sigmas.pdf . . . . .	60
■ finish this line . . . . .	64
■ Try cross correlation at a different wavelength 2.3 micron? . . . . .	64
■ Try cross correlation with much larger wavelength range. 50, 100, 600, 1000 nanometres? . . . . .	64
■ Try my simulations with much larger wavelength range. 50, 100, 600 nanometres? . . . . .	64
■ rv method . . . . .	65
■ Check mission statements for these . . . . .	65
■ For example from Figueira 2016 see figure . . . . .	65
Figure: An example from Figueira et al. 2016 . . . . .	65
■ History of Precision calculations . . . . .	66
■ Change picture spectral range to capital lambda $\Lambda$ . . . . .	67
■ Change picture spectral range . . . . .	68
■ Finish this equation (9 of bouchy 2001) . . . . .	68
■ Try the symbolic package from PC . . . . .	68
■ finish this . . . . .	70
■ Does spectrograph pipelines such as HARPS use these equations to measure estimate/precision? . . . . .	70
■ It is convenient to use this version when comparing observed spectra with different S/N.? . . . . .	70
■ define fwhm0 . . . . .	71
■ CHECKTHISRESULT!!!!!! . . . . .	71
Figure: Example of CARMENES spectra before and after correction . . . . .	72
■ Add figure here . . . . .	73
■ Add figure here . . . . .	73
■ finish this . . . . .	73
■ works of software testing in research. . . . .	76
■ add conclusions not affected . . . . .	77
Figure: uncomment this one . . . . .	79
■ cite the equation when I refer to it . . . . .	82
■ Check this if it is previous . . . . .	82
■ weighted sum equation . . . . .	82
■ Should I show the working of analytical working out of this in an appendix, or here? . . . . .	82
■ did I check this was equivalent . . . . .	83
■ put this some where . . . . .	83

■ put this line elsewhere . . . . .	83
■ is this needed . . . . .	84
■ Check how to cite priv communication properly . . . . .	85
■ Inlcude correct links . . . . .	85
■ NIR analysis work . . . . .	87
■ Precision table needs fixed up . . . . .	88
■ Maybe transpose Table A.1 to be shorter? . . . . .	89
■ CHANGE # into the ESO identification number 1b 2a etc . . . . .	89
■ Is this significant?? . . . . .	89
■ is detector two significant as well? . . . . .	89
■ THESE need to be properly selected and a caption given, one without any artefacts also? . . . . .	89
■ Style needs to be tweaked also . . . . .	89
■ change scale on delta flux of HD 162020-2 chip 1 (it is too large atm) . . . . .	89
Figure: Corner plot of single detector? . . . . .	95
Figure: Corner plot fixed gaps . . . . .	95
Figure: Corner plot variable gaps . . . . .	95
■ remove vertical lines . . . . .	95
■ fill in table . . . . .	95
Figure: Residuals between individual fitting and the variable gap fits . . . . .	95
■ Fix up at end . . . . .	97

# Contents

<b>Todo list</b>	<b>vi</b>
<b>List of Tables</b>	<b>xiii</b>
<b>List of Figures</b>	<b>xv</b>
<b>1 Introduction</b>	<b>1</b>
1.1 Main Section 1 . . . . .	1
1.1.1 Subsection 1 . . . . .	1
1.1.2 Subsection 2 . . . . .	1
1.2 Main Section 2 . . . . .	1
1.3 Recent detections in Companion spectra. . . . .	1
1.3.1 model fitting transit stars (not actual title, more other similar methods) . . . . .	1
1.3.2 Earths atmosphere . . . . .	2
1.4 Paper Introduction . . . . .	3
<b>2 Advanced Concepts</b>	<b>6</b>
2.0.1 RV calculation . . . . .	6
2.1 Estimating Companion-host Flux ratio . . . . .	7
2.1.0.1 Baraffe tables . . . . .	8
2.1.1 Companion K . . . . .	9
2.2 Synthetic models . . . . .	9
2.2.1 PHOENIX-ACES . . . . .	9
2.2.2 BT-Settl . . . . .	9
2.2.3 Telluric models . . . . .	9
2.2.3.1 TAPAS . . . . .	9
2.2.4 Tapas models . . . . .	9
2.2.4.1 Vacuum wavelengths . . . . .	10
2.2.5 Differential techniques . . . . .	11

<b>3 NIR spectroscopic reduction</b>	<b>12</b>
3.1 Summary of dataset . . . . .	12
3.2 NIR spectroscopy . . . . .	12
3.2.1 General reduction Concepts . . . . .	13
3.2.1.1 Dark Current . . . . .	13
3.2.1.2 Flat-field . . . . .	13
3.2.1.3 Nodding and Jitter . . . . .	14
3.2.2 Th-Ar lamp calibration . . . . .	15
3.2.3 Extraction . . . . .	15
3.3 Pipeline Comparison . . . . .	16
3.3.1 ESO CRIRES pipeline . . . . .	17
3.3.2 DRACS . . . . .	17
3.3.3 Pipeline comparison and selection . . . . .	18
3.3.3.1 Reduction issues . . . . .	20
3.3.4 Reduction experience: . . . . .	23
3.4 Post reduction stages . . . . .	23
3.4.1 Wavelength calibration . . . . .	24
3.4.1.1 Telluric correction . . . . .	28
3.4.2 Tapas models . . . . .	30
3.4.3 Issues with TAPAS . . . . .	30
3.4.3.1 Telluric masking . . . . .	31
3.4.4 Wavelength masking . . . . .	31
3.4.5 Barycentric correction . . . . .	32
<b>4 Direct Spectral Recovery</b>	<b>33</b>
4.1 Motivation . . . . .	33
4.2 Motivation and target selection . . . . .	33
4.2.1 The Data . . . . .	35
4.2.2 CRIRES data . . . . .	35
4.2.3 Calculations using observed times . . . . .	35
4.3 Direct Subtraction Method . . . . .	36
4.3.1 Results of spectral differential analysis . . . . .	39
4.4 Orbital Solutions . . . . .	40
4.4.1 Relative differential amplitude . . . . .	46
4.4.1.1 Differential scheduling challenges copy from paper . . . . .	48
4.5 Direct recovery in the mIR . . . . .	48
4.6 Summary . . . . .	49
<b>5 Spectral Companion Recovery</b>	<b>50</b>
5.1 Main Section 1 . . . . .	50
5.2 Binary synthetic spectral recovery . . . . .	50
5.2.1 Synthetic PHOENIX-ACES models . . . . .	50
5.2.2 $\chi^2$ method . . . . .	51
5.2.3 Computed model spectra . . . . .	52

5.2.3.1	Single component model . . . . .	52
5.2.3.2	Binary model . . . . .	53
5.2.3.3	Effective radius . . . . .	53
5.2.4	Re-normalization . . . . .	54
5.2.5	Reducing parameters . . . . .	54
5.3	Results . . . . .	55
5.3.1	Simulated binaries . . . . .	56
5.3.2	HD211847 observation . . . . .	57
5.3.3	Companion injection-recovery . . . . .	59
5.3.4	Junk from paper about BT-settl . . . . .	62
5.3.5	Incremental changes . . . . .	64
5.3.6	Note about a target - discussion of results . . . . .	64
5.3.6.1	Wavelength range . . . . .	64
<b>6</b>	<b>NIR information</b>	<b>65</b>
6.1	Overview . . . . .	65
6.2	Radial velocity precision . . . . .	66
6.2.1	Fundamental photon noise limitation . . . . .	66
6.2.2	Prepare phoenix aces models . . . . .	70
6.2.3	Rotation convolution . . . . .	70
6.2.4	Instrumental Convolution . . . . .	71
6.2.5	Numerical Convolution . . . . .	71
6.3	. . . . .	72
6.3.1	Bands . . . . .	73
6.3.2	Comparing models to CARMENES. . . . .	73
6.4	Metallicity NaN effects . . . . .	74
6.5	Updating RV precision software . . . . .	76
6.5.1	Automated testing . . . . .	76
6.5.2	Atmospheric masking bug . . . . .	76
6.5.3	Performance . . . . .	77
6.5.4	Model extension . . . . .	77
6.6	Numerical Gradient . . . . .	77
6.6.1	Masking Function . . . . .	81
6.6.1.1	Masking order . . . . .	82
6.6.2	SNR scaling . . . . .	83
6.7	SPIRou and NIRPS ETC . . . . .	84
<b>7</b>	<b>Conclusions</b>	<b>86</b>
7.1	Conclusions from Paper . . . . .	86
7.2	Future Work . . . . .	87
<b>A</b>	<b>Artefacts in Optimal Extraction</b>	<b>89</b>
<b>B</b>	<b>Multi-dectector wavelength calibration</b>	<b>95</b>

<b>C PhD output</b>	<b>97</b>
C.1 Publications . . . . .	98
C.2 Talks and Seminars . . . . .	102
C.3 Posters . . . . .	103
C.4 Attended Conferences and Schools . . . . .	106
C.5 Outreach . . . . .	108
C.6 Other . . . . .	109
<b>Bibliography</b>	<b>110</b>

# List of Tables

2.1	Estimated flux ratios given the companion mass ( $M_2$ or $M_2 \sin i$ ) from Table 4.2. . . . .	8
4.1	Stellar parameters of the host stars. V is the apparent magnitude taken from SIMBAD (Wenger et al., 2000). Distances were calculated from the GAIA DR2 parallax measurements. . . . .	34
4.2	Orbital parameters for the BD companions obtained from the literature. <b>Yes need rotating.</b> . . . . .	34
4.3	Details about the each CRIRES observation. The number of artefacts removed in Section 3.3.3.1 as well as the SNR of the combined spectra is provided. The last three columns are the calculated RV of both host and largest companion, from the orbital solution, as well as the RV difference between the two components. . . . .	36
4.4	Estimated orbital semi-amplitude and RV separation of the companion, given the companion mass ( $M_2$ or $M_2 \sin i$ ) from Table 4.2 and observation times from Table 4.3. . . . .	37
5.1	Full parameter space of the PHOENIX-ACES spectral grid. . . . .	51
5.2	Input and recovered parameters on simulations and an observation when applying a single ( $C^1$ ) and binary ( $C^2$ ) models. The $\log g$ and metallicity were fixed at $\log g_1 = 4.50$ , $\log g_2 = 5.0$ and $[Fe/H]=0.0$ equally for both components. Gaussian noise was added to both simulations with a SNR of 150. Here $m$ and $n$ are the number of data points and parameters used in each model. . . . .	55
5.3	Upper mass limits of target companions assuming a companion $\log g=5.0$ . Masses are derived from Baraffe et al. (2015) evolutionary models using $T_{\text{eff}}$ and $\log g$ . The flux ratio $F_2/F_1$ is the absolute flux ratio between the cut-off temperature and the target host star. . . . .	62
6.1	The wavelength ranges of the nIR spectral bands. . . . .	73
6.2	CARMENES library target selection spanning the M-Dwarf spectral range. . . . .	73
6.3	csv2tex table . . . . .	73

6.4 The affect of the numerical gradient function on RV precision. The band label VIS and NIR indicate the full visible and nIR bands while CARM <sub>VIS</sub> and CARM <sub>NIR</sub> indicate the two wavelength bands of the CARMENES spectrograph. $\Delta\lambda$ is a wavelength shift applied to move the FFD values between pixels for this comparison only. The M0 spectra used here had no rotation, or instrument broadening preformed and was normalized to a maximum of 1 in each band. The precision values given here are for accessing the relative precision change due to the different gradient methods. . . . .	80
6.5 Relative RV precision difference for Condition #2 due to spectral splitting and order of applying the pixel mask. The ratio are the difference between Split and Masked implementations with the same gradient calculation. The last column is the ratio between the Masked versions using the FFD and numpy gradient methods and are consistent with Table 6.4. Results a for an M0 spectral type, with $v \sin i = 1.0$ and R=100 000. . . . .	83
A.1 Identification of all the optimally reduced nod spectra which had artefacts that were replaced by the rectangular extractions, corrected for bad pixels. The numbers represent the position in the nod cycle ABBAABBA. The number of the observation for each target is given by #. . . . .	90
A.2 Tally of nod cycle positions in which their optimally reduced spectra were affected and were replaced. . . . .	90
B.1 Example fitting parameters obtained for HD30501 observation 2 under different scenarios.	96

# List of Figures

1.1	M-R relationship Chen and Kipping (2016) . . . . .	2
1.2	Reproduction of Figure 1 of Smette et al. (2015) showing telluric absorption form 0.30 μm. Original caption: . . . . .	4
2.1	By Lasunncty at the English Wikipedia, CC BY-SA 3.0, <a href="https://commons.wikimedia.org/w/index.php?curid=8971">https://commons.wikimedia.org/w/index.php?curid=8971</a>	
3.1	Master dark frames for exposure times of 3 and 180 seconds. Each master is created by averaging 3 images in which the detector received no incident light. Both frames are on the same scale and show dark current grows with exposure time. The colour has been inverted so that black is the recorded measurement. . . . .	13
3.2	A flat-field image for detector #2 before (left) and after (right) the non-linearity corrections are performed. . . . .	14
3.3	Illustration of the nodding technique. Left: Sample slice of successive images at nod positions A and B, and their difference A-B for detector #1. Right: A vertical slice along the slit at column 512 (middle of detector). The background level observed in A and B is effectively removed by the subtraction. . . . .	15
3.4	Example Th-Ar calibration lamp frames for each detector. These are the raw frames in which dark current correction has not been performed (i.e the dark current is still visible on the bottom corners). . . . .	16
3.5	Comparison between the ESO pipeline and DRACS pipeline. For two observations HD30501-1 and HD202206-1. The blue lines are the extracted spectra from the ESO pipeline, the orange dashed lines are the optimal extraction from the DRACS pipeline, while the green dash-dotted line is the DRACS extraction after dealing with artefacts in the optimal extraction addressed in Section 3.3.3.1. The wavelength information applied to the spectra here comes from the ESO pipeline. . . . .	19
3.6	DRACS reduction of HD202206-1 detector 2 with a single pipeline parameter changed. Left: Pipeline with the “doslit.resize” set to “no”. Right: The same but with “doslit.resize” set to “yes”. During the order tracing the aperture size is automatically adjusted but the <b>finish this sentence</b> . Setting the resize parameter for <b>apextract?</b> . Changing this one parameter removed one large artefact but kept the other. One large artefact is removed, one is not. . . . .	21

3.7 Example of an artefact in the optimally extracted spectra from detector #2 of HDXXXXXX.	22
The top panel contains the 8 normalized nod spectra obtained using optimal extraction. The middle panel shows nod spectra using only rectangular extraction. The bottom panel shows the difference between a combined spectrum using optimal nods only and a combined spectrum in which the identified nods are replaced with their rectangular counterparts as per Section 3.3.3.1. A vertical offset is included between each spectra for clarity. The nod spectra are in observation order from top to bottom. . . . .	22
3.8 Wavelength calibration example. The equation of the fitted line for these points is $\lambda = -1.85e^{-7}x^2 + 1.16e^{-2}x + 2111.86$ with each coefficient shown to two decimal places only. Error bars the line width set to around 0.04 nm. . . . .	26
3.9 An example spectra for each target and each detector 1–4 in order of increasing wavelength. The solid lines are the spectra while the black dashed lines are the telluric models used for wavelength correction, showing good alignment with the spectra. . . . .	28
4.1 (Top) A reduced CRIRES observation of HD 30501 (blue) for detector 1 between 2 112–2 124 nm along with the tapas telluric absorption model (orange dashed) used for the wavelength calibration and telluric correction. (Middle) The telluric corrected spectra. (Bottom) (blue) Differential spectra for HD 30501 between observations 1 and 3. (orange dashed) Simulated “perfect” differential using PHOENIX-ACES spectra with parameters $T_{\text{eff}} = 2\,500$ K, $\log g = 5.0$ , and $[\text{Fe}/\text{H}] = 0.0$ , with the same $\Delta RV$ as the observations. The shaded regions indicate where the telluric green and host star blue spectra are > 4% deep. . . . .	41
4.2 RV orbital single companion Keplerian for the HD 4747. The left hand plot shows the RV curve for one full orbit while the right hand panel shows the RV curve over 6 months (Period 89). The solid black line indicates the RV of the host star (with scale on the left), while the blue dashed line indicates the RV of the companion (with scale on the right axis). The orange crosses and red stars indicate the times at which observations were obtained for the target, for the host and companion respectively. . . . .	42
4.3 Same as Figure 4.2 but for HD 162020. . . . .	43
4.4 Same as Figure 4.2 but for HD 167665. . . . .	43
4.5 Same as Figure 4.2 but for HD 168443b. Analysed as if this was a single companion. . . .	43
4.6 Same as Figure 4.2 but for HD 168443c. Analysed as if this was a single companion. . . .	44
4.7 Same as Figure 4.2 but for HD 202206B. Analysed as if this was a single companion. . . .	44
4.8 Same as Figure 4.2 but for HD 202206c. Analysed as if this was a single companion. . . .	44
4.9 Same as Figure 4.2 but for HD 211847. . . . .	45
4.10 Same as Figure 4.2 but for HD 30501. . . . .	45

4.11 Simulated relative amplitude of differential spectra at different companion  $\Delta RV$  separations revealing the diminished amplitude at very small orbital separations. The solid blue line shows the maximum relative amplitude of the differential signal (from a shifted copy of itself) of a PHOENIX-ACES spectrum with  $T_{\text{eff}} = 2500 \text{ K}$ ,  $\log g = 5.0$ ,  $[\text{Fe}/\text{H}] = 0.0$  in the wavelength region  $2110\text{--}2123 \text{ nm}$ . The maximum difference is normalized by the median amplitude between  $\pm 7\text{--}10 \text{ km s}^{-1}$ , representing a complete line separation. The orange (dashed) and green (dot-dashed) lines represent the relative amplitude of a differential spectrum of a spectrum containing a single Gaussian and single Lorentzian absorption line respectively, each with a unitary amplitude and a  $\text{FWHM} = \lambda/R$ . The solid vertical lines indicate the estimated companion  $\Delta RV$  in these observations while the dashed vertical lines indicate the RV corresponding to the FWHM at this wavelength and resolution. . . . . 47

- 5.1  $\chi^2$  results for companion recovery of a simulated binary observation of a Sun-like star ( $T_{\text{eff}1} = 5800 \text{ K}$ ) with an M-dwarf companion ( $T_{\text{eff}2} = 4000 \text{ K}$ ). The top right plot shows the application of a single component model ( $C^1$ ) while the other three are using a binary model ( $C^2$ ). Both left hand panels show the distribution of host temperature and host RV. The top right panel shows the distribution for host and companion temperature, and the bottom right the companion temperature and radial velocity. The red circle and yellow star indicate the location of the simulation input and recovered parameters respectively. The white line shows a  $3\sigma$  confidence level about the minimum  $\chi^2$  solution grid point. Each box is centred on the parameter values and shows the grid resolution. . . . . 56
- 5.2 Similar to Figure 5.1,  $\chi^2$  results for companion recovery of a simulated binary observation similar to HD 211847, ( $T_{\text{eff}1} = 5800 \text{ K}$ ,  $T_{\text{eff}2} = 3200 \text{ K}$ ). The top right plot shows the application of a single component model ( $C^1$ ) while the other three are using a binary model ( $C^2$ ). Both left hand panels show the distribution of host temperature and host RV. The top right panel shows the distribution for host and companion temperature, and the bottom right the companion temperature and radial velocity. The red circle and yellow star indicate the location of the simulation input and recovered parameters respectively. The white line shows a  $3\sigma$  confidence level about the minimum  $\chi^2$  solution grid point. Each box is centred on the parameter values and shows the grid resolution. . . . . 56
- 5.3  $\chi^2$  result grid for observation 2 of HD 211847, similar to Figs. 5.1 and 5.2. The top right plot shows the application of a single component model ( $C^1$ ) while the other three are using a binary model ( $C^2$ ). Both left hand panels show the distribution of host temperature and host RV. The top right panel shows the distribution for host and companion temperature, and the bottom right the companion temperature and radial velocity. The red circles indicate the literature values or calculated parameters for the target while the yellow star indicates the minimum  $\chi^2$  solution. The error bar on the  $T_{\text{eff}1}$  is from the literature while the error bars on  $rv_1$  and  $rv_2$  are calculated by propagating the orbital parameter uncertainties through the radial velocity equation. The white line shows a  $3\sigma$  confidence level about the minimum  $\chi^2$  solution grid point, not always visible here due to the large  $\chi^2$  values. . . . . 59

5.4 Comparison between the observed HD 211847 spectrum (blue) and the best fit synthetic binary model (orange dashed) for each detector. The bottom section of each panel shows the residuals between the parts of the observation used in the $\chi^2$ fit and recovered binary model ( $O - C^2$ ) in purple. The red dashed line shows the difference between the recovered binary model and the binary model with the exact same parameters except for the estimated companion temperature of 3 200 K ( $C^2[3200\text{K}] - C^2$ ). The grey shading indicated the wavelength regions where masking has been applied. The thinner masked regions that match with cuts in the observed spectra are where the centres of deep (>5%) telluric lines that have been masked out are. . . . .	59
5.5 Result of simulated injection-recovery of synthetic companions on HD 30501. The blue dots and orange triangles indicate the recovered companion temperature for the observed and synthetic spectra respectively. The $\pm 100\text{ K}$ error bars are the grid step of the synthetic models. The black dashed diagonal shows the 1:1 temperature relation. The grey shaded region indicates the $\pm 1\,000\text{ K}$ temperature range explored. Gaussian noise added to the synthetic spectra was derived from the observed spectra. . . . .	61
5.6 (top) Companion temperature verses $\chi^2$ for simulations with different injected companion temperatures. Other fixed parameters for these fully synthetic simulations was $T_{\text{eff}1} = 5\,200\text{ K}$ , $\log g_1 = 4.5$ , $\log g_2 = 5.0$ , and both $[\text{Fe}/\text{H}] = 0.0$ . A fixed Gaussian noise corresponding to a SNR of 300 was used. (bottom) A close up view of $\chi^2 < 15$ . The three horizontal grey lines indicate the 1, 2, 3 sigma with 2 degrees of freedom. The vertical dotted lines indicate the location of the minimum $\chi^2$ recovered for each companion. The black solid vertical in both panels shows the 2 300 K cut-off of the PHOENIX-ACES models	61
6.1 Mass of discovered planets verse year. From Exoplanet.eu . . . . .	66
6.2 Arbitrary spectral line with a shift $\delta\lambda$ , inspired by Connes (1985). $\Lambda$ is the wavelength range considered. . . . .	67
6.3 Quality factor changes across spectral type and bands for variations in $[\text{Fe}/\text{H}]$ and NaN. Broadening values are $R=100\,000$ and $v \sin i = 1.0\text{ km s}^{-1}$ . Top: Quality factor variation of $[\text{Fe}/\text{H}]$ between -1.0 to 1.0 at a fixed NaN=4.5. Bottom: Quality factor variation of NaN between 4 and 5.5 with fixed $[\text{Fe}/\text{H}] = 0.0$ . Note a higher quality factor corresponds to an increased RV precision. . . . .	75
6.4 Visualization of the numerical gradient of some spectral lines. Top: The two spectral regions of a stellar spectrum the left hand slide contains short lines near the normalized continuum while on the right a single deep absorption line is shown. Bottom: The numerical gradients for the spectra shown in the top panels; the original FFD method is displayed with <i>blue squares</i> while numpy gradient is shown with <i>green stars</i> . The <i>orange circles</i> are the FFD version shifted to the mid-points between pixels for illustrative purposes. . . . .	80

A.1 Artefact example for the second detector of HD 4747. The top panel contains the eight normalized nod spectra obtained using optimal extraction. The middle panel shows nod spectra using only rectangular extraction. The bottom panel shows the difference between a combined spectrum using optimal nods only and a combined spectrum in which the identified nods are replaced with their rectangular counterparts as per Section 3.3.3.1. A vertical offset is included between each spectra for clarity. The nod spectra are in observation order from top to bottom. In this example there are artefacts in the 5th (purple) and eighth (grey) nod spectra around 700 and 500 pixels respectively. . . . .	91
A.2 Same as Figure A.1 but for the first detector of the second observation of HD 162020. In this example there are several large spikes observed in the rectangular extraction but they do not appear to effect the optimally extracted nods. <b>reduce scale of delta flux (to large atm)</b> . . . . .	92
A.3 Same as Figure A.1 but for the third detector of the second observation of HD 167665. In this example a small spike in the first spectrum (blue) around pixel 450 causes a extended dip in the optimally extracted nod. . . . .	92
A.4 Same as Figure A.1 but for the 1st detector of the second observation of HD 202206. In this example there are several large spike but only one produces an artefact. This is on the 5th nod (purple) around pixel 800. . . . .	93
A.5 Same as Figure A.1 but for the fourth detector of the first observation of HD 168443. In this example a barely visible spike on the 7th nod (pink) causes a deviation in the optimal nod around pixel 610. There is also a second small spike on the eighth nod (grey) around pixel 850, between two spectral lines. . . . .	93
A.6 Same as Figure A.1 but for the second detector of the second observation of HD 211847. In this example two large spikes around 800 and 1000 in the 7th nod (pink) create large deviations in the optimally reduced spectra. A spike in the first nod (blue) around pixel 700 also causes a bump. There is also some extra noise in the first nod around pixel 350. .	94
A.7 Same as Figure A.1 but for the second detector of the second observation of HD 30501. In this example there are artefact causing spikes in four places. The second nod (orange) around pixel 950, the 6th nod (brown) around pixel 20 and two spikes in the 7th nod (pink) around pixels 400 and 550. . . . .	94

## Abbreviations

CARMENES	Calar Alto high-Resolution search for M dwarfs with Exoearths with Near-infrared and optical Échelle
CFHT	Canada France Hawaii Telescope
CRIRES	CRyogenic high-resolution InfraRed Échelle Spectrograph
ETC	Exposure Time Calculator
E-ELT	European-Extremely Large Telescope
ESO	European Southern Observatory
ESPRESSO	Échelle SPectrograph for Rocky Exoplanet and Stable Spectroscopic Observations
FIRST	Florida InfraRed Silicon immersion grating spectromeTer
HET	Hobby-Eberly Telescope
HPF	Habitable Planet Finder
IR	Infrared
JWST	James Web Space Telescope
MIR	Mid-Infrared
MIRI	Mid-Infrared Instrument
NASA	National Aeronautics and Space Administration
nIR	Near-Infrared
SPIRou	SpectroPolarimètre Infra-Rouge
Th-Ar	Thorium-Argon
TMT	Thirty Meter Telescope
TNG	Telescopio Nazionale Galileo
VISIR	VLT spectrometer and imager for the mid-infrared
VLT	Very Large Telescope

## Physical Constants

Speed of Light       $c_0 = 2.997\,924\,58 \times 10^8 \text{ m s}^{-1}$  (exact)

Astronomical Unit    AU =  $\sim 150$  million km

$M_{Jup}$                 =

$M_\odot$                 =

$R_\odot$                 =

## List of Symbols

$a$	distance	m
$P$	power	W ( $\text{J s}^{-1}$ )
$\lambda$	wavelength	nm
$S_{tel}$	telescope collecting area	$\text{cm}^2$
$N_{e^-}$	number of photoelectrons	
$P_{avg}$	average monochromatic stellar brightness	$\text{photons s}^{-1} \text{cm}^{-2} \text{cm}^{-1}$
$T_{\text{exp}}$	exposure time	s
$\Lambda$	wavelength range	nm

# Chapter 1

## Introduction

### 1.1 Main Section 1

MR relation ship image arXiv:1506.05097 Chen and Kipping (2016)

Santos et al 2017

read and quote

#### 1.1.1 Subsection 1

#### 1.1.2 Subsection 2

### 1.2 Main Section 2

Spectral Disentangling techniques - PSOAP - Differencing Fruluga - Templates?

2D-cross-correlation? piskorz 2016

### 1.3 Recent detections in Companion spectra.

Birkby

#### 1.3.1 model fitting transit stars (not actual title, more other similar methods)

There are other situations in which to determine the presence of faint secondary spectra, such as identifying the presence of any background or companion stars of transiting planet candidates. Many astronomical phenomena such as grazing eclipsing, a giant primary star eclipsed by a dwarf or a background star can produce signals indistinguishable from planetary transits. Efforts to characterize the false positive probability (FPP) among Kepler planet candidates is as high as  $\sim 35\%$  (Santerne et al., 2012). The presence of unknown companions or background stars decreases the dimming effect from the planet transit leading to smaller planetary radius. Where multiple stars are present there may also be ambiguity on which star hosts the planet. Kolbl et al. (2015) developed a method for detecting the presences of faint secondary lines in optical stellar spectra by matching observations to the SpecMatch library of stellar

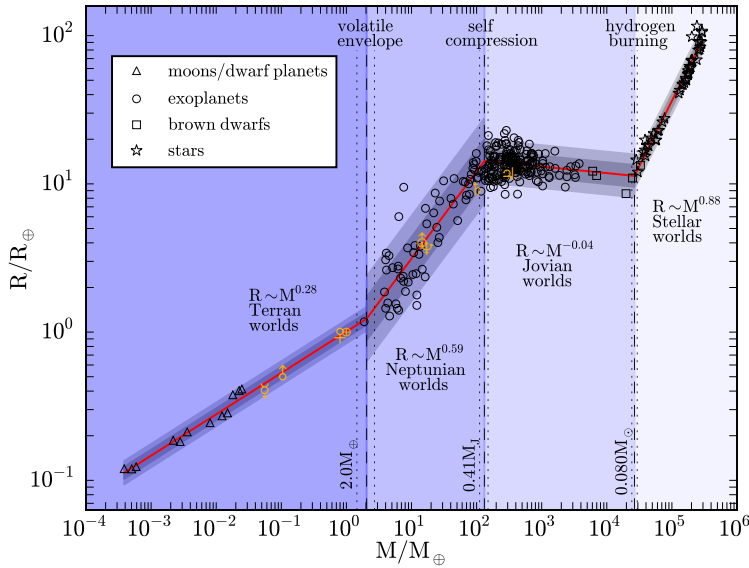


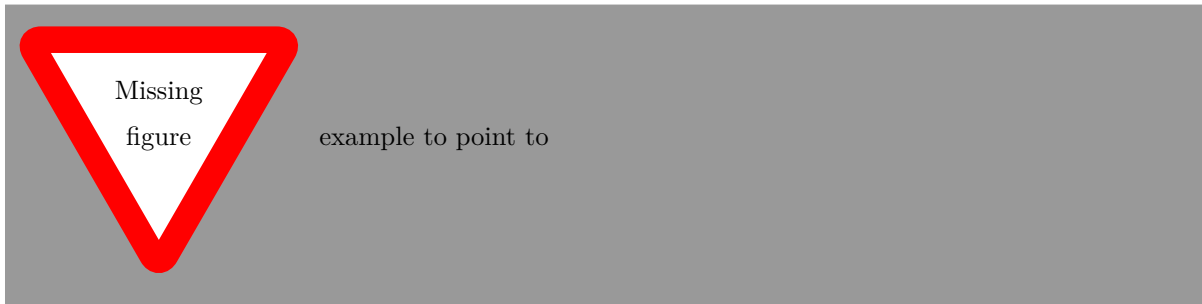
**Figure 1.1:** M-R relationship Chen and Kipping (2016)

spectra. Identifying the spectroscopic evidence of a secondary star for 63/1 160 California *Kepler* Survey objects of Interest (KOI).

For transiting planets, the presence of a background star or a companion star causes problems in characterizing the planet. Being able to detect spectra signal of the a faint second spectra in double-lined spectroscopic binaries. For example eclipsing binaries, A dim binary system companion or a giant planet around a background star can mimic the transit of a small Earth-like planet on a foreground star.

### 1.3.2 **Earths atmosphere**

While the Earth's atmosphere is important for an Astronomer's lungs, it can be a nuance for their ground-based observations. As light from astronomical sources passes through the atmosphere, its molecular components absorb some of the light, changing spectral components observed by imprinting a transmission spectrum of our atmosphere. The H<sub>2</sub>O absorption is a key example as it defines the photometric and spectroscopic bands in the nIR.



The correction of observations from the contamination of Earth's atmosphere is a complex process. The transmission is variable on many different time scales, the water vapour change is rapid, concentrations

of atmospheric constituents, to seasonal and longer. Such as the increase in atmospheric CO<sub>2</sub> causing anthropomorphic climate change this requires 6% change to CO<sub>2</sub> line depths since 2000 Molecfit paper? There is also variation with airmass, which depends on the observation angle in the sky and changes as targets move across the sky during the night.

other constituents, CO, CO<sub>2</sub>, CH<sub>4</sub> . . . , angle of observations.

An important consideration in the detecting the constituents of planetary atmospheres is the characterization and removal of Earths telluric lines.

e.g. 50% error in CO<sub>2</sub> detection on Mars atmosphere

Recently Ulmer-Moll et al. (2018) compared the telluric correction possible from three different synthetic telluric software against the standard star model. Molecfit, a software from ESO was the most.

This is a growing field and there are other software available too...

Water vapour content has rapid variability. Works such as Snellen 2011, . . . . model the telluric variation during observations to remove telluric lines and detect planetary lines.

[finish this](#)

Telluric absorption map

[Add original caption to 1.2](#)

## 1.4 Paper Introduction

Brown dwarfs (BDs) are sub-stellar objects unable to achieve hydrogen fusion, with masses around 13 – 80 M<sub>Jup</sub> (Chabrier and Baraffe, 2000), bridging the gap between low-mass stars and giant planets. Without sustained fusion, brown-dwarfs cool down over time with an age-dependent cooling rate. Therefore, there is an inherent degeneracy between the mass, age and luminosity of a given BD(Burrows et al., 1997). This degeneracy may be broken by observation of several parameters, for instance when a BD is in a binary system with a main sequence host star, using both the host stars age and the masses derived from the dynamical motion.

A paucity of BD companions exists in short period orbits around Sun-like stars ( $\lesssim 5$  AU), compared to stellar or planetary companions, termed the *brown dwarf desert* (Halbwachs et al., 2000; Zucker and Mazeh, 2001; Sahlmann et al., 2011). As the number of known BDs orbiting solar type stars is low, the characterization of benchmark BDs in the brown dwarf desert (e.g. Crepp et al., 2016) is beneficial in understanding this sub-stellar population and to help constrain formation and evolution theories (Whitworth et al., 2007). The BD desert also provides a greater challenge as it reduces the amount of good BD candidates to study.

BDs in binary systems, unlike free-floating BDs, allow for the determination of their masses, when complemented with radial velocity (RV) and astrometry measurements. The RV technique provides the mass lower-limit (M<sub>2</sub> sin *i*) of binary and planetary companions, while complementary astrometry measurements can often provide mass upper-limits (e.g. Sahlmann et al., 2011). Measuring or tightening the constraints of BD masses improves the understanding of mass dependence on BD formation processes. For instance, there is growing evidence that the larger giant planets and BD companions do not follow the well known metallicity-giant planet correlation seen in main-sequence stars with planets (e.g. Santos et al., 2004, 2017; Maldonado and Villaver, 2017). Photometry along with stellar evolution models (e.g. Baraffe et al., 2003; Allard, 2013) can also be used to estimate the mass of BD companions (e.g. Moutou et al., 2017) if there is sufficient orbital separation, and a precise determination of the age (Soderblom, 2010).

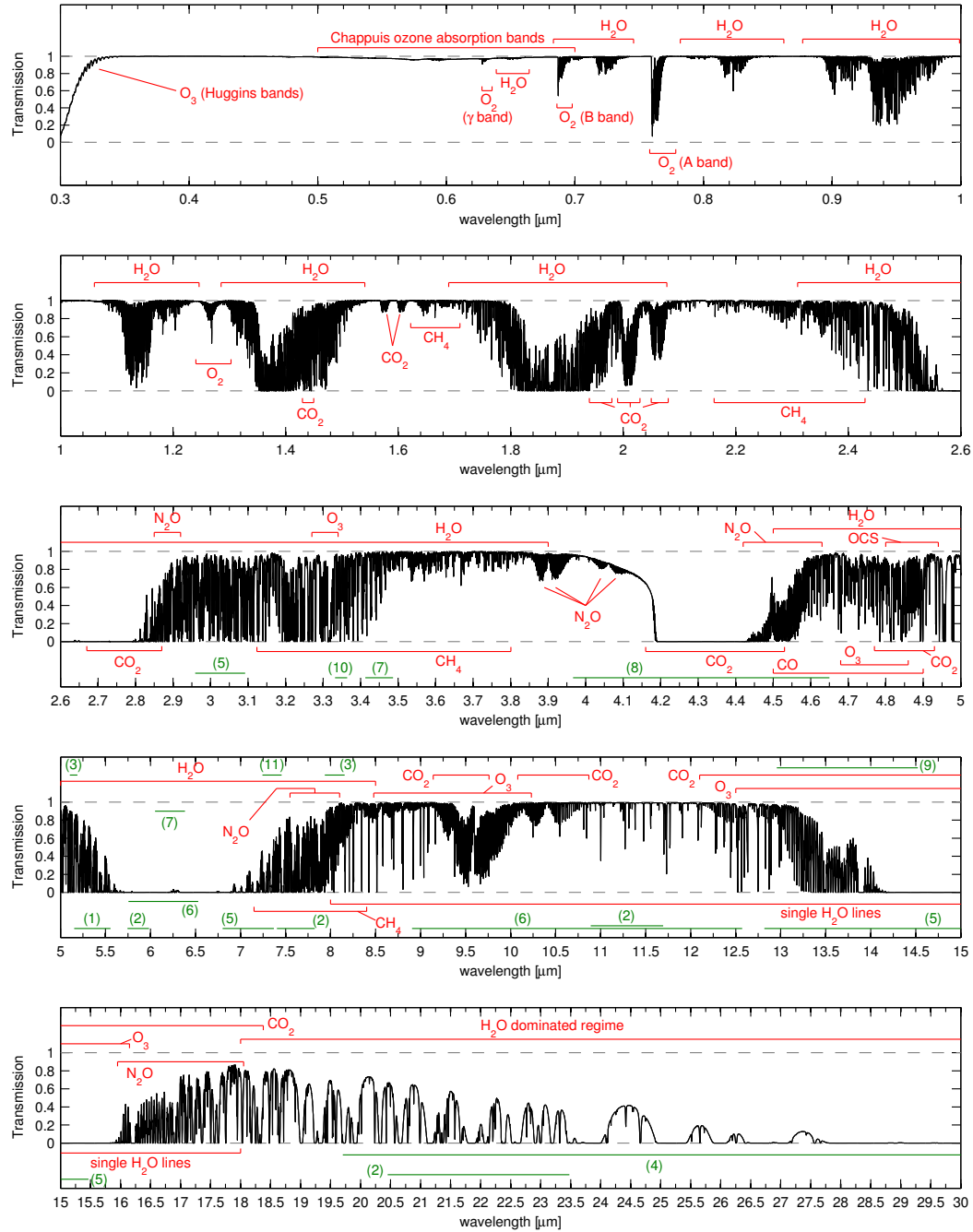


**Figure 1.2:** Reproduction of Figure 1 of Smette et al. (2015) showing telluric absorption from 0.30 μm. Original caption:

Recently, there has been a renewed interest in BD candidates triggered by exoplanetary searches. While several works found similar properties on the two populations, like a similar density (Hatzes and Rauer, 2015), others found intriguing differences. One of the most recent is the different host metallicity of the Brown Dwarf and giant planet populations (Santos et al., 2017; Schlaufman, 2018), a very strong hint of different formation mechanisms.

Spectral observations of binary systems contain the spectra of both bodies, in proportion to their flux ratio, and Doppler shifted relative to each other due to their orbital motion. One technique to recover the spectra of the companion is secondary reconstruction through a differential spectrum (Ferluga et al., 1997). Spectra from different phases are shifted to the host **stars** rest frame and subtracted to mutually cancel out the spectrum of the host star allowing the faint companion spectra to become visible. Advances in high-resolution and near-infrared (nIR) capabilities should enable this technique to be applied to BDs and planet companions, in which smaller RV shifts can be resolved and the contrast ratio of the smaller companion is improved.

Observing in the **nIRis** specifically desirable for the cooler sub-stellar and giant planet companions as their thermal emission is stronger in the infrared compared to the optical. This improves the contrast ratio between the host star and companion, providing favourable conditions for their detection and spectral separation. CRIRES, a high resolution **nIRspectrograph**, has made many prominent advances in recent years with the detection of atmospheric constituents, such as CO and H<sub>2</sub>O, atmospheric winds and thermal profiles, rotation and orbital motion, for both transiting and non-transiting planets (e.g. Snellen et al., 2010; Brogi et al., 2012; Rodler et al., 2012; de Kok et al., 2013; Brogi et al., 2014; Snellen et al., 2014; Piskorz et al., 2016; Brogi et al., 2016; Birkby et al., 2017).

The higher temperature and relatively larger size of BDs compared to giant-planets makes the development of spectral recovery techniques for BD companions a logical step towards the spectroscopic detection of planetary atmospheres. There has been the recent installation and continued development of many new high-resolution **nIRspectrographs**, such as, CARMENES (Quirrenbach et al., 2014), NIRPS (Bouchy et al., 2017) or SPIRou (Artigau et al., 2014), as well as, the CRIRES+ (Dorn et al., 2016) upgrade. These new instruments motivate the study of nIR-oriented methodologies for spectral recovery, and are of high importance due to the larger planet-to-star flux ratio provided by near-IR compared to the visible.

The search and detection of faint secondary spectra is not only relevant to planetary atmospheres. Kolbl et al. (2015) developed a method to detect the presence of optical secondary spectra down to a flux ratio of 1% in the hosts of *Kepler* transit candidates. The presence of which can cause ambiguities in the system configuration, and increase the uncertainty of the measured planet radius. The characterization of the false positive probability rate for Kepler has been found to be as high as  $\sim 35\%$  Santerne et al. (2012).

In this paper we apply two different techniques on FGK stars with BD companions with the aim to spectroscopically detect their companions. In Sect. refsec:data we present the observations and reduction process as well as the spectral models used in this work. In Sect. refsec:specdiff we explain the differential spectral technique and its applicability to these observations while in Sect. refsec:results we apply companion recovery using a  $\chi^2$  approach. In Sect. refsec:discussion we discuss our results and in Sect. refsec:conclusions we present our conclusions.

# Chapter 2

## Advanced Concepts

To put things too detailed for the introduction?

Radial Velocity: Picture of orbital motion. Concepts of RV motion- Masses, Orbits, (period, mass, distance impact.) Equation What the Equations mean.

### 2.0.1 RV calculation

We use the Keplerian orbit RV equation to estimate the RV of the host and companions at the time of each observation,  $t$ :

$$RV = K[\cos(\nu(t) + \omega) + e \cos(\omega)] \quad (2.1)$$

Here,  $K$  is the *semi-major amplitude*,  $\nu$  is the *true anomaly*,  $e$  is the orbital *eccentricity*, and *omega* is the *argument of periastron*. The true anomaly is not only a function time,  $t$ , but also the orbital period  $P$ , the *time of periastron passage*,  $T_0$ , and eccentricity. The literature parameters for each target are provided in Table 4.2. To determine the RV of the companion we transformed the RV semi-amplitude of the host  $K_1$  into the semi-amplitude for the companion  $K_2$  using the mass ratio,

$$q = M_2/M_1 = K_1/K_2 \quad (2.2)$$

We note that for the targets in which only the minimum mass ( $M_2 \sin i$ ) is known, this equation will indicate the maximum  $K_2$  value for the companion. The estimated  $K_2$  for each companion is provided in Table ?? while the RV for both components at the time of each observation is provided in Table 4.3.

The error on estimated RV values, shown in Figure 5.3, is calculated by applying the general error propagation formula (Ku, 1966) and using the errors on the orbital parameters. For a function,  $f$ , with errors on the inputs  $\delta x$ ,  $\delta y$  etc., it follows:

$$f = f(x, y, z, \dots) \quad (2.3)$$

$$\delta f = \sqrt{\left(\frac{\partial f}{\partial x} \delta x\right)^2 + \left(\frac{\partial f}{\partial y} \delta y\right)^2 + \left(\frac{\partial f}{\partial z} \delta z\right)^2 + \dots} \quad (2.4)$$

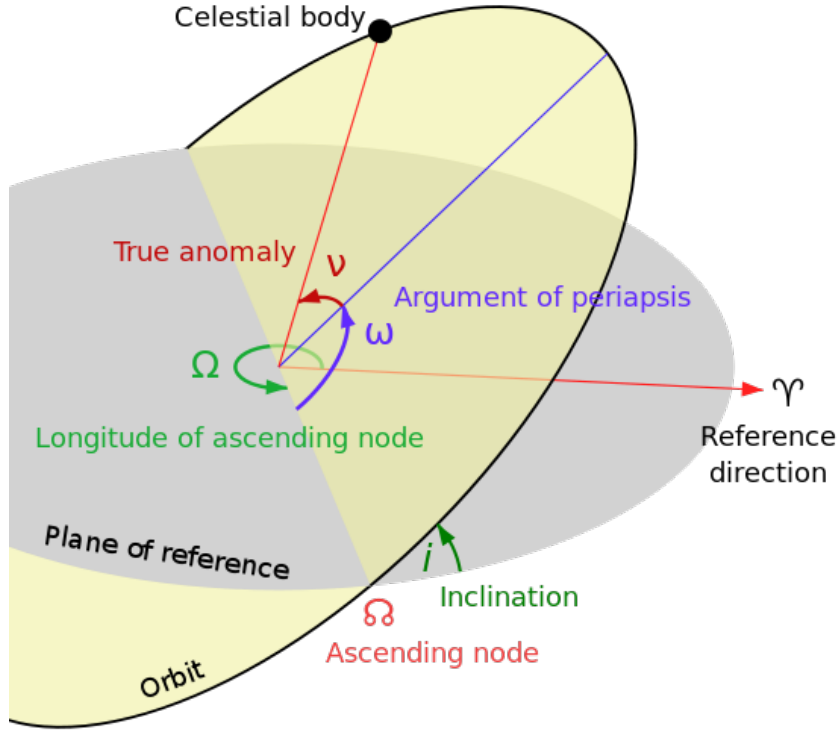


**Figure 2.1:** By Lasunnty at the English Wikipedia, CC BY-SA 3.0, <https://commons.wikimedia.org/w/index.php?curid=8971052>

## 2.1 Estimating Companion-host Flux ratio

In order to visually or spectroscopically detect binary or planetary companions it is helpful to calculate the flux/contrast ratio between the host and companion.

The companion-host flux or contrast ratio of the system can be estimated using:

$$\frac{F_2}{F_1} \approx 2.512^{m_1 - m_2}, \quad (2.5)$$

where  $m_1$  and  $m_2$  are the magnitude of the host and companion respectively.

The photometric apparent magnitudes for the host stars,  $m_1$ , in several wavelength bands are easily obtained online catalogues such as SIMBAD (Wenger et al., 2000) or 2MASS (Skrutskie et al., 2006). However, the magnitudes of the companions,  $m_2$ , are not readily available as they have not been directly measured. To estimate the magnitude of the companions stellar evolution models of Baraffe et al. (2003, 2015) are used. These models tabulate several properties of low-mass stars and BDs during their evolution. These include the temperature, radius, luminosity, and absolute magnitudes in several photometric bands, for a range of companion masses and stellar ages. A given companion mass, and a stellar age will uniquely identify a point in the Baraffe models which corresponds to a specific magnitude for the companion. The tables provided in Baraffe et al. (2003, 2015) are also interpolated to reach companion masses and stellar ages between the models provided.

In Table 2.1 the host-companion flux ratio estimates for the targets analysed in this work are presented. The K-band flux ratios are calculated as the observed spectra are in the K-band at 2.1  $\mu\text{m}$ . The ages for

**Table 2.1:** Estimated flux ratios given the companion mass ( $M_2$  or  $M_2 \sin i$ ) from Table 4.2.

Companion	Host $m_K$	Host $\pi$ mas	Companion $M_K$	Estimated $F_2/F_1$ $K$ -band	Estimated $N_2/N_1$ (noise ratio)
HD 4747	5.305	53.184	3.82	$7 \times 10^{-5}$	76
HD 162020	6.539	32.410	4.10	$2 \times 10^{-8}$	1 615
HD 167665	5.038	32.014	2.60	$6 \times 10^{-5}$	105
HD 168443b	5.211	25.208	2.35	$1 \times 10^{-16}$	$1 \times 10^8$
HD 168443c	5.211	25.208	2.35	$1 \times 10^{-11}$	$4 \times 10^5$
HD 202206B	6.485 <sup>a</sup>	21.726	3.04	$21.63$	$4 \times 10^{-8}$
HD 202206c	6.485 <sup>a</sup>	21.726	3.04	$45.63$	$9 \times 10^{-18}$
HD 211847B	7.018	20.489	3.50	8.40	0.011
HD 30501	5.525	49.081	3.96	10.38	0.003

<sup>a</sup> Magnitude from 2MASS catalogue instead of SIMBAD.

the stellar system used are given in Table 4.1 while the companion masses are given from Table 4.2. These both are used to obtain the absolute magnitude for the companions. For the companions in which only the minimum mass ( $M_2 \sin i$ ) is known then the flux-ratio given will be the lower limit, or worst case scenario.

The magnitudes provided by SIMBAD are given in apparent magnitude,  $m$ , while the magnitudes in the evolutionary models are absolute magnitudes  $M$ . That is, the apparent magnitude that the star would have if it was observed at a distance of 10 parsecs (32.6 light-years). The apparent magnitudes of the hosts are converted to absolute magnitudes using  $M = m - \mu$  where  $\mu$  is the distance modulus:

$$\mu = 5 \log_{10}(d_{pc}) - 5. \quad (2.6)$$

Here  $d_{pc}$  is the distance to the object in parsec. The distance is obtained from the trigonometric parallax  $\pi$  using the formula  $d(pc) = 1/\pi(arcsec)$ , with the parallax in arcseconds<sup>1</sup>. In this work the recent high-precision parallax measurements from GAIA are used Collaboration et al. (2018).

From the flux ratio the noise ratio between the host and companion can also calculated in a similar way using the equation  $N_2/N_1 = \sqrt{2} \times \sqrt{F_1/F_2}$ .

this section is completed i think

### 2.1.0.1 Baraffe tables

A simple tool<sup>2</sup> was created to calculate/estimate the host-companion flux ratio using the Baraffe et al. (2003, 2015) evolution tables. Given the name of the target star, the mass of a companion and the stellar/system age it determines the flux ratios the available spectral bands. The tool uses the targets name to query `astroquery` package the SIMBAD database to obtain the stellar properties, specifically the flux magnitudes and parallax. It then interpolates the Baraffe tables to the desired companion mass and age, calculating and returning values for all parameters of the companion given in the tables (e.g.  $T_{\text{eff}}$ ,  $\log g$ ,  $R/R_{\odot}$ ). The stellar magnitudes are converted to absolute values using Equation 2.6 and the flux ratios computed using Equation 2.5.

<sup>1</sup> Most parallax values e.g. GAIA are tabulated in milliarcseconds (mas). Therefore it is important to remember to convert the parallax to arcseconds first, to avoid embarrassing calculation errors!

<sup>2</sup> Available at [https://github.com/jason-neal/baraffe\\_tables](https://github.com/jason-neal/baraffe_tables)

An extension of this tool is that can be used to perform the reverse calculation also. That is, given the target name, age and flux ratio in a given band it can estimate the mass of the companion mass using the Baraffe tables.

this section is completed i think

### 2.1.1 Companion K

Maybe something can go above from this ... *These sections might be unnecessary*

To calculate the RV of the companion at the time of each observation. For a two-body system the RV semi-amplitude of the companion  $K_2$  can be determined from the orbital host-companion mass ratio

$$q = M_1/M_2 = K_2/K_1$$

. Note, that for the targets in which only the minimum mass ( $M_2 \sin i$ ) is known, this will give the maximum RV semi-amplitude of the companion. This relation was used to estimate  $K_2$  for the companion from the minimum mass or mass we have for each companion. These values along with the other orbital parameters of the system were used to calculate the RV of the companions for each observation. These values are provided with the observations in Table 4.3.

## 2.2 Synthetic models

:

In the work we make extensive use of the PHOENIX-ACES models with some experimentation with the BT-Settl models. A collection of several theoretical stellar spectral libraries can be found at Spanish Virtual Observatory Theoretical Spectra Web Server.

### 2.2.1 PHOENIX-ACES

Available

**FINISH**

### 2.2.2 BT-Settl

Available

**FINISH**

Harder to work with.

Other models which have not been used here. Kruz models a directory of different model can be found ...?

### 2.2.3 Telluric models

Utilizing telluric models has been shown to be better than the standard star method.

#### 2.2.3.1 TAPAS

### 2.2.4 Tapas models

For the wavelength calibration and telluric correction methods we use telluric line models. These have

ADAPT THIS section to explain the models more generally. Move the usage back to Reduction section

been shown to provide as good or better telluric correction compared to the telluric standard method and (Ulmer-Moll et al., 2018).

We utilized the TAPAS (Transmissions of the AtmosPHERE for ASTRonomical data) web-service<sup>3</sup> (Bertaux et al., 2014) to obtain atmospheric transmission models for each observation. TAPAS uses the standard line-by-line radiative transfer model code LBLRTM (Clough and Iacono, 1995) along with the 2008 HITRAN spectroscopic database (Rothman et al., 2009) and ARLETTY atmospheric profiles derived using meteorological measurements from the ETHER data center<sup>4</sup> to create telluric line models.

telluric model  
correction  
methods origi-  
nal

The ARLETTY atmospheric profiles have a 6 hour resolution, so there may be a slight difference between the actual profile at the time of observation.

We use the mid-observation time to retrieve transmission models for each observation, with the ARLETTY atmospheric profiles<sup>5</sup> and vacuum wavelengths selected. The telluric models were retrieved without any barycentric correction to keep the telluric lines at a radial velocity of zero with respect to the instrument.

TAPAS allows for the choice of atmospheric constituents included in the model spectra. We obtained one model with all available species present, convolved to a resolution of  $R = 50\,000$ , and another two models without an instrumental profile convolution applied. For these two extra models, one contained only the transmission spectra of H<sub>2</sub>O while the other contained all other constituents except H<sub>2</sub>O. This was to explore a known issue with the depth of H<sub>2</sub>O absorption lines in the TAPAS Bertaux et al. (2014). Section 3.4.1.1.

-> synthesizing telluric spectra nIR for CRIRES Seifahrt et al. (2010)

Look at

Using TAPAS is contrasted alongside Molecfit and Telfit in Ulmer-Moll et al. (2018). We conclude that ...

#### 2.2.4.1 Vacuum wavelengths

Astronomical light is refracted as it enters Earth's atmosphere, as it changes medium from the vacuum of space and to air. The index of refraction,  $n$ , is the factor at which the velocity,  $v$ , and wavelength  $\lambda$  of electromagnetic radiation changes from their values in a vacuum.

a good refer-  
ence that men-  
tions the uv  
and optical  
uses could be  
good?

$$n = \frac{\lambda_{vac}}{\lambda_{air}}, \frac{v_{vac}}{v_{air}} \quad (2.7)$$

The index of refraction of air is very close to 1, but has a complex wavelength dependence which also depends on atmospheric composition (e.g., CO<sub>2</sub>, H<sub>2</sub>O), temperature and pressure. There are several empirical formula for the index of refraction of air (e.g., Edlén, 1953; Peck and Reeder, 1972; Ciddor, 1996). As an example the refractive index given by Ciddor (1996), based on optical and infrared measurements and valid up to 1.7 μm, is:

$$n - 1 = \frac{0.05792105}{238.0185 - \lambda^{-2}} + \frac{0.00167917}{57.362 - \lambda^{-2}}. \quad (2.8)$$

This is measured at standard air, dry air at 15°C, 101.325 kPa and with 450 ppm CO<sub>2</sub>. Beyond 1.7 μm there are only theoretical models of the refractive index of air, due to lack of experimental data. For

<sup>3</sup> <http://www.pole-ether.fr/tapas/>

<sup>4</sup> <http://www.pole-ether.fr>

<sup>5</sup> Nearest of the 6 hourly profiles

example Mathar (2007) provides theoretical values between  $1.3 - 24 \mu\text{m}$  for common air pressure and temperature of ground-based observatories.

In this work we extensively use spectral wavelengths specified in a vacuum. The first is because the empirical relations are not valid beyond  $1.7 \mu\text{m}$ , while the CRIRES spectra we investigate are observed around  $2.1 \mu\text{m}$  and the CRIRES instrument manual provides all measurements in vacuum wavelengths.

The TAPAS synthetic transmission models Bertaux et al. (2014) we use for telluric correction are available for download in vacuum wavelengths or air wavelengths<sup>6</sup>. The PHOENIX-ACES library of synthetic spectra we use also provides spectra in vacuum wavelengths. Since both are available in vacuum wavelengths and the TAPAS models are used for calibration, vacuum wavelength exclusively, With this there is no errors introduced from conversions between air and vacuum wavelengths.

### 2.2.5 Differential techniques

See ? for lots of useful references regarding differential works Simon and Sturm 1994

Rodler 2012 uses differential of a series of phases to construct a stellar mask for the host to subtract from all measurements.

---

<sup>6</sup> The wavenumber,  $1/\lambda$ , is also available.

# Chapter 3

## NIR spectroscopic reduction

The work of this thesis relies on the use of nIR spectra obtained by the CRIRES instrument. This chapter contains an overview of the steps undertaken to extract astronomical spectra, focusing on the CRIRES instrument specifically. A comparison between two different reduction pipelines for CRIRES is performed. Details of the issues encountered with the reduction output are presented. The post reduction steps performed, specifically wavelength calibration and telluric correction<sup>1</sup> are also included in this chapter. The reduced spectra produced in this chapter will be analysed in Chapter 4 and Chapter 5. We wrap up this chapter by highlighting other techniques in high resolution nIR spectra reduction and calibration which may have improved some of the results.

### 3.1 Summary of dataset

The work performed relies on high resolution nIR spectra, obtained around  $2.1\text{ }\mu\text{m}$  with CRIRES. In brief, we have 17 individual observations of 7 target stars obtained in 2012. Each observation contains 8 individual observations performed in an ABBAABBA nod cycle pattern. Here we detail the steps performed to extract the stellar information from the raw observations. Further details of the observations and the motivation for them are given in Chapter 4.

### 3.2 NIR spectroscopy

To perform spectroscopy requires an instrument called a spectrograph. The purpose of which is to take the incoming star light and separate it into its different wavelength<sup>1</sup>(think colours in the visible). All spectrographs<sup>2</sup> are comprised of a few key components. The first part is the front end optics responsible for collecting the light and getting it to the spectrograph, such as a telescope. The second part<sup>3</sup> dispersive elements inside the spectrograph, such as a prism or grating used to separate the wavelength components. The final part is the detector or camera, used to recording<sup>4</sup> the resulting spectrum.

The design of spectrographs is highly dependant on the wavelength range observed. For instance CCD cameras (based on Silicon) are readily used in the optical but silicon is a poor detector at nIR wavelengths. Instead nIR spectrographs need to use CMOS detectors which are composed of different materials to be<sup>5</sup> are sensitive to different wavelengths. CRIRES detectors specifically are made of InSb

(Indium antimonide) to perform spectroscopy between 1–5  $\mu\text{m}$  Dorn et al. (2004). Other considerations are needed such as the composition of the optical components as well as any anti-reflection coatings used, all of which have different wavelength characteristics that need to be matched.

I don't know where I am going with this section.

### 3.2.1 General reduction Concepts

Focus on our observations

There are 3 main effects that need to be accounted for in nIR spectroscopy which influence the observations and calibrations taken. We briefly detail them here and how they are corrected [for](#)

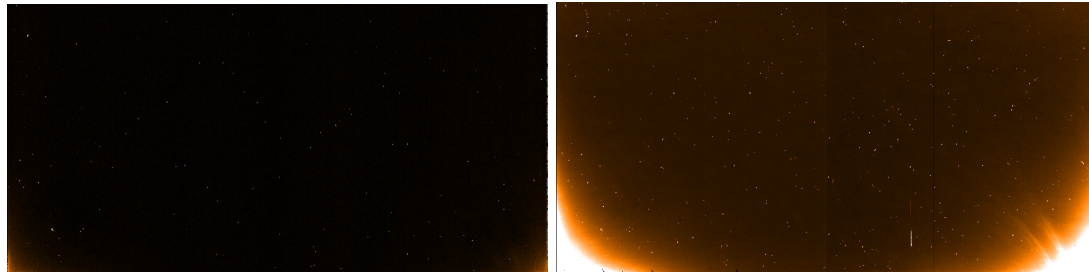


**Figure 3.1:** Master dark frames for exposure times of 3 and 180 seconds. Each master is created by averaging 3 images in which the detector received no incident light. Both frames are on the same scale and show dark current grows with exposure time. The colour has been inverted so that black is the recorded measurement.

#### 3.2.1.1 Dark Current

The dark current is a form of instrumental noise, in which the detector measures photons while not being illuminated. It is the detection of thermal electrons moving inside the detector, creating spurious photon counts. Calibration and removal of the dark current is performed by taking exposures in which the detector is not illuminated. The detectors in the CRIRES instrument are cryogenically cooled to a temperature of  $\sim 27\text{ K}$  (within  $0.1\text{ K}$ ) to significantly reduce the dark current, and to maintain consistency. The electrical components of the CRIRES detectors create thermal energy while operational which impacts the dark current. A strong glow is observed in the bottom corners of the CRIRES detector in Figure 3.1 due [nearby amplifiers](#). As per the CRIRES calibration plan, “dark frames” need to be taken for each exposure time used. Figure 3.1 shows the master dark frame created from averaging three dark frames for exposure times of 3 seconds (for the flats) and 180 seconds (for the science), both on the same amplitude scale. For the CRIRES detectors the dark current per pixel is around  $0.2\text{--}0.4\text{ }(\text{e}^-\text{s}^{-1})$ , while the glow at the two corners of the 180 second exposure shown here is around  $\sim 9000/180 \approx 50\text{ }(\text{e}^-\text{s}^{-1})$ .

#### 3.2.1.2 Flat-field

No detector is truly perfect, with all pixels performing equally well. To correct for pixel-to-pixel variations in photon sensitivity across the detector and for any distortions in the optical path, a flat-field correction is needed. Exposures of a uniform<sup>1</sup> light source are taken, allowing the individual pixel-to-pixel sensitivity

<sup>1</sup> Ideally uniform intensity and spectral distribution

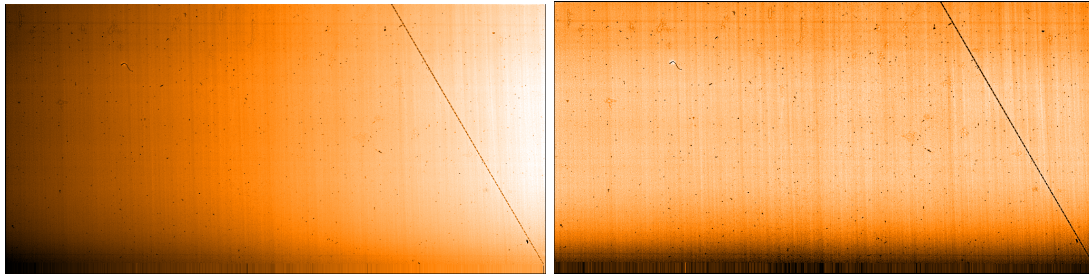


**Figure 3.2:** A flat-field image for detector #2 before (left) and after (right) the non-linearity corrections are performed.

to be measured and corrected. The flat-field frames are corrected for dark current by subtraction of the master dark frame with the appropriate exposure time.

The CRIRES detector suffers from nonlinearities in sensitivity across the detector. This can be seen in the flat-field image on the left of Figure 3.2 where there is a gradient from white to black across the detector. A set of coefficients for each pixel is provided by ESO<sup>2</sup> to apply the correction for the nonlinearity of the detectors. This also corrects for a slight difference in sensitivity between the pixels from the odd and even columns in the CRIRES detectors, commonly called the “odd-even effect”. The frame on the right of Figure 3.2 has been corrected for the nonlinearities.

The flat-field can also reveal defects in the detector e.g. dead pixels, dust or scratches; a large scratch is show clearly visible in Figure 3.2.

### 3.2.1.3 Nodding and Jitter

The technique of *nodding* is used to remove sky emission, detector dark current, and glow. First, an observation is split into multiple separate exposures. Between each exposure the telescope is moved to change the vertical position of the target in the slit. The light from the star travels through a slightly different optical path and is recorded on a different part of the detector. The frames from the two nod positions (A, B) are then subtracted (A-B) to remove the background measurement from each spectra.

A visual example of the nodding is shown in Figure 3.3. On the left are slices of 150 pixel columns from successive nod positions A and B as well as the difference A-B. On the right is a single pixel column from each image on the left. The background signal at the level of 20-30 counts in the image is almost canceled out by the opposite nod. This efficiently removes the background signal/noise from the observed spectra target.

Observations of faint targets, that need long exposure times, are also broken up into multiple images so that the instrument glow from Figure 3.1 does not saturate the detector.

[FIXup this table](#)

[fix Figure 3.3](#)

A small random vertical offset is applied to each observation which ensures that all spectra at the same nod position do not consistently land on the same pixels each time. This is known as the *jitter* and allows for the correction of bad pixels and decreases the effect from any systematics of the detector.

As an example, the CRIRES observations analysed for the work performed in Chapter 4 and 5 were performed with an ABBAABBA nod cycle pattern with an exposure time of 180s each, or 24 minutes all

[move](#)

<sup>2</sup> Available at <https://www.eso.org/sci/facilities/paranal/instruments/cires/tools.html>

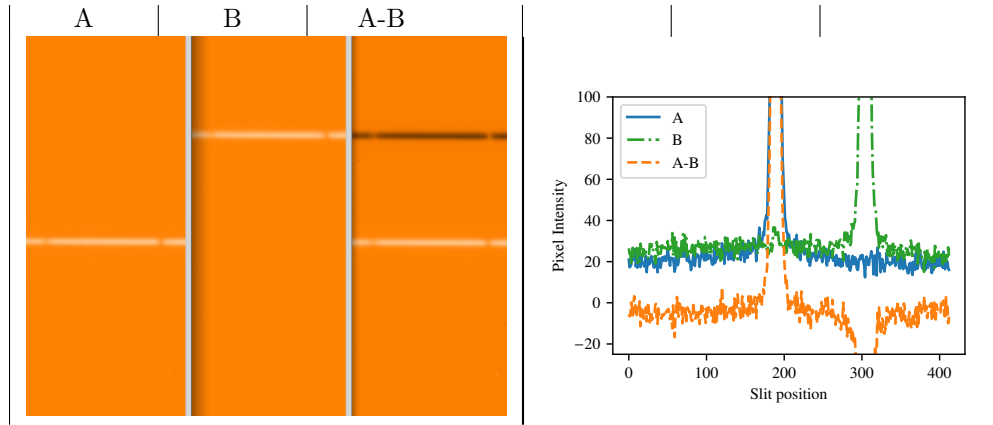


**Figure 3.3:** Illustration of the nodding technique. Left: Sample slice of successive images at nod positions A and B, and their difference A-B for detector #1. Right: A vertical slice along the slit at column 512 (middle of detector). The background level observed in A and B is effectively removed by the subtraction.

up.

### 3.2.2 Th-Ar lamp calibration

As part of the CRIRES calibration procedure, spectra are taken of Th-Ar lamps. The Th-Ar spectra are placed into the instrument using 6 optical fibres, creating 6 uniformly spaced spectra across the detector. Figure 3.4 contains the Th-Ar spectra for all four detectors. There are  $\sim 50$  Th-Ar lines that fall across the four detectors for the wavelength setting here, although most of them are faint.

The purpose of the Th-Ar fibres is to perform cross-correlation against a Th-Ar template to obtaining a wavelength solution for each detector. Optical defects (e.g. scratches on the detector) interfere with the performance of the correlation between Th-Ar lines and the spectral template in ESO pipeline. This can be resolved by first applying a pixel mask (although we did not attempt it). At the top and bottom there are also two meteorological fibres that can not be used for wavelength calibration as they pass through a different optical pathway. The brightest one at the bottom has strong features that seem to overwhelm or washout many columns in detector 2–4 (vertical stripes). This information is included here for completeness, as the Th-Ar were not used in the chosen data reduction method, see Section 3.4.1.

Check if it is mentioned how these get corrected/ if the impact the wavelength solution.

Note: Useful information about MIR reduction in the VISIR manual

### 3.2.3 Extraction

The process of extraction is, in brief, turning the two-dimensional image of the spectrum into a one-dimensional representation. This is done by summing the photon counts along the spatial direction, for each column in the dispersion direction in a small window around the spectrum. To do this one needs to identify the position of the spectrum across the detector, referred to as order tracing. In our case there is only one spectral order present but in a cross-dispersed configuration there can and will be many orders. A rectangular box, with a specified aperture width, is centred along the traced spectrum.

There are two types of extraction commonly used. The *rectangular* extraction performs a simple aperture sum in the spatial direction, counting all photon counts that fall within the aperture. An

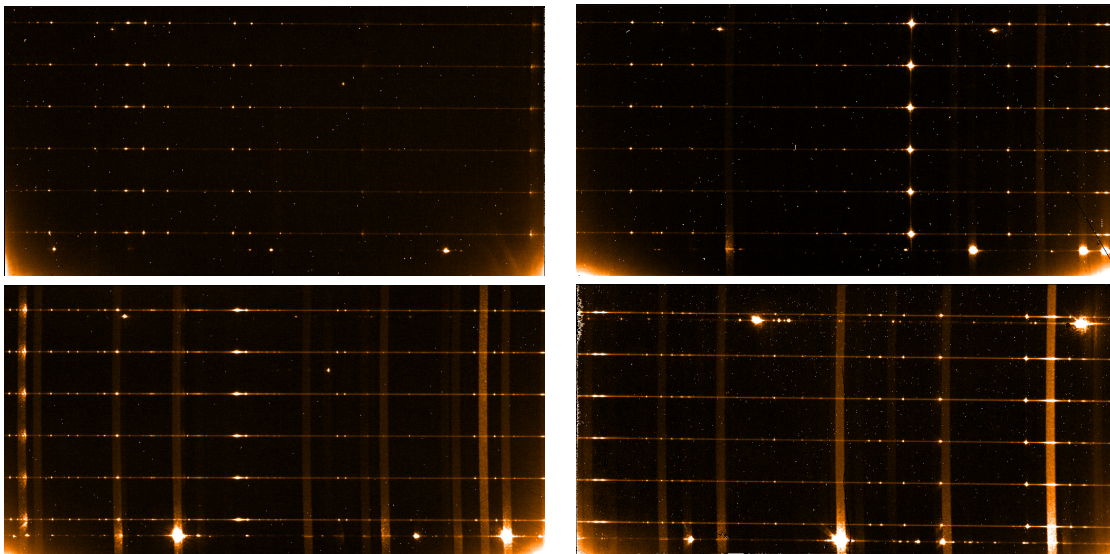


**Figure 3.4:** Example Th-Ar calibration lamp frames for each detector. These are the raw frames in which dark current correction has not been performed (i.e the dark current is still visible on the bottom corners).

*optimal* extraction (Horne, 1986) also includes variance weighting to reduce the impact of the noise and deviant pixels on the spectral extraction. A spatial profile is fitted to the spectra and the pixels weighted such that those furthest away from the centre have less impact on the sum. Optimal extraction can increase the effective exposure time by up to 1.69 times at  $3\sigma$  (Horne, 1986). Both rectangular and optimal extraction methods are available from both the ESO CRIRES and DRACS pipeline, compared below.

### 3.3 Pipeline Comparison

To be able to extract the target spectra from the calibration and observation images, a number of steps (some outlined above in Section 3.2.1) have to be performed in sequence. The series of steps, performed by various software tools, is referred to as a *pipeline*. Each stage in the pipeline performs a specific task, for example creating the master dark frame, or performing the nod subtraction. The result of one stage is passed to the next (either automatically or manually). Two different pipelines were available to reduce the CRIRES observations used in this work. The first is the standard CRIRES pipeline<sup>3</sup>, available from ESO. The second is an in-house pipeline previously used in Figueira et al. (2010) called DRACS (Data Reduction Algorithm for CRIRES Spectra)

In these next sections we document our experience using both pipelines, comparing the extracted spectra and user experience.

Reword

Pedro it is my understanding that the ESO pipeline did not exist/was not publicly available when you created DRACS, correct?

<sup>3</sup> <https://www.eso.org/sci/software/pipelines/>

### 3.3.1 ESO CRIRES pipeline

The ESO CRIRES pipeline was used to reduce CRIRES nodding spectra following direction from the CRIRES pipeline user manual<sup>4</sup> and the CRIRES reduction cookbook<sup>5</sup>

The GASGANO<sup>6</sup> graphical user interface (GUI) was used to interact with the pipeline with guidance from the GASGANO manual<sup>7</sup>. This pipeline provides a number of *recipes* which perform the required extraction steps. From the GUI each recipe is manually selected, then the correct calibration and observation files need to be selected to use with each recipe. The final output from the ESO pipeline is a table in a `fits` format with the combined extracted spectra (both *rectangular* and *optimal* extractions), pixel errors and a wavelength solution.

For a novice of spectral extraction this pipeline and the available documentation was very helpful to get started and perform the extraction. However, to reduce many spectra it soon became a long tedious process.

Constant revision of the documentation was necessary to ensure all the correct image and calibration files were added to each recipe. The ESO pipeline makes all the recipe parameters easily accessible to modify via a window of the recipe interface. This is great for adjusting the parameters and for identifying which parameters are relevant to each recipe. When trying to experiment with the recipe parameters to achieve high quality spectra extraction it was repetitive to change the same parameters for each observation. It was also difficult to keep track of all the changes while assessing their effect on the final output. The recipe parameter defaults get restored for each observation, making it difficult to reduce all of the observations in a consistent manner.

The parameters for the wavelength calibration were the most tedious. To try and improve the wavelength calibration, the y-positions of the 6 Th-Ar fibres were manually found from the images for each detector and every observation and entered as input parameters for the calibration recipe. This helped the wavelength calibration recipe to correctly identify/fit more of the Th-Ar spectra in most cases, but this took time. Because of this, it was chosen to use the other pipeline and these calibration were not used.

ESO has a new reduction “workflow” called ESO Reflex(Freudling et al., 2013)<sup>8</sup>. This enables automated reduction with the ability to chain together the extraction recipes in the specific order desired, repeat steps to optimize the reduction, and automatically handle the data organization (no need to manually select the files for each recipe). This would likely have enabled a quicker and more consistent reduction of the spectra. Unfortunately, it is not available for the CRIRES pipeline.

### 3.3.2 DRACS

DRACS (Data Reduction Algorithm for CRIRES Spectra) is a custom reduction pipeline (Figueira et al., 2010) written in IRAF’s CL<sup>9</sup> (Tody, 1993). It provides for automated dark and nonlinearity corrections (using the nonlinearity coefficients provided by ESO), as well as the flagging and replacement of bad pixels. Sensitivity variations are corrected by dividing by a flat-field which was corrected from the blaze function

<sup>4</sup> <ftp://ftp.eso.org/pub/dfs/pipelines/cires/crire-pipeline-manual-1.13.pdf>

<sup>5</sup> [https://www.eso.org/sci/facilities/paranal/instruments/cires/doc/VLT-MAN-ESO-14200-4032\\_v91.pdf](https://www.eso.org/sci/facilities/paranal/instruments/cires/doc/VLT-MAN-ESO-14200-4032_v91.pdf)

<sup>6</sup> <https://www.eso.org/sci/software/gasgano.html>

<sup>7</sup> <https://www.eso.org/sci/software/gasgano/VLT-PRO-ESO-19000-1932-V4.pdf>

<sup>8</sup> <https://www.eso.org/sci/software/esoreflex/>

<sup>9</sup> IRAF is distributed by the National Optical Astronomy Observatories, which are operated by the Association of Universities for Research in Astronomy, Inc., under cooperative agreement with the National Science Foundation.

effect. The nodding pairs are mutually subtracted and the order tracing is accomplished by fitting cubic splines. Order tracing allows the extraction algorithm to follow the shape for the dispersion across the detector<sup>10</sup>. By default the pipeline returns the *optimal extraction* (Horne, 1986), but the *rectangular* extraction can also be obtained. The extracted spectra from each nod is continuum normalized by dividing by a polynomial fitted to the continuum, with the polynomial degree selected individually for each spectrum and detector. Finally, the normalized nod-cycle spectra are averaged together to give a single reduced spectrum, normalized to 1.

is footnote correct "instruments optics"

The DRACS pipeline was originally developed to work with *H*-band spectra. Because of this, some of the parameters were adjusted in an attempt to achieve a better reduction on the *K*-band spectra analysed here. The parameters adjusted were the tracing and normalization polynomial functions and their specific order on the detector. Also, there was initially no reduction parameters present for detector #3 (as this had not been used with ~~in~~ previous works using this pipeline). Therefore, the pipeline was extended to be able to reduce detector #3 of CRIRES, ~~but~~ adjusting the pipeline code and finding suitable parameters for detector #3.

When using the DRACS pipeline on a new target, the tedious part is initially creating the lists of files identifying which files are the dark, flat, and the science frames<sup>11</sup>. After these lists are created, the reduction pipeline can be run and re-run easily, making the effort worth it.

The first time through is interactive with a number of manual checks decisions to be made (e.g. confirming the order tracing position, and fit is good). DRACS remembers them in a database, allowing for ~~less interaction needed~~ a second or third time through the pipeline. This was useful to experiment with and iterate the reduction parameters of the pipeline. When changing the parameters which ~~affect~~ the order tracing, the database with the order tracing results needed to be deleted so that it would not influence the new fits. These parameters were therefore slower to iterate on.

This semi-autonomous nature of the DRACS pipeline means that all the spectra can be reduced in a consistent way, relatively quickly, and does not require manual spectra selection for each individual recipe as was done with the ESO pipeline.

There are a couple of drawbacks with using the DRACS pipeline. The first is the lack of documentation on how to use it. This required looking through the source code to find which functions and scripts do which part of the extraction. DRACS makes use of many IRAF packages which have documentation available online<sup>12</sup>. Searching through this documentation was difficult, but required, to understand how to use and modify DRACS.

The second drawback is that DRACS does not perform wavelength calibration, which is included with the ESO pipeline. This means an external wavelength calibration was the only option (see Section 3.4.1). The last drawback is the discovery of artefacts present in the nod spectra, which we discuss in detail in Section 3.3.3.1.

### 3.3.3 Pipeline comparison and selection

Both reduction methods were applied to the same CRIRES spectra to check the quality and consistency of both methods. In Figure 3.5 two examples of the extraction for HD30501-1 (left) and HD202206-1 (right) from both pipelines are provided. The blue lines are the extracted spectra from the ESO

<sup>10</sup> The spectra do not fall perfectly horizontally on the detector and usually contain some curvature due to the optics of the instruments.

<sup>11</sup> The GASGANO GUI was helpful to help identify the distinction of each fits file for a beginner.

<sup>12</sup> Such as at the [http://stsdas.stsci.edu/gethelp/pkgindex\\_noao.html](http://stsdas.stsci.edu/gethelp/pkgindex_noao.html).

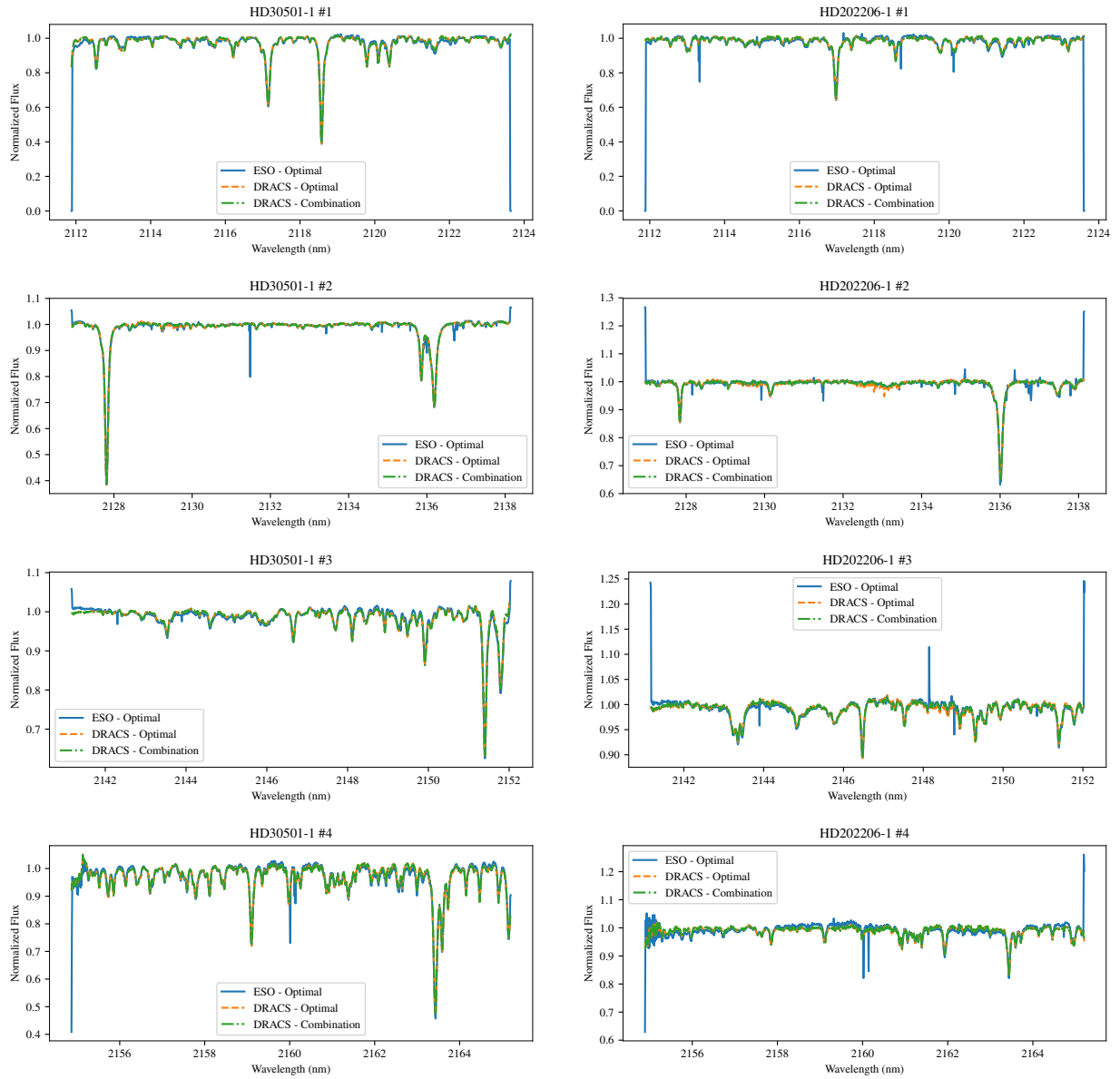


**Figure 3.5:** Comparison between the ESO pipeline and DRACS pipeline. For two observations HD30501-1 and HD202206-1. The blue lines are the extracted spectra from the ESO pipeline, the orange dashed lines are the optimal extraction from the DRACS pipeline, while the green dash-dotted line is the DRACS extraction after dealing with artefacts in the optimal extraction addressed in Section 3.3.3.1. The wavelength information applied to the spectra here comes from the ESO pipeline.

pipeline, the orange dashed lines are the optimal extraction from the DRACS pipeline, while the green dash-dotted line is the DRACS extraction after dealing with artefacts in the optimal extraction addressed in Section 3.3.3.1.

One of the important things checked was the line depths of each spectra to ensure that the pipelines were consistent. The ESO pipeline has noticeable issues, with many large spikes still present in the spectra, likely caused by bad pixels or cosmic rays that are not correctly removed. There also appears to be problem with edges of the ESO reduced spectra, with very large spikes at either end.

At this stage the DRACS pipeline was chosen, as it was considered that the DRACS pipeline produced better extracted spectra than the ESO pipeline. This decision was based on the quality of the reduced spectra, as well as the relative ease of use of the pipeline (being semi-automated once set up). Another deciding factor was the need to create software to remove the bad pixels observed in the ESO reduced spectra. However, this was unavoidable as it was eventually required for the DRACS reduced spectra<sup>13</sup>. Though the ESO pipeline provided a wavelength solution for the spectra, this did not factor into the decision as it was considered too unreliable due to known issues with CRIRES wavelength calibration, necessitating a new wavelength calibration anyway.

The spectra used here in the comparison are the combination of the 8 nod spectra. Later it was discovered, that individual nod spectra from the DRACS pipeline had issues, see Section 3.3.3.1. These are difficult to notice on this scale as they each constitute 1/8th of the information. As an example of this is seen in detector #2 of HD202206-1 in Figure 3.5. An artefact from a single nod spectra, which is shown in Figure 3.6, is barely visible in the pipeline comparison here as a slight depression of the orange dashed line between 2132 and 2134 nm. We explain the identification of these artefacts and how we deal with them (green lines) in the following section.

### 3.3.3.1 Reduction issues

At a later date some large artefacts in the DRACS extracted spectra were identified. An investigation into the cause of these artefacts was undertaken to identify their source and remove them from the spectra. Separating out the individual nod spectra side-by-side revealed that the artefacts were occurring in only a few of the individual nod spectra from the optimal extraction and that they were not present in the rectangular extracted nods. Four examples are shown in Figures blah and blah. In each panel the top sub-plot contains the optimal extracted spectra, while the middle sub-plot contains the rectangularly extracted spectra.

Check optimal extraction parameters, may have reduced the extraction width by too much?? Need to check changing it.

The occurrence of artefacts in the observations did not appear to have a pattern with nod position or detector. They do occur with large spikes in the rectangular extractions. There are many other spikes in the rectangular extractions that do not create the artefacts observed.

It is clear that the artefacts in the optimally extracted nods correspond to large pixel spikes present in the rectangular extracted nod. As mentioned in Section 3.2.3 the *optimal* extraction includes variance weighting across the spatial direction. It appears that the presence of cosmic rays or bad pixels heavily affected the variance weighting procedure during the *optimal* extraction. It is also observed that the artefacts created are not localized to the region around the bad pixel region but affect a extended spectral range (100's of pixels in some cases).

Numerous parameters in the DRACS pipeline were experimented with to try and remove the observed artefacts with limited success. For instance, no complete removal of the artefacts was found by manually

<sup>13</sup> see Section 3.3.3.1!

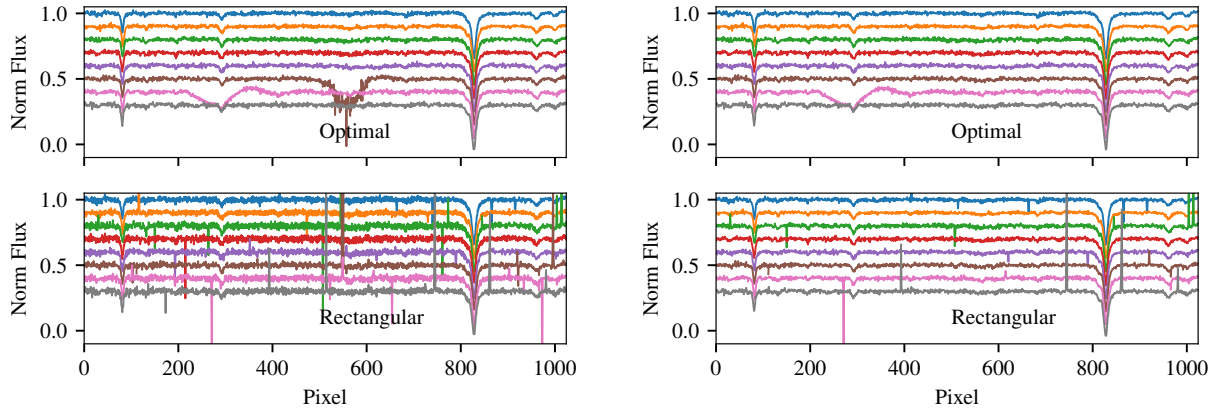


**Figure 3.6:** DRACS reduction of HD202206-1 detector 2 with a single pipeline parameter changed. Left: Pipeline with the “doslit.resize” set to “no”. Right: The same but with “doslit.resize” set to “yes”. During the order tracing the aperture size is automatically adjusted but the **finish this sentence**. Setting the resize parameter for **apextract?**. Changing this one parameter removed one large artefact but kept the other. One large artefact is removed, one is not.

changing the  $\sigma$  rejection limits (between  $1 - 5\sigma$ ) and increasing the tracing width parameter of IRAFs DOSLIT<sup>14</sup> recipe. Although it did slightly affect the shape of the artefacts. During the creation of this document we found that the enabling automated aperture resizing<sup>15</sup> by setting the “resize” parameter to yes does manage to remove one of the large artefacts in the observation of HD202206-1. We show the effect of this in Figure 3.6 with the optimal and rectangular extraction from the DRACS pipeline with only the *resize* parameter changed. The artefact in the 6th nod is removed but the artefact in the 7th nod is still present.

This discovery came too late to implement it for all of the observations, re-doing all the analysis, but does indicate that some improvements may be obtained with extensive time and patience tweaking the parameters of the DRACS pipeline.

The artefacts in the individual nod spectra were observed to create flux deviations in the fully combined optimally extracted spectra of  $\sim 0.5\%$ . The purpose of these spectra was to detect faint companion spectra with expected flux ratios  $F_2/F_1 < 1\%$ . We therefore needed to take measures to remove these artefacts from the combined spectra.

The solution that we chose was to replace the optimally extracted nods that contained artefacts with their rectangular counterparts. Creating a combined spectra that had a mix of optimally reduced and rectangularly reduced nod spectra. To replace the spikes in the rectangular extraction that created the artefacts and others a iterative  $4-\sigma$ <sup>16</sup> rejection algorithm<sup>17</sup> was applied to the rectangular extractions. The  $\sigma$  for each pixel was calculated as the standard deviation of the nearest 2 pixels on either side of it, across all 8 nod spectra. Any rejected pixels were replaced using linear interpolation along the spectra.

Combined spectra were finally constructed by averaging the eight nod-cycle spectra together, where some of the optimally extracted spectra have been replaced using the above method. The third panel of Figure 3.7 shows the difference between the combined spectra using only optimally extracted spectra and

finish this sentence in caption

<sup>14</sup> Documentation for DOSLIT can be found here <http://stsdas.stsci.edu/cgi-bin/gethelp.cgi?doslit>

<sup>15</sup> Using <http://stsdas.stsci.edu/cgi-bin/gethelp.cgi?apresize.hlp>

<sup>16</sup> There is no justification why  $4-\sigma$  was chosen over the commonly used  $3-\sigma$ .

<sup>17</sup> Found at [https://github.com/jason-neal/nod\\_combination](https://github.com/jason-neal/nod_combination)

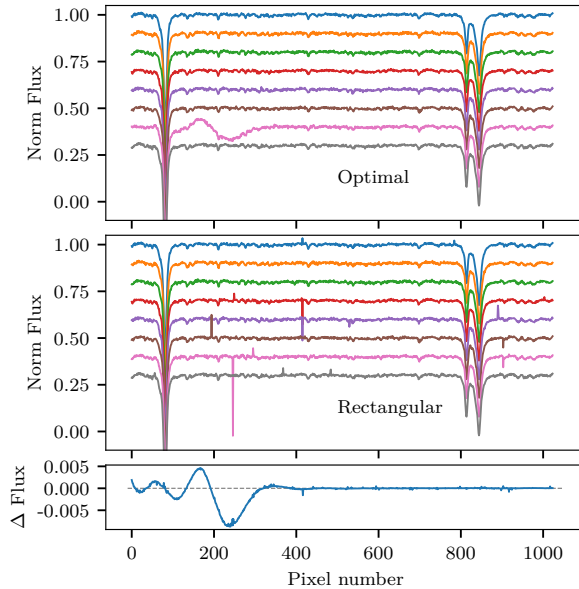


**Figure 3.7:** Example of an artefact in the optimally extracted spectra from detector #2 of HDXXXXXX. The top panel contains the 8 normalized nod spectra obtained using optimal extraction. The middle panel shows nod spectra using only rectangular extraction. The bottom panel shows the difference between a combined spectrum using optimal nods only and a combined spectrum in which the identified nods are replaced with their rectangular counterparts as per Section 3.3.3.1. A vertical offset is included between each spectra for clarity. The nod spectra are in observation order from top to bottom.

the mixed combination with replacements. The actual spectra from the two different methods can be seen in Figure 3.5 where orange is the combination of optimally reduced spectra only and green uses the replacement method outlined here.

There is a clear large extended artefact on the 7th nod of the top panel is created by the large spike. For the first panel a single large spike in the 7th nod (pink) near pixel 230 creates a wide and noticeable artefact in the optimal extraction. This is the same spectra as the 2nd down the right of Figure 3.5.

EXAMPLE with the new-old Figure 3.7.

The fraction nod spectra from all detectors and observations affected by artefacts was 14 percent. These are detailed in Table A.1. More examples of observations that contain artefacts are given in Appendix A. Selected to show their range of variation.

The continuum normalization is performed in IRAF while the mixed combination is carried out in *Python* along with the post reduction procedures detailed below. This pipeline was chosen over the ESO CRIRES pipeline because it seemed relatively simpler to use, being semi-automated, and appeared to have less bad pixel/cosmic ray artefacts in the resulting spectra. In hindsight the artefacts that appeared in the DRACS reduction took longer to investigate, a create a solution. This involved a script to remove the bad-pixels that created the artefacts, something we tried to avoid by using the DRACS pipeline instead of the ESO pipeline.

These artefacts in the *K*-band spectra were not observed in previous works in the *H*-band using this pipeline and as such may have a wavelength dependent effect. Although another possibility could be that there were artefacts in intermediate steps of the previous works that were missed due to the semi-automated pipeline, with the combined output only slightly affected.

CHANGE the figure here

check this statement

In the paper We say it could be glow. I do not think it is anymore and think it is just bad pixels not correctly removed. Either way it does not affect our results significantly.... This method is likely to have a slight negative impact on the noise/SNR

Note for HD202206 the 1st two nods have a much higher extracted flux. I am still unsure why this is...

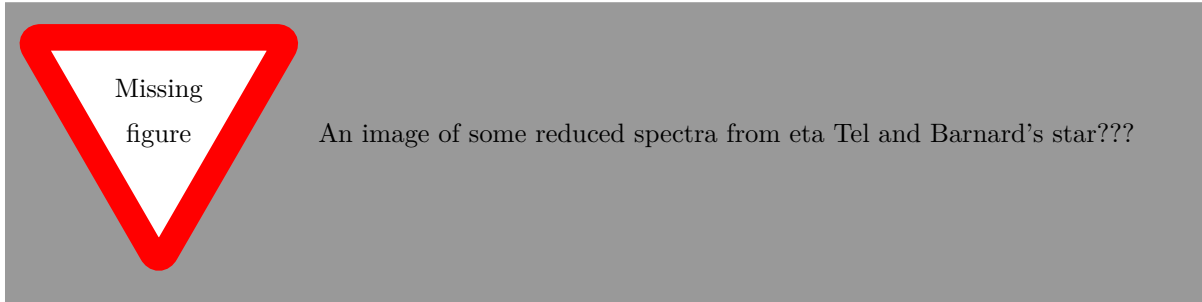
Much time and effort **when** into trying to extract the spectra as best as possible, without artefacts to have the best chance at obtaining high quality scientific results of the faint features we were trying to detect. Due to time constraints the replacement of nods with artefacts (indicated in Table A.1) with their rectangular counterparts was performed.

### 3.3.4 Reduction experience:

The experience gained in reducing CRIRES spectra enabled participation in collaboration with other science cases. The DRACS pipeline was used to extract the spectra of two other targets. A target and a very brief aim of each science case is given below.

- Barnard's Star<sup>18</sup>: The carefully reduced nIR spectra of Barnard's Star was meant to extend the work of Andreasen et al. (2016) in deriving the spectroscopic parameters of cool M-stars in the nIR. Unfortunately the work did not advanced enough to analyse M-star's and they analysed the spectrum of Arcturus (K0) and a fully reduced spectrum of 10Leo (K1) from the CRIRES-POP library Nicholls et al. (2017) in [citet Andreasen et al. \(in prep.\)](#).
- $\eta$  Tel<sup>19</sup>: The spectra of  $\eta$  Tel, quickly rotating Brown Dwarf, was reduced to accurately determine its rotation rate by measuring the line broadening. The results from this data will be published in an upcoming paper [Hagelberg et al. \(in prep.\)](#).
- The same spectra of  $\eta$  Tel were also used in Ulmer-Moll et al. (2018) to compare different telluric correction methods in the nIR.

For these works only the spectral extraction outlined above was performed. The post extraction and reduction steps from the following sections were not.



## 3.4 Post reduction stages

From the DRACS pipeline we have extracted the 1-D spectra of each target. The spectra still need to undergo some post-reduction **step**. In particular, wavelength calibration and telluric correction. A detailed look of how these steps were developed and performed are addressed in the following section.

<sup>18</sup> Programme ID: 085.D-0161(A)

<sup>19</sup> Programme ID: 083.C-0759(A)

### 3.4.1 Wavelength calibration

Wavelength calibration is the process of assigning accurate wavelength values to each pixel in the spectra. For CRIRES in the nIR this is challenging. CRIRES uses a Thorium-Argon (Th-Ar) lamp to place 6 emission spectra on the detector using fibres. The spectra of the Th-Ar emission lines are used to determine the spatial distribution of the wavelength solution across each detector using correlation with a spectral template. Th-Ar lamps are excellent at optical wavelengths where the numerous spectral lines enable precision of sub- $\text{m s}^{-1}$  radial velocity measurements HARPS spectrograph. For example the new ESPRESSO spectrograph uses  $\sim 8600$  Th-Ar lines<sup>(?)</sup>. However in the nIR, there is a relatively low density of Th-Ar lines (Kerber et al., 2009), which, in combination with the alignment of the narrow wavelength range of the detector, causes a poor wavelength calibration to be obtained (e.g. CRIRES-POP (Nicholls et al., 2017)). Above  $2.2 \mu\text{m}$  there are O-H sky lines that can be used for wavelength calibration but for our observations below  $2.2 \mu\text{m}$  they are too dim.

These wavelength calibration issues were experienced when using the ESO CRIRES pipeline, with non-Th-Ar lines features sometimes affecting the correlation.

At the wavelength of  $2.1\text{--}2.17 \mu\text{m}$  there are roughly XXX Th-Ar lines across all four detectors, as seen in Figure 3.4. The DRACS pipeline does not use the Th-Ar lamp files for wavelength calibration and leaves this as a post reduction step.

A common method for wavelength calibration that does not rely on Th-Ar lamps of CRIRES involves using the telluric lines present to provide the wavelength solution (e.g., Brogi et al., 2012, 2014; de Kok et al., 2013) (Piskorz et al., 2016). This is made possible by the use of high resolution spectra, in which the telluric lines are well resolved, as well as accurate spectral information of the atmosphere.

We follow this method using the telluric absorption lines present in each observation as the wavelength reference. Instead of directly using the HITRAN database (Rothman et al., 2013) for the telluric line positions Brogi et al. (such as in 2012, 2014); de Kok et al. (such as in 2013), we use the TAPAS atmospheric transmission models (Bertaux et al., 2014) obtained for each observation. The TAPAS models use the HITRAN database but also includes atmospheric profiles and physical meteorological measurements to model the telluric absorption strength.

To calibrate the wavelength the telluric lines in the model need to be associated to the corresponding telluric lines in the observed spectrum. The centroid<sup>20</sup> of each telluric line in the model is obtained by fitting the telluric transmission spectrum,  $T(\lambda)$ , as a simple sum of Gaussian functions (subtracted from the continuum).

$$T(\lambda) = 1 - \sum_i G(\lambda, A_i, \mu_i, \sigma_i), \quad (3.1)$$

where  $G$  is a Gaussian function of the form

$$G(\lambda, A, \mu, \sigma) = Ae^{-(\lambda-\mu)^2/2\sigma^2}, \quad (3.2)$$

and  $A$ ,  $\mu$ ,  $\sigma$  are the amplitude, central wavelength, and standard deviation for each line respectively. Telluric lines actually have a Voigt profile<sup>21</sup> although they are not fully resolved in the nIR and their

<sup>20</sup> Centre of the line

<sup>21</sup> A Voigt profile is a convolution of two broadening profiles, a Gaussian and a Lorentzian. Gaussian broadening results

fix-up get a good citation, number of lines

paper for harps Th-Ar lines

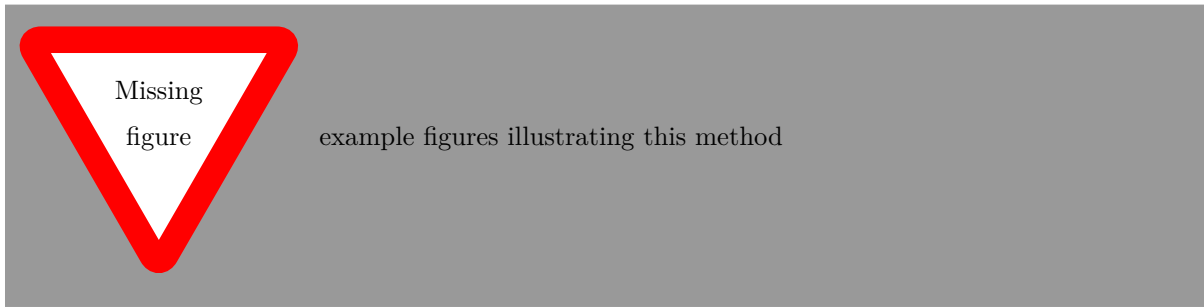
cite cires manual, and a paper about sky lines?

shape is dominated by the instrumental profile. Seifahrt et al. (2010) measured the instrumental profile of CRIRES using singular-value decomposition and show that it is extremely well represented by a single Gaussian below a SNR of around 300. Therefore, wavelength calibration using single Gaussian fits to each line is sufficient.

The observed spectra contain two different spectral components: stellar and telluric lines, which are multiplied together. The observed spectra are therefore are fitted with a multiplication of two Gaussian-sum models. The identification between telluric and stellar lines is performed by hand for each spectra, using the telluric model as the reference. Care was taken to fit the correct components to blended spectra where possible to improved the number telluric lines use for calibration. The fits were inspected to ensure that they reasonably matched the line positions. There was difficulty in identifying the shallow lines with depths below 1–2%. But these were needed in some spectra to obtain a suitable fit. If there were blended lines that did not look to fit correctly these lines were removed and not considered in the calibration step.

$$\begin{aligned} I_{obs}(x) &= I_{tell}(x) \times I_{space}(x) \\ I_{obs}(x) &= \left(1 - \sum_j G(x, A_j, \mu_j, \sigma_j)\right)_{tell} \times \left(1 - \sum_k G(x, A_k, \mu_k, \sigma_k)\right)_{space}, \end{aligned} \quad (3.3)$$

where  $x$  is the pixel coordinates of the extracted spectra.



After fitting  $I_{obs}(x)$  to the observed spectrum and  $T(\lambda)$  to the telluric model the wavelength solution was obtained by fitting a second order polynomial to the centroid values  $\{\mu_j(x), \mu_i(\lambda)\}$  from the telluric components of the observed spectra and telluric model respectively. A second order polynomial has been shown to be sufficient for higher precision RV studies (e.g., Bean et al., 2010; Figueira et al., 2010). This polynomial is then used to map the whole spectrum from pixels into wavelength. Higher 3<sup>rd</sup> and 4<sup>th</sup> order polynomials that are also used in the literature Seifahrt et al. (e.g., 2010); Ulmer-Moll et al. (e.g., 2018) were attempted but had limited success here due to the limited number and uneven spacing of telluric lines in the narrow wavelength range analysed here, especially on the second detector. There were often large deviations due to the uneven spread of telluric lines, especially at the extremities. Higher order terms for wavelength calibration are usually used in regions with a higher density of telluric lines and/or a longer wavelength span (Piskorz et al., 2016; Seifahrt et al., 2010; Ulmer-Moll et al., 2018).

---

from thermal Doppler broadening, and instrumental broadening while the Lorentzian broadening comes from molecular vibrational bands(Meier, 2005).

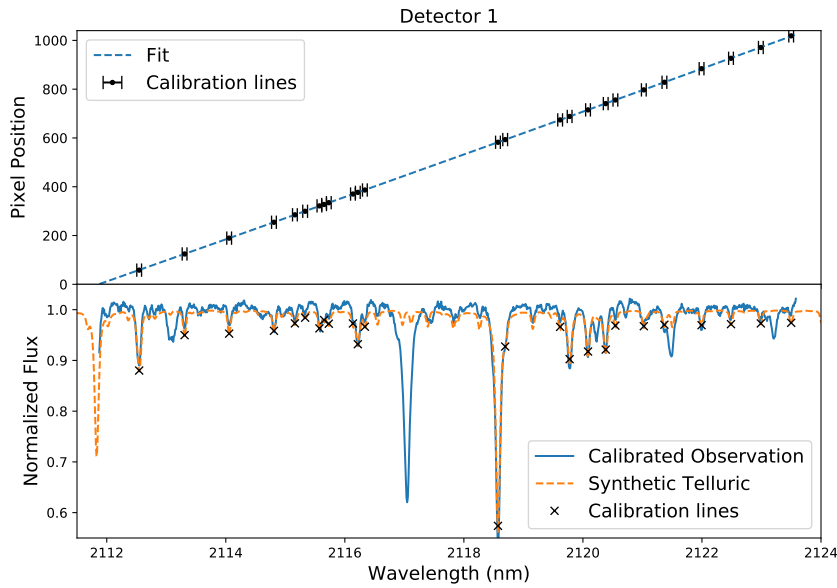
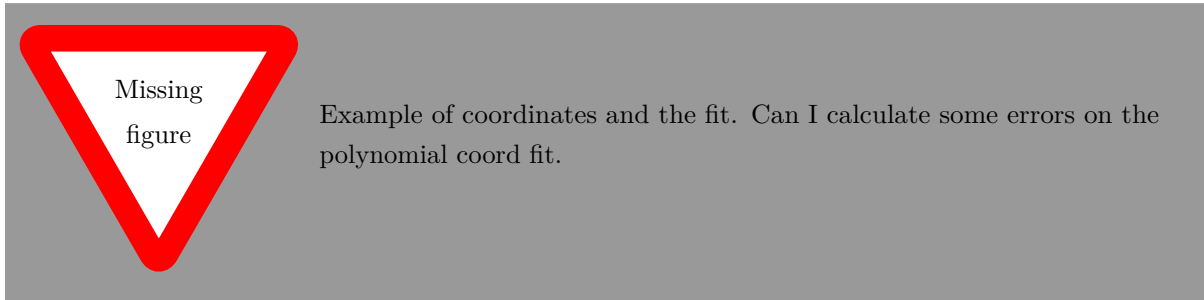


**Figure 3.8:** Wavelength calibration example. The equation of the fitted line for these points is  $\lambda = -1.85e^{-7}x^2 + 1.16e^{-2}x + 2111.86$  with each coefficient shown to two decimal places only. Error bars the line width set to around 0.04 nm.



explain the fit  
Figure 3.8

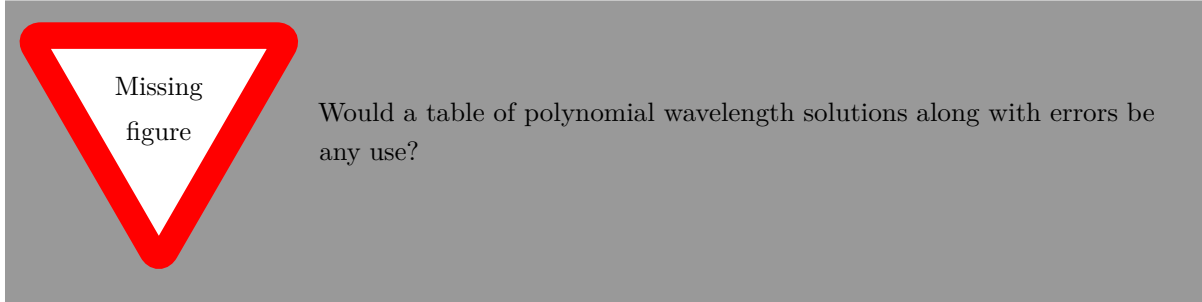
Much like with the Th-Ar calibrations, this technique performs better when there is sufficient coverage of telluric lines on the detectors. For the wavelength setting of these observations, the spectra from the second detector (top right panel of Figure 3.9) only have two large telluric lines present with several small lines, with relative depths smaller than 1%, which are often difficult to accurately identify. This deteriorated the calibration stability for the second detector. With the lack of telluric contamination and stellar lines on the second detector it may have been ideal for the detection of a faint secondary spectra; unfortunately the wavelength calibration quality varies in an inverse way.

We note that there are many variations on this wavelength calibration technique including those integrated within programs such as *TelFit* Gullikson et al. (2014), and ESO's *Molecfit* Smette et al. (2015), that perform telluric correction and re-calibrate the wavelength axis themselves at the same time.

One improvement that would have been to include a concurrent fitting of a stellar spectral model, adjusted for RV, along with the telluric model could help to improve the wavelength calibration performed here. Piskorz et al. (2016) performed wavelength calibration using only a telluric line model at other

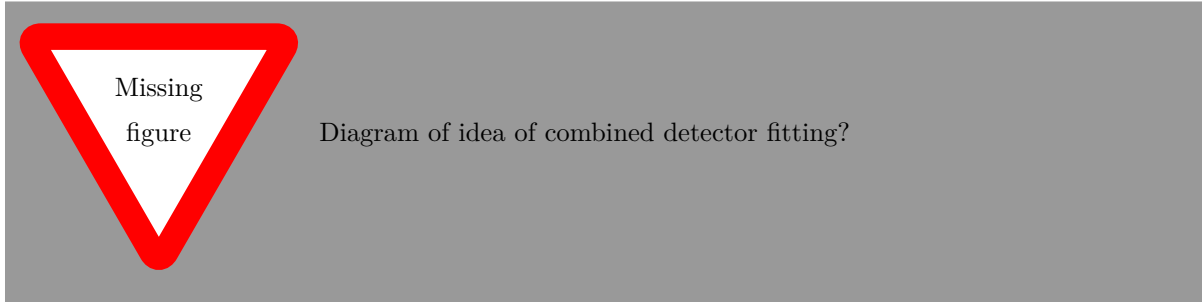
nIR wavelengths (e.g. 3.0–3.4 μm) successfully. However, around 2 μm they needed to include a fitted stellar model to obtain good wavelength calibration due to the weaker telluric lines in this region. This is the same wavelength region of the data analysed here. Having experience of performing wavelength calibration at other wavelengths may have revealed the difficulties of calibration from the telluric lines at 2 μm sooner.

A brief attempt of wavelength calibration using an iterative method outlined in Brogi et al. (2016). This involved generating set of quadratic wavelength solutions for the observed spectrum and cross-correlating each one against the telluric model. The solutions for the next iteration are obtained by refining the parameters from the wavelength solution with the highest correlation. The method worked well for Brogi et al. (2016) as they included templates for both star and telluric lines were observing in a wavelength domain in which there is a large number of strong and uniform stellar rCOlines across the detector. Our brief experiments with this method were not successful as we did not include a stellar model or mask. Without adding any stellar masking the telluric lines would strongly correlate to the stellar lines present, especially were there were blended lines. This lead to visibly incorrect wavelength solutions and this method was abandoned. If a stellar mask was used it may have been possible to achieve more sensible results, although still challenging to the low density of telluric lines at this wavelength range.



Add pictures of wavelength calibrations

At one point it was considered to attempt a global fit of the wavelength calibration, using all four CRIRES detectors together. This would be one consistent fit to the dispersion across all 4 detectors at once. This would required extra fitting parameters such as the 3 gaps between the detectors and any vertical offsets. This may even need to be performed on the two-dimensional images, before extraction. What this may have allowed for the telluric lines from neighbouring detectors would help to fit the calibration on detectors where there are very few telluric lines (e.g. detector 2). The fitted instrument parameters such as the detector gaps may even be constrained by so that they are physically consistent across all observations. However, this idea was not explored further or implemented due to time constraints.



An example of the wavelength calibration using all 4 detectors is provided in Appendix B.

In the future it may be possible or necessary to combine all of the methods above, including the

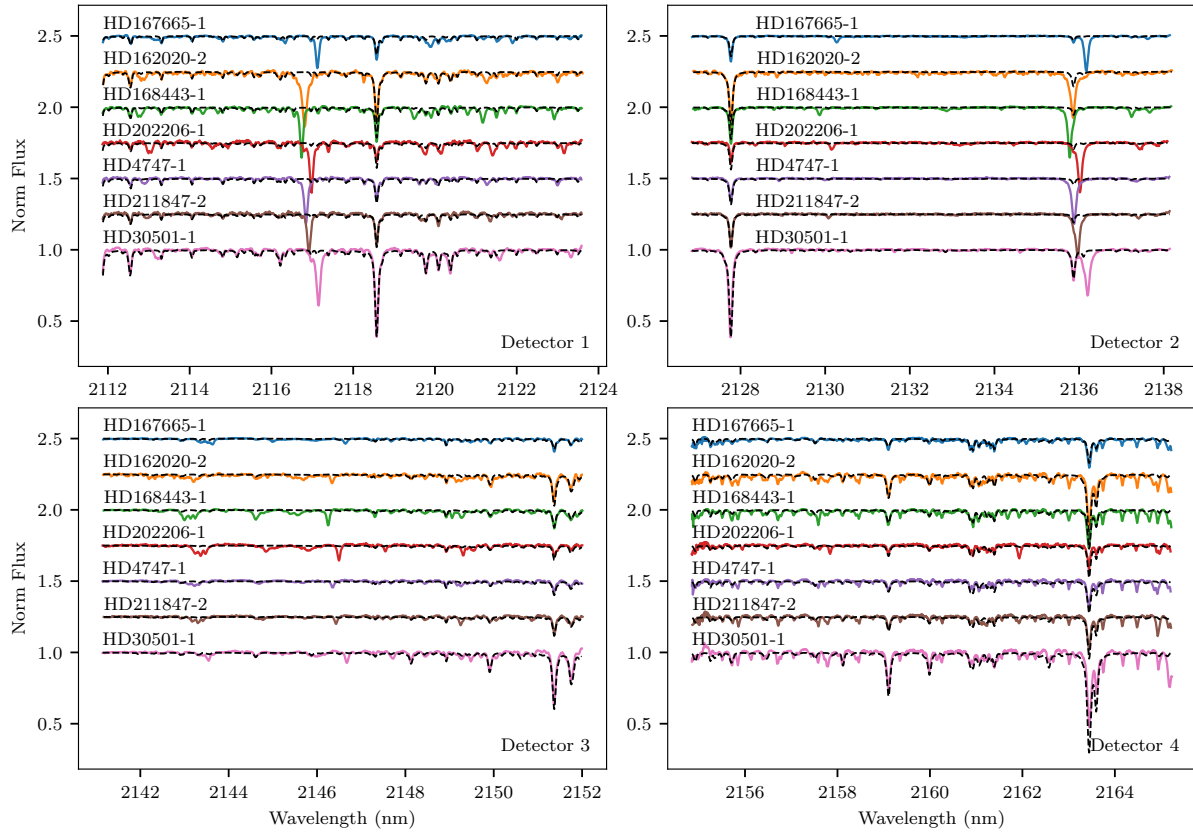
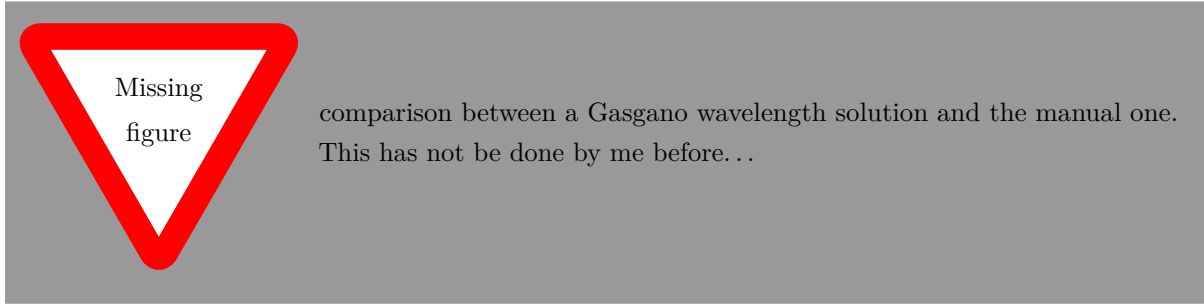


**Figure 3.9:** An example spectra for each target and each detector 1–4 in order of increasing wavelength. The solid lines are the spectra while the black dashed lines are the telluric models used for wavelength correction, showing good alignment with the spectra.

Th-Ar calibration lines, telluric models, stellar templates, and multiple detectors fitted at once to achieve accurate calibration.



In hindsight using the wavelength solution from the ESO pipeline may have been a good starting point, rather than the pixel positions, for calibration of the DRACS reduced spectra. This may have made the line identification simpler.

See Solene's paper regarding Telluric correction with models and reference spectra

### 3.4.1.1 Telluric correction

The Earth's atmosphere is a spectral filter for all ground-based astronomical observations, imprinting the absorption profile of the atmosphere onto the spectrum observed. To accurately recover the spectra of

the observed target the removal of the absorption lines introduced by Earth's atmosphere is extremely important. The motion, changing composition and . A number of methods are available to correct for the telluric lines, telluric reference (cite), models (tapas), modelling/fitting (molecfit tellfit). The effectiveness between these three methods has recently been performed in Ulmer-Moll et al. (2018). . .

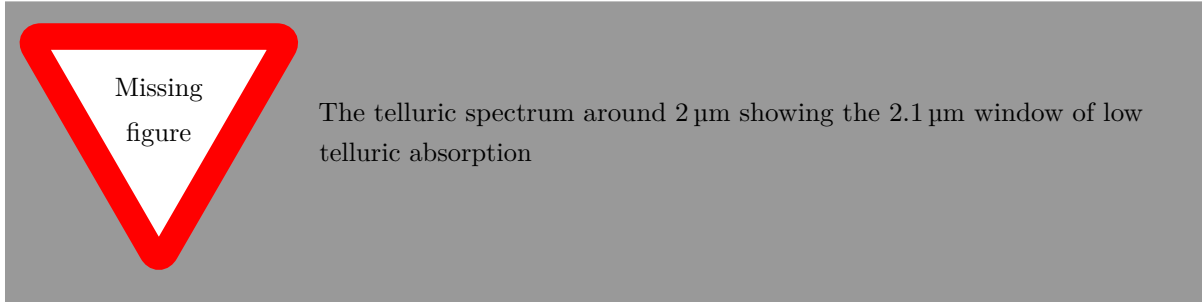
See solenes paper for material here

Expand this section...

Should this be more in the introduction?

In this work we use telluric models without fitting, using the TAPAS spectra.

These observations were first taken in an atmospheric window of the *K*-band in order to reduce the absorption introduced by the atmosphere (Barnes et al., 2008).



To correct for the remaining telluric line contamination the spectra were divided by the TAPAS(Bertaux et al., 2014) atmospheric transmission models for each observation. Synthetic telluric models were used to avoid the observing overhead necessary to perform telluric standard star exposures (Vacca et al., 2003), and they have been demonstrated to be superior in the quality of the correction relative to the telluric standard approach (e.g., Cotton et al., 2014).

Before the correction, the depth of the telluric lines were re-scaled to match the airmass of the observation using the relation  $T = T^\beta$ , where  $T$  is the telluric spectrum and  $\beta$  is the airmass ratio between the observation and model. This changed the depth of most absorption lines to match the observations, but does not correctly scale the deeper  $\text{H}_2\text{O}$  lines. The scaled telluric model is interpolated to the wavelengths of the observed spectrum and then used to correct the observed spectra through division, leaving behind a telluric corrected spectra. An example of a telluric corrected spectra is shown in the middle panel of Figure 4.1, with the light blue shading indicating where the deeper telluric lines were.

We attempted the technique suggested by Bertaux et al. (2014) to address the poor  $\text{H}_2\text{O}$  airmass scaling, to fit a scaling factor to the  $\text{H}_2\text{O}$  absorption lines before convolution to the instrument resolution. This was achieved by first dividing the spectrum by a telluric model with only non- $\text{H}_2\text{O}$  constituents, convolved to the observed resolution, and scaled by the airmass to remove the non- $\text{H}_2\text{O}$  lines. Then a model with only  $\text{H}_2\text{O}$  lines at full resolution was scaled by a factor  $T^x$ , convolved to  $R = 50\,000$  and compared to the observed spectra. The factor  $x$  was fitted to find the best scaling factor for the  $\text{H}_2\text{O}$  lines.

We found that for a few spectra in our sample this method corrected the deeper telluric lines well, but in many cases we found that the fitted scaling factor was affected by the presence of blended stellar lines (attempting to fit those also). It was also strongly influenced by the deepest  $\text{H}_2\text{O}$  telluric lines present. We find that the telluric correction of the deep  $\text{H}_2\text{O}$  lines could be improved with this technique, but at the cost of worsening the correction of the many smaller  $\text{H}_2\text{O}$  lines. Since the smaller  $\text{H}_2\text{O}$  lines covered more of the spectrum in this region than the larger lines we chose not to continue with this separate  $\text{H}_2\text{O}$  scaling. One possible solution for this would be to perform a piece-wise telluric correction, performing this step only for the deeper  $\text{H}_2\text{O}$  lines, or by using one of the other tools that fits the telluric model to the observations. This technique could also benefit from a larger wavelength span that would

enable blended lines to be ignored while having sufficient deep H<sub>2</sub>O lines to fit the scaling factor correctly. This small experiment shows that a simple scaling is not enough to correct for the absorption in an effective way, for this case.

example of good and bad fitting...

### 3.4.2 Tapas models

For the wavelength calibration and telluric correction methods we use telluric line models. These have been shown to provide as good or better telluric correction compared to the telluric standard method and (Ulmer-Moll et al., 2018).

We utilized the TAPAS (Transmissions of the AtmosPHERE for ASTRonomical data) web-service<sup>22</sup> (Bertaux et al., 2014) to obtain atmospheric transmission models for each observation. TAPAS uses the standard line-by-line radiative transfer model code LBLRTM (Clough and Iacono, 1995) along with the 2008 HITRAN spectroscopic database (Rothman et al., 2009) and ARLETTY atmospheric profiles derived using meteorological measurements from the ETHER data center<sup>23</sup> to create telluric line models.

The ARLETTY atmospheric profiles have a 6 hour resolution, so there may be a slight difference between the actual profile at the time of observation.

We use the mid-observation time to retrieve transmission models for each observation, with the ARLETTY atmospheric profiles<sup>24</sup> and vacuum wavelengths selected. The telluric models were retrieved without any barycentric correction to keep the telluric lines at a radial velocity of zero with respect to the instrument.

TAPAS allows for the choice of atmospheric constituents included in the model spectra. We obtained one model with all available species present, convolved to a resolution of R = 50 000, and another two models without an instrumental profile convolution applied. For these two extra models, one contained only the transmission spectra of H<sub>2</sub>O while the other contained all other constituents except H<sub>2</sub>O. This was to explore a known issue with the depth of H<sub>2</sub>O absorption lines in the TAPAS Bertaux et al. (2014). Section 3.4.1.1.

### 3.4.3 Issues with TAPAS

There are a number of issues we encountered when using TAPAS web-service, mainly due to interaction with the website. Often their service was down for weeks at a time without any warning or notification. With this you would waste time filling out the web form and attempt to submit it but would receive no response and no email with a link to the data. There was a higher success rate of successful response between different web-browsers. A number of bug reports were submitted to the owners of the webpage without any acknowledgement.

The web-page is useful for quickly obtaining a small number of spectra but can be tedious for many. In our case we were requesting 3 telluric spectra, with varying molecular contributions, for each of our 17 observations. There is an ability to request multiple spectra at a time but we found this would not function if trying to request more than 4 spectra at once.

Add telluric spectra for NIR band? the plot from Molecfit?

Still uneven line coverage on all detectors in this small range

H<sub>2</sub>O corrections

ADAPT this section to the usage of the models.

telluric model correction methods original

<sup>22</sup> <http://www.pole-ether.fr/tapas/>

<sup>23</sup> <http://www.pole-ether.fr>

<sup>24</sup> Nearest of the 6 hourly profiles

A script<sup>25</sup> was created to automatically generate the data necessary to fill out the a TAPAS request for each CRIRES observations. The script scanned the CRIRES header for information such as the mid-time of observations, target coordinates, slit width (defines CRIRES's instrumental resolution) etc. and populated the XML request form provided by TAPAS. The script output is copied and pasted into the web-browser for submission.

Trial and error was needed to understand all the XML form entries, such as the molecules requested and the atmospheric model to use (ARLETTY) and achieve a valid TAPAS request. The real issue was with the TAPAS ID number. Each TAPAS request has an ID number (which is provided with the email response). This ID number needs to be correctly set in the XML form before submission. This number increments by 1 with each submission but its initial value is unknown unless you made the last request. If you submit the XML request with the incorrect ID number you will get a response with the correct ID number, but the failed request. You increment this ID number by 1 and hopefully make a valid request. Unfortunately if someone else has made a TAPAS request after yours then the ID number will again be invalid. It is unknown whether multiple transmission spectra could have been requested at the same time with the XML form.

There is another issue with a one hour time offset between the requested and the time returned by TAPAS. For instance if the requested time was for an observation at 0200h UTC then the transmission spectrum returned by TAPAS is for 0100h UTC. This changes the position of the target, the airmass and potentially the ARLETTY model used (6 hour time steps), affecting the strength of the telluric lines. It is tedious to remember to offset your input time by one hour to obtain the correct time, and slightly more work when you also have to adjust the date when going backwards past 0000h. When submitting the XML script the time that is returned is the time requested. Attempts were made to bring this issue to the attention of the TAPAS team in 2016 but as of August 2018 this issue is still present.

These issues need to be considered when requesting TAPAS spectra, adding unnecessary difficulty to the relatively simple process.

### 3.4.3.1 Telluric masking

The telluric spectra from TAPAS can not only be used for correcting individual spectra but are also easily used to create a wavelength mask telluric lines. For instance Figueira et al. (2016) and Artigau et al. (2018) use TAPAS spectra to mask out atmospheric lines deeper than 2% for the computation of photon noise precision of radial velocity measurements. Masking with the TAPAS models is similarly performed in Chapter 6 when we extend the analysis of Figueira et al. (2016). The telluric model used for this is an average of 52 TAPAS spectra (one per week in 2014), simulated at La Silla Observatory at an airmass of 1.2 ( $z = 33.5^\circ$ ). This is to incorporate long-term variations of absorption over the year. Masking is applied by defining a cut-off line depth, typically 2%, at which to mask out any deeper telluric lines.

### 3.4.4 Wavelength masking

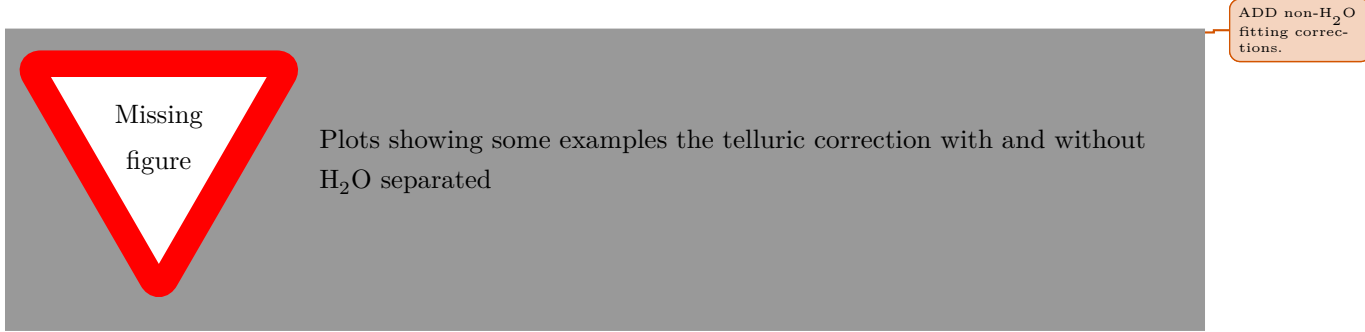
Throughout the course of this work several wavelength regions were found where we cannot reliably extract information, due to the wavelength calibration and telluric line corrections. We apply different wavelength masks to these areas to remove them from the spectra. We collate the main reasons for the wavelength masking below, although these masks are not always used for all analysis.

<sup>25</sup> Available at <https://github.com/jason-neal/equanimous-octo-tribble/blob/master/octotribble/Tapas/>

Firstly, regions near the edges of each detector where the wavelength solution is extrapolated outside of the calibrating telluric lines are removed, reducing the effective size of each detector by about 10% or  $\sim 100$  pixels.

Secondly, we mask out any remaining artefacts present in the spectra and the centres of deep telluric lines where telluric correction was not corrected properly, sometimes resulting in “emission-like” peaks in the corrected spectrum. These factors combined result in masking out around a further 10% of the observed spectra.

In Section ?? we also apply a further wavelength restriction to mask out regions where there is a large mismatch between the observed spectrum and the closest synthetic spectra to the host. This significantly restricts the wavelength span utilized for that purpose to around only 43%. The masked regions caused created by this last mask are shown in Figure 5.4.



### 3.4.5 Barycentric correction

The orbital and rotational motion of the Earth imparts a daily and seasonal radial velocity signal offset onto observations. The maximum barycentric velocity is around  $30 \text{ km s}^{-1}$ .

After the telluric correction is performed, the spectra are corrected for Earth’s heliocentric motion by Doppler shifting the spectrum by the negative value of the barycentric velocity calculated, placing all spectra as if they were observed from the reference point of the Sun.<sup>26</sup> The barycentric velocity is calculated using PyAstronomy’s<sup>26</sup> *helcor* function ported from the REDUCE IDL package (see Piskunov and Valenti (2002)). This calculates radial velocity of the observatory towards the astronomical target, accounting for Earth’s barycentric motion around the Sun as well as Earth’s rotation. This computation requires the date and time of the observation, the location of the observatory and the celestial coordinates of the target.

<sup>26</sup> <https://pyastronomy.readthedocs.io>

# Chapter 4

## Direct Spectral Recovery

There are many different techniques to disentangle the spectra of binary objects. In this chapter we focus on applying a direct subtraction method to near-infrared (nIR) spectra of FGK stars with Brown Dwarf (BD) companions. The data used was obtained with the CRIRES instrument in 2012 with the purpose to apply this technique specifically. A level of trust was placed in the quality of the observations, which was misplaced. We will begin this chapter with the motivation for these specific targets and detail the observations obtained. We will then present the direct subtraction technique and explore in detail how the observations are insufficient to apply this method, and explore this technique at low RV separations by comparison to simulated results.

### 4.1 Motivation

Motivation section

**Why this technique and not others.** - separation of components - direct imaging (can't separate)

Find direct imaging limitations —

### 4.2 Motivation and target selection

The work of Sahlmann et al. (2011) identified several candidate brown dwarf companions of FGK stars with  $M_2 \sin i$  values  $> 10 M_{\text{Jup}}$ . Seven candidates from Sahlmann et al. (2011), which were visible in Period 89 (2012), were selected for further observation in order to identify their stellar nature. That is, to refine the mass of the companions to distinguish if they companion is a large giant planet ( $M \lesssim 13 M_{\text{Jup}}$ ), a Brown dwarf ( $13 \lesssim M \lesssim 80 M_{\text{Jup}}$ ) or a low-mass star ( $M \gtrsim 80 M_{\text{Jup}}$ ).

The spectral differential approach was chosen with the goal to constrain the companion masses while minimizing the observational time required to observe. It was deemed that it should be possible to obtain a detection of a companion at 1% contrast ratio with an exposure time of around 20 minutes. Two observations at “clearly separate RVs” were requested to constrain each target. Observations were performed without telluric standard star observations to avoid the wasted observing time, choosing to instead rely on synthetic model correction (see 3.4.1.1). The  $K$ -band was chosen to achieve a high contrast relative to the host star, detected in the extreme V-K colour indexes ( $> 7.8$ ).

**Table 4.1:** Stellar parameters of the host stars. V is the apparent magnitude taken from SIMBAD (Wenger et al. 2000). Distances were calculated from the GAIA DR2 parallax measurements.

Star	SpT	V	$T_{\text{eff}}$ (K)	$\log g$ (cm s $^{-2}$ )	[Fe/H]	$M_1$ (M $_{\odot}$ )	Age (Gyr)	d (pc)	Ref
HD 4747	K0V	7.15	$5316 \pm 50$	$4.48 \pm 0.10$	$-0.21 \pm 0.05$	$0.81 \pm 0.02$	$3.3 \pm 2.3$	$18.80 \pm 0.04$	1, 2
HD 162020	K3V	9.12	$4723 \pm 71$	$4.31 \pm 0.18$	$-0.10 \pm 0.03$	$0.74 \pm 0.07$	$3.1 \pm 2.7$	$30.85 \pm 0.06$	4, 5
HD 167665	F9V	6.40	$6224 \pm 50$	$4.44 \pm 0.10$	$0.05 \pm 0.06$	$1.14 \pm 0.03$	$0.7 - 3.6$	$31.24 \pm 0.06$	
HD 168443	G6V	6.92	$5617 \pm 35$	$4.22 \pm 0.05$	$0.06 \pm 0.05$	$1.01 \pm 0.07$	$10.0 \pm 0.3$	$39.67 \pm 0.12$	5, 6
HD 202206	G6V	8.07	$5757 \pm 25$	$4.47 \pm 0.03$	$0.29 \pm 0.02$	$1.04 \pm 0.07$	$2.9 \pm 1.0$	$46.03 \pm 0.14$	5, 7
HD 211847	G5V	8.62	$5715 \pm 24$	$4.49 \pm 0.05$	$-0.08 \pm 0.02$	$0.92 \pm 0.07$	$0.1 - 6.0$	$48.81 \pm 0.13$	1, 2, 3
HD 30501	K2V	7.59	$5223 \pm 50$	$4.56 \pm 0.10$	$0.06 \pm 0.06$	$0.81 \pm 0.02$	$0.8 - 7.0$	$20.37 \pm 0.01$	1, 2

References: (1) Sahlmann et al. (2011); (2) Santos et al. (2005); (3) Crepp et al. (2016); (4) Tsantaki et al. (2013); (5) Hirsch et al. (2016); (6) Santos et al. (2004); (7) Sousa et al. (2008); (8) Collaboration et al. (2018);

**Table 4.2:** Orbital parameters for the BD companions obtained from the literature. Yes need rotating.

Object	$\gamma$ (km s $^{-1}$ )	Period (day)	$e$	$K_1$ (m s $^{-1}$ )	$T_0$ (JD-2,450,000)	$\omega$ (deg)	$M_2$ (M $_{\text{Jup}}$ )
HD 4747	$0.215 \pm 11$	$13\,826.2 \pm 314.1$	$0.740 \pm 0.002$	$755.3 \pm 12$	$463.1 \pm 7.3$	$269.1 \pm 0.6$	
HD 162020	$-27.328 \pm 0.002$	$8\,428.19 \pm 6e^{-5}$	$0.277 \pm 0.002$	$1\,813 \pm 4$	$1\,990.68 \pm 0.01$	$28.4 \pm 0.2$	
HD 167665	$8.003 \pm 0.008$	$4\,451.8 \pm 27.6$	$0.340 \pm 0.005$	$609.5 \pm 3.3$	$6\,987.6 \pm 29$	$-134.3 \pm 0.9$	
HD 168443b	$-0.047 \pm 0.552$	$58.1124 \pm 4e^{-4}$	$0.529 \pm 0.001$	$475.13 \pm 0.9$	$5\,626.20 \pm 0.02$	$172.9 \pm 0.1$	
HD 168443c	$-0.047 \pm 0.552$	$1\,749.83 \pm 0.57$	$0.211 \pm 0.002$	$297.7 \pm 0.6$	$5\,521.3 \pm 2.2$	$64.9 \pm 0.5$	
HD 202206B	14.721	256.33 ± 0.02	0.432 ± 0.001	567 ± 1	2 176.14 ± 0.12	161.9 ± 0.2	
HD 202206c	14.721	1 260 ± 11	0.22 ± 0.03	41 ± 1	3 103 ± 452	280 ± 4	
HD 211847	6.689 <sup>a</sup>	$7\,929.4 \pm 2\,500$	$0.685 \pm 0.068$	$291.4 \pm 12.2$	$12\,030.1 \pm 2\,500$	$159.2 \pm 2.0$	
HD 30501	$23.710 \pm 0.028$	$2\,073.6 \pm 3.0$	$0.741 \pm 0.004$	$1\,703.1 \pm 26.0$	$3\,851.5 \pm 3.0$	$70.4 \pm 0.7$	

**References.** (1) Crepp et al. (2016); (2) Udry et al. (2002); (3) Sahlmann et al. (2011); (4) Pilyavsky et al. (2011); (5) Correia et al. (2005); (6) Benedict and Harrison (2017); (7) Moutou et al. (2017)

**Notes.** <sup>(a)</sup> fixed

The list target host stars are presented in Table 4.1 along with their stellar parameters, while the companion orbital parameters are provided in Table 4.2.

We note that the orbital parameters of some targets have been refined in the literature since the observations took place. For example three candidates have had their masses refined in recent works. The companion to HD 211847 was determined to be a low mass star with  $M_2 = 155 M_{\text{Jup}}$  (Moutou et al., 2017), while the companion to HD 4747 was found to have a mass of  $M_2 = 60 M_{\text{Jup}}$  (Crepp et al., 2016). The two companions of HD 202206 (B and c) were found to have masses of  $M_B = 93.6 M_{\text{Jup}}$  and  $M_c = 17.9 M_{\text{Jup}}$ , respectively, classifying HD 202206c as a “circumbinary brown dwarf” (Benedict and Harrison, 2017). These three target with recently refined masses (along with HD 30501) create a good set benchmarks to compare any results from the techniques developed here, and show that the masses of these targets do span the BD – low mass star range. All target companions except HD 162020 ( $P=8.4$  days) are in (very) long period orbits ( $P=0.7-38$  years) with masses (or  $M_2 \sin i$ ) greater than  $10 M_{\text{Jup}}$ .

Rotate orbital parameter table.

### 4.2.1 The Data

#### 4.2.2 CRIRES data

Observations were performed with the CRIRES instrument (Kaeufl et al., 2004) configured to observe a narrow wavelength domain of the *K*-band between 2120–2160 nm. The slit width of  $0.4''$  resulted in an instrumental resolving power of  $R = 50\,000^1$ . No adaptive optics were used to ensure that the entrance slit was entirely covered by each target. This is to prevent strong slit illumination variations that could change the shape of spectral lines.

The observations were performed in service mode during Period 89 with run ID. 089.C-0977(A) between April and August 2012. A single observation is composed of eight individual spectra with an integration time of 180s each, observed in the ABBAABBA nod cycle pattern to obtain a high signal-to-noise ( $>100$ ) when combined. The list of observations obtained with CRIRES are provided in Table 4.3.

There is a slight inconsistency with some of the observations, taken in service mode. For instance HD 202206 has two observations taken with the Ks filter, while one is taken with the J filter. There is also the last observation of HD 30501 taken with a different filter to the rest. We are unable to access the phase two proposal to determine if this was requested as such or it was an observational mistake.

There is also a inconsistency with the ordering of the observations again with HD 202206. The observation that was performed first is labelled as the third in the fits header file.

The target HD 4747 only has one observation. There could be two possible reasons for this, these observations were preformed in service mode as filler and there was time to complete it, or only one observation was requested due to the very long orbital period of the target.

**Is there a reason for the two different filters?**

**The filters ... using the Ks and the Hx5e-2 filters. Why use the different filters???**

All observations were reduced using the DRACS pipeline (see Section 3.3.3) with artefact corrections applied. They were each wavelength calibrated and corrected for telluric lines following Sections 3.4.1 and 3.4.1.1. The spectra were corrected for Earth's barycentric RV using the *helcor* PyAstronomy<sup>2</sup> function ported from the REDUCE IDL package (see Piskunov and Valenti (2002)). Using the date and coordinates of the targets this function calculates the induced RV from the orbital motion of the Earth around the Sun as well as the rotation of the Earth, projected towards the target. This calculated RV is then used to apply the appropriate Doppler shift on each spectrum to correct for the Earth's barycentric motion.

#### 4.2.3 Calculations using observed times

Before the differential subtraction method is presented, calculations can be performed to estimate the RV of both components in each observations and the likely separation between the companions between observations. The time of each observation is combined with the orbital parameters from Table 4.2 and Equation ?? to calculate the RV of the host star ( $RV_1$  in 4.3). For the companion the mass or  $M_2 \sin i$  is used alongside the stellar mass from possible from Table ?? to calculate the RV of the companion using

<sup>1</sup> The rule of thumb resolution for CRIRES is  $100\,000 \frac{0.2''}{slitwidth}$

<sup>2</sup> <https://pyastronomy.readthedocs.io>

I still assume this is a mistake

Check why the ordering number is incorrect for HD202206. If it is correct like this and is numbered incorrectly in the header then we should mention this.

rotate table?

I am not sure if this is the best location for this section.

**Table 4.3:** Details about the each CRIRES observation. The number of artefacts removed in Section 3.3.3.1 as well as the SNR of the combined spectra is provided. The last three columns are the calculated RV of both host and largest companion, from the orbital solution, as well as the RV difference between the two components.

Object	Obs. #	Start date (yyyy-mm-dd hh:mm:ss)	Filter	Airmass (at start)	Artefacts / 32	SNR	$RV_1$ $\text{km s}^{-1}$	$RV_2$ $\text{km s}^{-1}$	$rv_2$ $\text{km s}^{-1}$
HD 4747	1	2012-07-06 07:36:06	Ks	1.25	7	340	-0.219	-0.154	0.065
HD 162020	1	2012-07-04 06:23:22	Ks	1.30	2	127	-28.760	50.785 <sup>a</sup>	79.545 <sup>a</sup>
HD 162020	2	2012-07-04 06:57:48	Ks	1.44	2	128	-28.717	48.440 <sup>a</sup>	77.157 <sup>a</sup>
HD 167665	1	2012-07-28 05:00:53	Hx5e-2	1.24	7	371	7.581	18.024 <sup>a</sup>	10.443 <sup>a</sup>
HD 167665	2	2012-07-28 05:37:27	Hx5e-2	1.39	4	374	7.581	18.025 <sup>a</sup>	10.444 <sup>a</sup>
HD 167665	3	2012-08-05 02:54:03	Hx5e-2	1.04	4	358	7.575	18.163 <sup>a</sup>	10.588 <sup>a</sup>
HD 168443	1	2012-08-05 04:29:32	Ks	1.31	2	192	-0.121	50.932 <sup>a,b</sup>	51.053 <sup>a,b</sup>
HD 168443	2	2012-08-05 04:58:50	Ks	1.47	4	190	-0.121	51.189 <sup>a,b</sup>	51.310 <sup>a,b</sup>
HD 202206	1	2012-07-12 06:54:44	Ks	1.01	3	189	14.843	12.992 <sup>b</sup>	-1.851
HD 202206	2	2012-07-13 05:41:40	J	1.01	3	209	14.837	13.065 <sup>b</sup>	-1.772
HD 202206	3	2012-07-11 08:29:55	Ks	1.15	4	180	14.849	12.920 <sup>b</sup>	-1.929
HD 211847	1	2012-07-06 07:02:57	Ks	1.07	4	272	6.613	7.171	0.558
HD 211847	2	2012-07-13 06:54:37	Ks	1.05	5	283	6.614	7.167	0.553
HD 30501	1	2012-04-07 00:08:29	Hx5e-2	1.60	3	217	22.372	36.377	14.005
HD 30501	2	2012-08-01 09:17:30	Hx5e-2	1.42	10	212	22.505	35.120	12.615
HD 30501	3	2012-08-02 08:47:30	Hx5e-2	1.53	8	237	22.507	35.102	12.595
HD 30501	4	2012-08-06 09:42:07	Ks	1.28	7	235	22.514	35.031	12.517

<sup>a</sup> Maximum RV given  $M_2 \sin i$  only.

<sup>b</sup> Largest mass companion only.

Equation ?? ( $RV_2$  in 4.3). The difference in RV between the host and companion each observation is also computed as  $rv_2 = RV_2 - RV_1$  although it will not be used until 5.

The magnitude of the RV separation of the two companion spectra in the differential  $\Delta RV$  is calculated following Equation 4.5 and provided in 4.4. This table also contains the estimated semi-major RV amplitude for the companion  $K_2$  and the phase coverage from the observations. The phase coverage is the fraction of the orbit covered between the observations for each target. For HD 4747 the  $\Delta RV$  and phase coverage values are missing due to a single observation.

equations for companion rv with the masses still included. include 180 degree angle phase change also

The full orbital solution for the components along with the times of observations are provided later in Section 4.4.

Fix caption position here

recalculate values that are less than 1

### 4.3 Direct Subtraction Method

Here we present the direct subtraction method used, which is similar to previous works (Ferluga et al., 1997; Kostogryz et al., 2013). Assuming that the instrumental profile and atmospheric absorption are dealt with appropriately the spectra of the observed targets are assumed to be composed of two components. A bright host star blended with the faint companion. The spectrum received from the host-companion pair is given by the superposition of two spectral components ( $J_1, J_2$ ):

$$I(\lambda) = J_1(\lambda - v_1) + J_2(\lambda - v_2) \quad (4.1)$$

**Table 4.4:** Estimated orbital semi-amplitude and RV separation of the companion, given the companion mass ( $M_2$  or  $M_2 \sin i$ ) from Table 4.2 and observation times from Table 4.3.

Companion	Estimated $K_2$ ( $\text{km s}^{-1}$ )	Estimated $ \Delta RV $ ( $\text{m s}^{-1}$ )	Phase coverage (%)
HD 4747	-10.65	—	—
HD 162020	-98.92 <sup>a</sup>	2 388	0.28
HD 167665	-14.47 <sup>a</sup>	145	0.18
HD 168443b	-64.65 <sup>a</sup>	258	0.035
HD 168443c	-18.05 <sup>a</sup>	<1	0.001
HD 202206B	-6.79	78	0.74
HD 202206c	-2.50	<1	0.15
HD 211847B	-1.85	5	0.09
HD 30501	-16.12	1 410	5.8

<sup>a</sup> Maximum  $K_2$  only given  $M_2 \sin i$

where the subscripts 1 and 2 indicate the spectrum of the host and companion respectively, and  $\lambda$  represents the wavelength of the spectra and  $\lambda - v$  represents the Doppler shift  $\lambda(1 - v/c)$  by a velocity  $v$ .

This can be shifted into the rest frame of the host star by applying the shift  $v_1$ :

$$I(\lambda + v_1) = J_1(\lambda) + J_2(\lambda - v_2 + v_1) \quad (4.2)$$

To analyse  $J_2$ , the spectral component of interest, the component from the host needs to be carefully removed. If two observations of the same target are observed, denoted with subscripts  $a$  and  $b$ , there will be relative motion between the components due to the orbit. Assuming that the stellar spectra do not change over time ( $J_{1a} = J_{2a}$ ) and each spectrum can be individually Doppler shifted to the rest frame of the host star  $J_1\lambda$ , then the spectrum of the host star ( $J_1$ ) can be removed through subtraction of the two observations. Mutually cancelling the host component while leaving two components of the companion, with a relative Doppler shift between them.

$$\begin{aligned} S(\lambda) &= I_a(\lambda + v_{1a}) - I_b(\lambda + v_{1b}) \\ &= (J_{1a} + J_{2a}(\lambda - v_{2a} + v_{1a})) - (J_{2b} + J_{2b}(\lambda - v_{2b} + v_{1b})) \\ &= J_{2a}(\lambda - v_{2a} + v_{1a}) - J_{2b}(\lambda - v_{2b} + v_{1b}) \end{aligned} \quad (4.3)$$

$$S(\lambda + v_{2a} - v_{1a}) = J_{2a}(\lambda) - J_{2b}(\lambda - v_{2b} - v_{1a} + v_{1b} + v_{2a}) \quad (4.3)$$

$$S(\lambda') = J_{2a}(\lambda) - J_{2b}(\lambda - \Delta RV_2) \quad (4.4)$$

where,

$$\Delta RV_2 = v_{1a} - v_{1b} - v_{2a} + v_{2b} \quad (4.5)$$

is the RV difference between the two companion spectral components when the host components are mutually subtracted. and  $\lambda' = \lambda + v_{2a} - v_{1a}$

The resulting differential spectra  $S\lambda'$ , dubbed *s-profile* by Ferluga et al. (1997), is composed of just

the companion spectra, shifted and subtracted from itself.

Ferluga et al. (1997) even provide a analytical form for the *s-profile* given a single Gaussian line of the form  $J(\lambda) = 1 - D \cdot \exp^{-\pi(\lambda-\lambda_0)^2/W^2}$ : ....

$$S(\lambda) = 2D \cdot \exp^{-\pi D^2[(\lambda-\lambda_0)^2+(k/2)^2]/W^2} \cdot \sinh \frac{\pi D^2(\lambda-\lambda_0)k}{W^2}, \quad (4.6)$$

where  $\lambda_0$ ,  $D$ , and  $W$  are the central wavelength, depth and equivalent width of the Gaussian line, and  $k = \Delta RV_2$  is the shift between the two companion spectra.

From binary dynamics (e.g., Murray and Correia, 2010) the RV amplitudes of the host and companion are related through the mass ratio,  $q$ , while having an opposite sign<sup>3</sup>:

$$v_2 = -q * v_1 \quad (4.7)$$

We can simplify Equation 4.5 by expressing it in terms of the mass ratio and host RV only:

put in advanced concepts chapter???

this ignores  $\gamma$

$$\begin{aligned} \Delta RV_2 &= qv_{1a} - qv_{1b} + v_{1a} - v_{1b} \\ &= (1+q)(v_{1a} - v_{1b}). \end{aligned} \quad (4.8)$$

If the  $\Delta RV_2$  between the companion spectra is able to be derived from the s-profile (see Ferluga et al., 1997) then the mass ratio of the system,  $q$ , can determined, thereby constraining the mass of the companion.

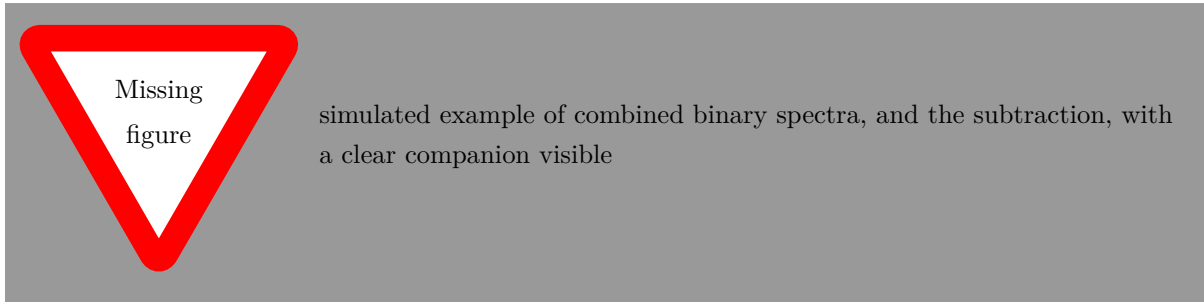
The values  $v_{1a}$  and  $v_{1b}$  are radial velocity of the host components. The values we use calculated using the RV equation 2.1 using the orbital parameters from the literature and provided in 4.2 and are used to shift each spectra to the hosts rest frame. These components can also be determined directly from the spectrum by cross-correlating the observed spectrum with a stellar template of the host and were in reasonable agreement. The same values already used to shift and mutually cancel the host spectrum.

There should be checks for consistency between  $v_{1a}$ ,  $v_{1b}$  and how well the host component is removed in the s-profile.

**If v1a and v1b are incorrect what will happen to q?**

put elsewhere: Equation 4.7 was used to calculate the expected companion RV for each observation in Table 4.3.

Example simulations?



kostov.. 2013 use a very similar method, choosing two observations from the extrema. They also preform a number of simulations regarding observing CRIRES spectra with

<sup>3</sup> The opposite sign arises from a  $180^\circ$  difference in the angle of periapsis,  $\omega$ , for the companion.

different brown dwarfs. Figure our the flux ratio limit they get too???

### 4.3.1 Results of spectral differential analysis

We applied the spectral differential procedure outlined above on the wavelength-calibrated and telluric-corrected CRIRES observations. The spectra were first Doppler shifted to the rest frame velocity of the system by applying a shift of  $-\gamma$ . The differential subtraction method was then applied by shifting each spectra so that the host lines were at rest and then subtracting one from the other as described above.

It is necessary to have a consistent instrumental setup Ferluga et al. (1997), to avoid introducing extra instrumental effects (e.g. slit-width and/or filters) into the spectral differentials and to always observe the same wavelength range and maximize the information to be extracted. In our case, the second observation of HD 202206 and fourth of HD 30501 were taken with different filters compared to the other observations. Therefore, these two observations could not be used for this differential analysis. As noted in (Hadrava, 2009), any spectral differences in the filters would add extra unknown signal/noise making it harder to disentangle the faint spectral differences.

We performed the differential analysis for all targets but only show our most favourable case here, HD 30501, because it is the second largest companion in our sample at  $90 M_{\text{Jup}}$  and also has the second largest RV separation between observations. The differential spectra recovered for HD 30501 is shown at the bottom panel of Figure 4.1. The presence of deep ( $> 4\%$ ) stellar and telluric lines in the original spectrum is shaded by the blue and green regions respectively. This indicates that the features of the differential spectrum near these shaded regions are likely due to imperfect telluric correction and host mutual cancellation.

The mutual cancellation of the stellar host works well for the  $\sim 40\%$  deep line near 2117 nm, being completely removed, but it does not do so well for the smaller  $\sim 10\%$  deep line around 2121.5 nm. The residual for the large  $\sim 40\%$  deep telluric line near 2118.5 nm is quite prominent. There is also a wider residual due to three neighbouring lines  $\sim 10\%$  deep around 2120 nm which cause features in the differential spectrum. One possible explanation is that the continuum normalization near 2120 nm was influenced by this grouping of lines.

To understand the observed differential signal we simulated a differential spectrum of HD 30501 using a synthetic PHOENIX-ACES spectra with parameters  $T_{\text{eff}} = 2500 \text{ K}$ ,  $\log g = 5.0$ , and  $[\text{Fe}/\text{H}] = 0.0$ , with a RV offset estimated from the observation times. These parameters represent an estimated companion  $T_{\text{eff}}$  with the metallicity and  $\log g$  similar to the host (closest grid model). The model spectra were convolved to  $R = 50\,000$ , continuum normalized and scaled by the estimated flux ratio of the companion. We do not include any synthetic host or telluric spectra and as such simulate the differential result of a “perfect” host cancellation with no telluric contamination present. This is the ideal-case scenario, and we stress that it is impossible to simulate the effect of improper telluric correction in a meaningful way. When comparing the simulated and observed differential in the bottom panel of Figure 4.1, there is a striking amplitude difference. The orange-dashed line of the simulated differential spectrum amplitude is of a much smaller scale than the observed differential. This demonstrates that the amplitude of the differential signal we are trying to detect is much smaller than the residuals created by this differential technique.

The amplitude of the differential signal is lower than we expected due to the very low  $\Delta RV$  between the observation pairs. The maximum  $\Delta RV$  between observation pairs, for the observations investigated in this work, are provided in Table 4.4. **There is no  $\Delta RV$  for HD 4747 as there was only a single observation. We also provide the phase coverage for our targets. We calculate this as the ratio of time**

between the observed pairs and the orbital period, and show that the fraction of the orbit covered is very small, all except one covering less than 1 percent of the orbit.

In our best case, HD 30501, the  $\Delta RV$  of the companion between observations is  $1.41 \text{ km s}^{-1}$ . For comparison, a single Gaussian absorption line, to be shifted by  $\Delta\lambda = \text{FWHM}$  would need a  $\Delta RV$  of  $v_{\text{FWHM}} = c/R = \sim 6 \text{ km s}^{-1}$ . Since the  $\Delta RV$  are shifted by a smaller value than the FWHM, the spectral lines of the reconstruction mutually cancel themselves, diminishing the amplitude of the differential signal significantly. As the companion spectra are already faint (with a flux ratio at the percent level) the differential signal is not detectable within these observations and noise level.

When the  $\Delta RV$  of the companion is smaller than the FWHM of a line there is a mutual subtraction of the companion spectra, diminishing the detected amplitude of the differential signal, and removing the ability to detect the companions using this method. Observations need to be spaced further apart in time/phase to achieve a larger  $\Delta RV$  separation and increase the amplitude of the differential. Of course once there is a separation there will be complex interactions between neighbouring lines that need to be accounted for.

Since the amplitude is so small, and the we did not attempt to pursue this further.. We did not attempt the binary reconstruction from the combination...

Ferluga et al. (1997) present a reconstruction method to recover the secondary from the s-profile. Unfortunate this was not appropriate due to insufficient separation.

## 4.4 Orbital Solutions

The insufficient spacing becomes clear when the RV variation during the orbits are visualized. Figures 4.2–4.10 show the RV curves for each target analysed here. Stars with two companions are shown twice, with each companion treated as a single Keplerian (ignoring the presence of the other companion). For each panel on the left hand plot shows the RV variation across a full orbit of the companion, while the panel on the right shows the RV variation for the observation window of Period 89 only (6 months). The solid black line indicates the RV of the host star (with scale on the left hand axis), while the blue dashed line shows the RV of the companion (with the scale on the right hand axis). The orange crosses and red stars indicate the times at which observations were obtained for each target, for the host and companion respectively.

The first observation easily observed is that RV curves come in many different flavours(shapes). This variations in shape arise from the different orbital parameters of each target (provided in Table 4.2). In the left hand plots, in which a full cycle is shown the different shapes are created from the eccentricity,  $e$ , and argument of periapsis,  $\omega$ . In the right hand panels for which a fixed time period is shown the parameter affecting the image shown is the orbital period of the companion. Specifically the ratio of Period 89 to the orbital period determines what fraction (or multiples) of the orbit to display.

The RV curves of the star and the planet mirror each other about the systems mean velocity  $\gamma$ , with the amplitude scaled by their mass ratio (see Equation ?? advanced topics for q).

All the plots apart from HD 4747 have more than one observations indicated but this is difficult to tell as they are nearly all on top of each other.

For the companions HD 162020b (Figure ??) and HD 168443b (Figure 4.5) their orbital periods are shorted than 6 months, allowing for multiple cycles during Period 89. As such the full amplitude range was available to measure if observations were taken at the locations of the extrema and it should have

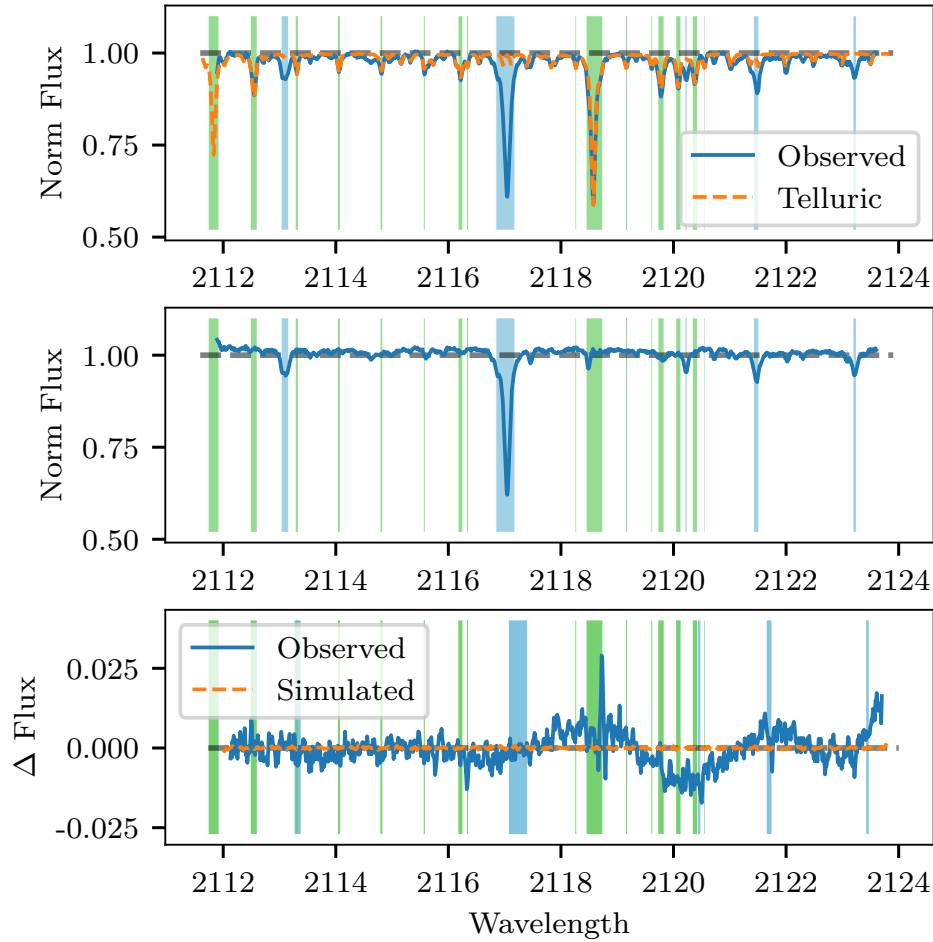


**Figure 4.1:** (Top) A reduced CRIRES observation of HD 30501 (blue) for detector 1 between 2112–2124 nm along with the tapas telluric absorption model (orange dashed) used for the wavelength calibration and telluric correction. (Middle) The telluric corrected spectra. (Bottom) (blue) Differential spectra for HD 30501 between observations 1 and 3. (orange dashed) Simulated “perfect” differential using PHOENIX-ACES spectra with parameters  $T_{\text{eff}} = 2500 \text{ K}$ ,  $\log g = 5.0$ , and  $[\text{Fe}/\text{H}] = 0.0$ , with the same  $\Delta RV$  as the observations. The shaded regions indicate where the telluric green and host star blue spectra are > 4% deep.

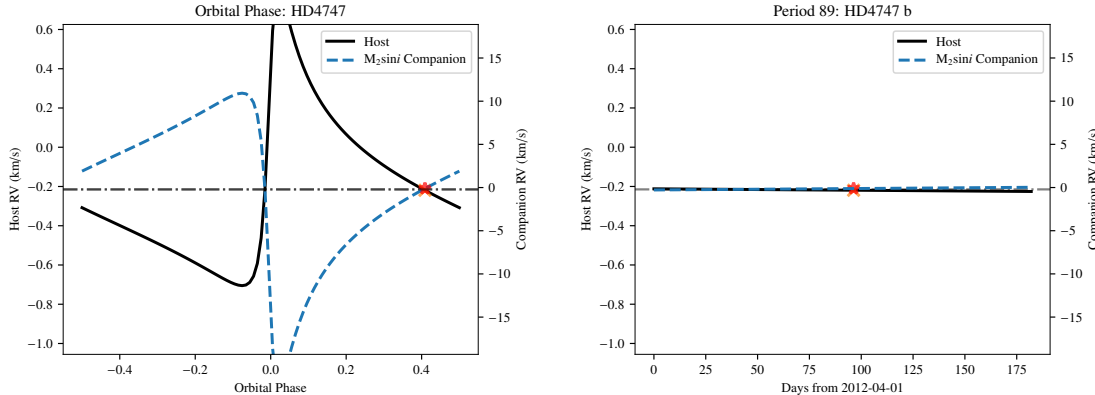


**Figure 4.2:** RV orbital single companion Keplerian for the HD 4747. The left hand plot shows the RV curve for one full orbit while the right hand panel shows the RV curve over 6 months (Period 89). The solid black line indicates the RV of the host star (with scale on the left), while the blue dashed line indicates the RV of the companion (with scale on the right). The orange crosses and red stars indicate the times at which observations were obtained for the target, for the host and companion respectively.

been possible to obtain observations in which the companion spectra were separated by more than their line FWHM. However the two observations for these two targets were taken immediately after each other. Making any differential extremely small. This is of course ignoring the fact that the flux ratios for these short period companions are estimated to be very low, meaning they would be very difficult to detect if sampled correctly.

The larger companion HD 168443c in Figure 4.6 the orbital period is longer, so they appear as straight lines in the right hand panel. Although the amplitude variation of the companion during Period 89 is about  $8\text{--}9 \text{ km s}^{-1}$ . Therefore observations taken at the extreme ends of Period 89 may have provided just enough separation to obtain a detection.

For HD 202206 about 3/4 of the orbit is covered in Period 89 with a RV amplitude of the companion possible of over  $40 \text{ km s}^{-1}$ . Therefore, in this case well separated RVs could have been obtained.

For the remain targets it is clear that sufficiently separated RVs were not obtained, but also that they were not possible from a single observing period with less than  $6 \text{ km s}^{-1}$  variation over Period 89. For HD 30501 in which there was a large time separation between observations was obtained, and is clearly visible in Figure 4.10. Unfortunately this did not result in a large enough companion separation. If the observations had been obtained in the previous period (88) instead then sufficient separation could have been obtained due to the orbital eccentricity. (this region is due to return in ...)

The code used to create orbital plots similar to those shown here is available under the iastro-pt/Observationtools<sup>4</sup> *Github* repository with documentation available on <https://ia-observationtools.readthedocs.io/en/latest/>

The sampling of points in the orbit reveal that the choice of points was not favourable for the application of the direct subtraction technique. This was however only discovered after attempting to apply the technique.

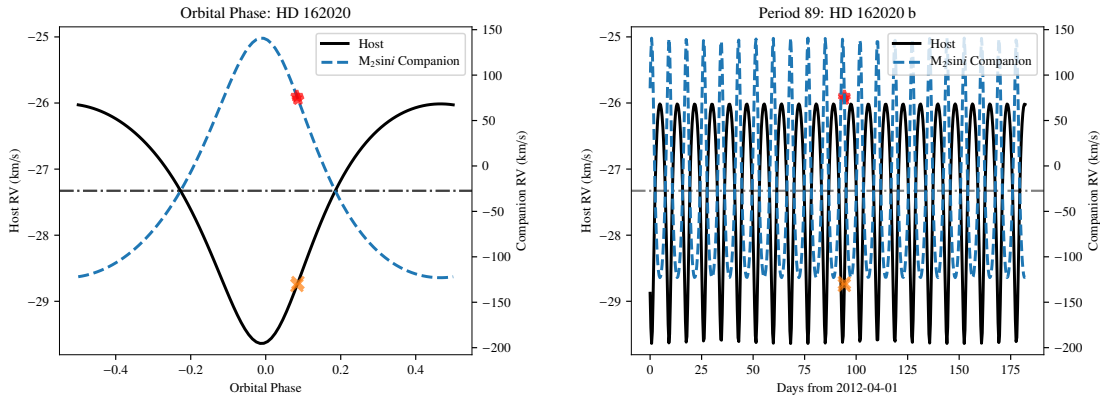
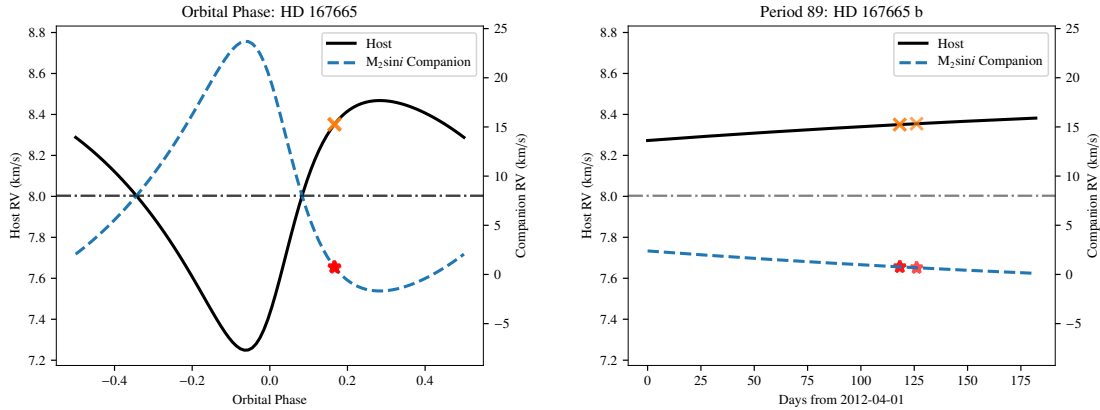
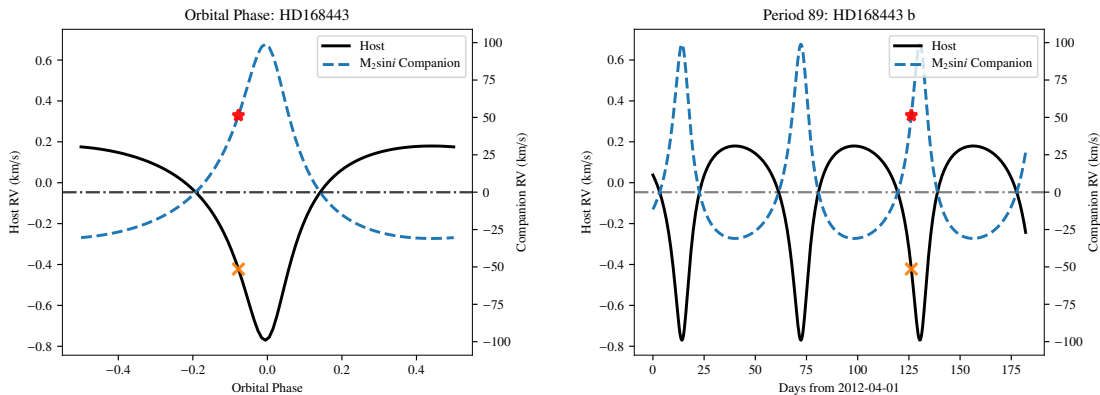
<sup>4</sup> <https://github.com/iastro-pt/ObservationTools>

Should I predict when the best time to observe these targets are is?  
e.g. in 2020 x and x will have sufficient RV change in one period to achieve a detection.

change RV scale for hd4747 orbit

Fix plot titles

Check M2sin i labels - can we get M2 only for those that we know

**Figure 4.3:** Same as Figure 4.2 but for HD 162020.**Figure 4.4:** Same as Figure 4.2 but for HD 167665.**Figure 4.5:** Same as Figure 4.2 but for HD 168443b. Analysed as if this was a single companion.

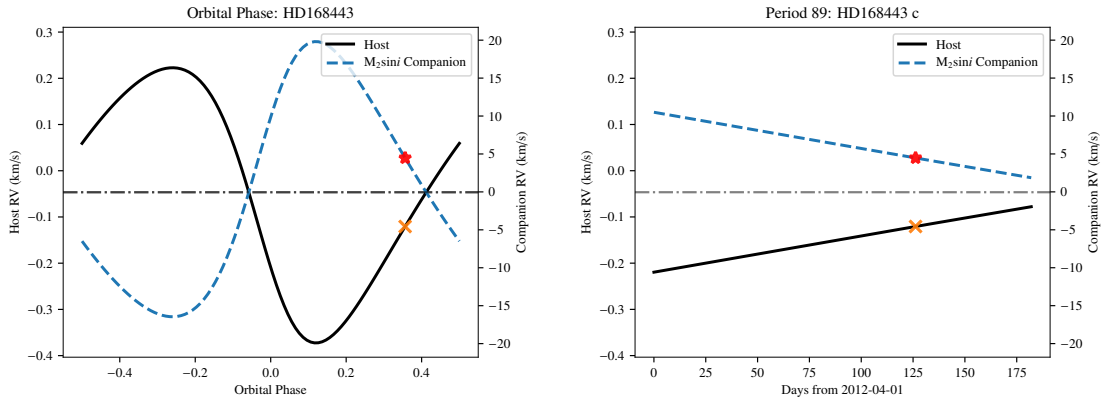


**Figure 4.6:** Same as Figure 4.2 but for HD 168443c. Analysed as if this was a single companion.

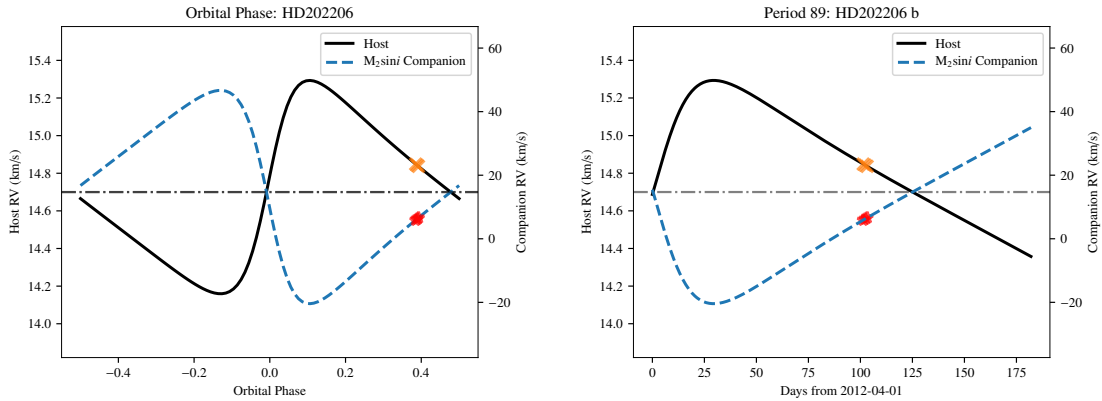


**Figure 4.7:** Same as Figure 4.2 but for HD 202206B. Analysed as if this was a single companion.

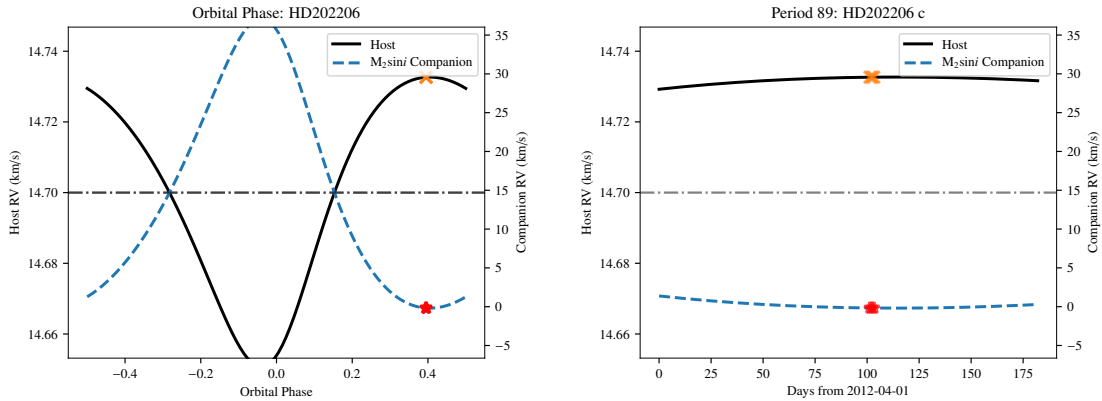


**Figure 4.8:** Same as Figure 4.2 but for HD 202206c. Analysed as if this was a single companion.

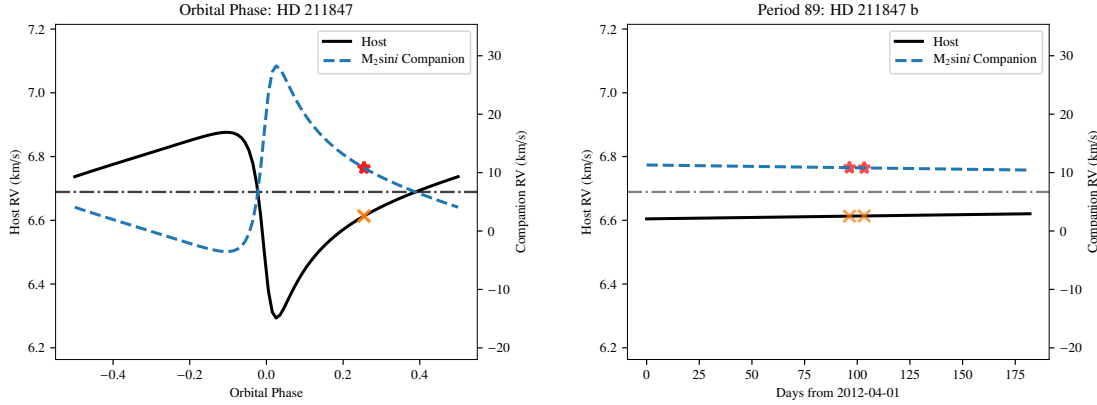


**Figure 4.9:** Same as Figure 4.2 but for HD 211847.

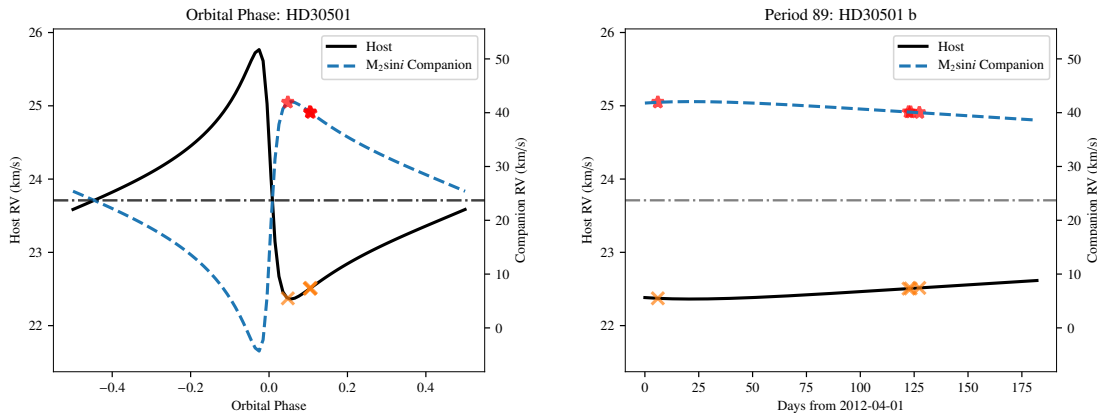


**Figure 4.10:** Same as Figure 4.2 but for HD 30501.

Should RV of companion be scaled by  $m_2 \sin i$  only or  $m_2^2$  if known?

#### 4.4.1 Relative differential amplitude

To investigate the differential subtraction under tiny  $\Delta RV$  further the change in differential amplitude against variation in RV was explored. Simulations were performed creating a differential spectra for a range of  $\Delta RV$ s between  $\pm 10 \text{ km s}^{-1}$  using the same PHOENIX-ACES spectra for the companion of HD 30501 ( $T_{\text{eff}} = 2500 \text{ K}$ ,  $\log g = 5.0$ ,  $[\text{Fe}/\text{H}] = 0.0$ ) convolved to  $R = 50000$ . These simulations were focused between the wavelength range 2110–2123 nm, corresponding detector 1 of the CRIRES observations. The differential spectra was created for each by taking the synthetic spectrum for the companion, Doppler shifting a copy the spectrum and subtracting it from the original. At each RV step the maximum absolute differential amplitude (peak to peak) of the simulated differential spectrum observed was recorded. Again these simulations are performed assuming perfect telluric correction and removal of the host star by only considering the spectrum of the companion alone.

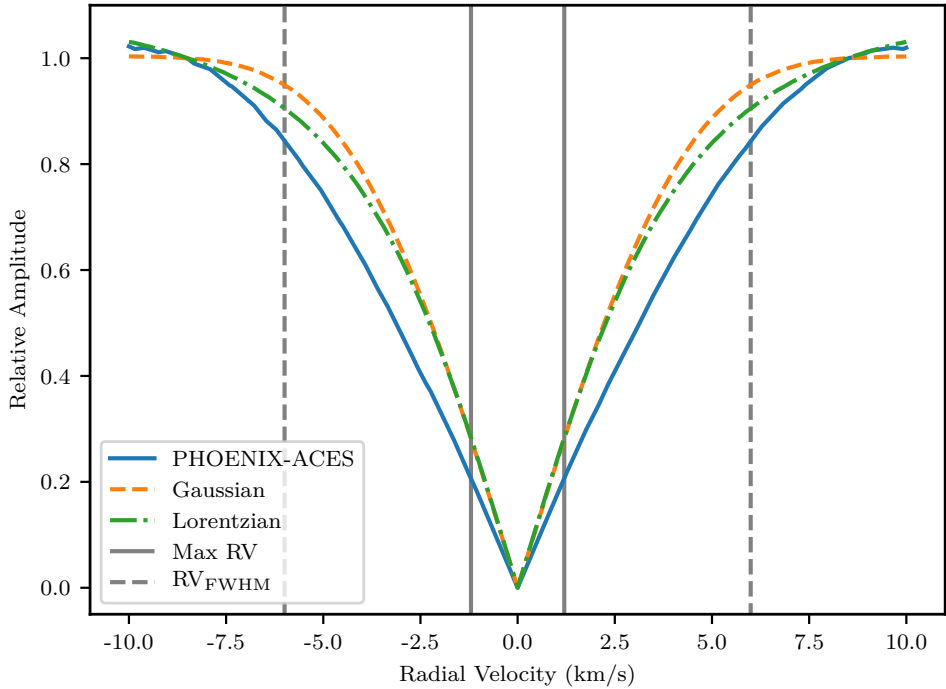
The result of this simulation is given in Figure 4.11. As this absolute amplitude is specific to the lines present in the analysed wavelength range, the values were normalized by the median amplitude value outside of the line FWHM (dashed vertical lines), between  $\pm(7 - 10) \text{ km s}^{-1}$ , to give a relative differential amplitude, independent from the depth of a specific line. Differential subtraction simulations we also performed using a spectrum made up of a single Gaussian line and a single Lorentzian, these are shown in Figure 4.11 as the orange dashed and green dash-dotted lines respectively. The spectral profile shape of differential for the Gaussian line was also checked for consistency with the analytical form of the differential spectra Ferluga et al. (1997, Equation A.1) (included above as Equation 4.6).

Figure 4.11 that a  $\Delta RV$  of zero between companion spectra, the spectral lines of the companion completely cancel each other out, resulting in zero amplitude. As the RV separation increases in either direction, the individual lines begin separating, and stop cancelling themselves out. A maximum differential amplitude is achieved when the individual lines are fully separated. We did not consider the shape/width of the differential spectral lobes as done in Ferluga et al. (1997, eqn. A.1), but this could also have been measured.

In the simulations of the synthetic spectrum (and of course real spectra) neighbouring spectral lines begin to strongly interfere, leading to a variable measured relative amplitude beyond 10 km/s. The shape of the relative amplitude becomes complicated due to the interaction but since the  $\Delta RV$  for all the observations fall well short of this region it was not investigated further. It is suspected that the interaction of neighbouring lines is one possible cause for the difference in the relative differential amplitude between the single theoretical line profiles and synthetic spectrum between 2 and 6  $\text{km s}^{-1}$ .

The vertical dotted lines indicate the line FWHM =  $\lambda/R = v/\text{cvelocity}$  of  $6 \text{ km s}^{-1}$  at  $2 \mu\text{m}$  with  $R=50000$ , showing that the amplitude is almost maximum when the lines are separated beyond their line width. The two solid vertical lines in Figure 4.11 indicate the  $\Delta RV = 1.41 \text{ km s}^{-1}$  separation calculated for our best target, HD 30501 from Table 4.4, given known orbital parameters and the observation times. This shows that our differentials have severely reduced amplitude, < 20% relative to well separated individual lines. As the companion spectra are already faint and in combination with a host star at >1% flux ratio the >80% extra reduction in signal amplitude makes this detection impossible with these observations.

Increase size of diff amp plots to two



**Figure 4.11:** Simulated relative amplitude of differential spectra at different companion  $\Delta RV$  separations revealing the diminished amplitude at very small orbital separations. The solid blue line shows the maximum relative amplitude of the differential signal (from a shifted copy of itself) of a PHOENIX-ACES spectrum with  $T_{\text{eff}} = 2500 \text{ K}$ ,  $\log g = 5.0$ ,  $[\text{Fe}/\text{H}] = 0.0$  in the wavelength region  $2110\text{--}2123 \text{ nm}$ . The maximum difference is normalized by the median amplitude between  $\pm 7\text{--}10 \text{ km s}^{-1}$ , representing a complete line separation. The orange (dashed) and green (dot-dashed) lines represent the relative amplitude of a differential spectrum of a spectrum containing a single Gaussian and single Lorentzian absorption line respectively, each with a unitary amplitude and a  $\text{FWHM} = \lambda/R$ . The solid vertical lines indicate the estimated companion  $\Delta RV$  in these observations while the dashed vertical lines indicate the RV corresponding to the FWHM at this wavelength and resolution. .

#### 4.4.1.1 Differential scheduling challenges copy from paper

This work has revealed that more care needs to be taken in planning the observations for the spectral differential analysis of faint companions in the future. Paying attention in particular to the FWHM of the lines in the region (governed by resolution and wavelength); the estimated companion  $\Delta RV$ ; the previous observations from different observing periods; and keeping consistent detector settings.

The original goal for the observations was to obtain two different and “clearly separated radial-velocities” for the secondary companion. However, the program was assigned a low-priority (C, in ESO grading) and, possibly due to operational reasons, the original time requirements necessary to secure well separated RVs for the companion spectra could not be met. This meant that all observations were insufficiently separated to extract a differential spectra for the companion.

The long orbital periods of these targets is also a contributing factor to the insufficient separations. Most of the targets observed here have orbital periods much longer than an observing semester (183 days). An optimal pair of observations (achieved at the extrema) would need to have been obtained from separate observing periods (between 2 months and 19 years apart). In some cases, even observations taken at the beginning and end of a single observing semester would not be sufficient to achieve companion separation (depending on the phase). Requiring separate observing periods to even achieve the minimum  $\Delta RV$  larger than the line FWHM. At the time it was impossible to ask for time over several semesters in a regular proposal.

Our study demonstrates the importance of proposals for projects that need to be extended over several semesters or years. In the ESO context, this corresponds to “Monitoring proposals” (e.g., ESO, 2017, pg. 18). Observations of the targets explored here, with long orbital periods in particular, would benefit from the ability for multi-period proposals and newer scheduling systems which allow for tighter scheduling constraints, such as a companion RV separation.

For future observations we suggest that the known orbital solution of the companion be used to estimate the companions’ RV curve during the observing period, with the companion  $M_2 \sin i$  providing an RV upper-limit. Knowing the instrumental wavelength and resolution, a constraint can then be set to avoid taking observations when the companion spectra are insufficiently separated, or  $\Delta RV < \text{FWHM}$ . This constraint can be set using the absolute and relative *time-link* constraints available in ESO’s Phase 2 Proposal Preparation (P2PP) tool. Additionally, analysing the known orbital solution before-hand, to determine RV constraints will also help identify the best time to observe, if observations from separate periods will be required or, if an optimally separated companion differential is even feasible.

It was unable to be determined if the time differential was asked for in the 2nd proposal round....

**CHECK out LOCKWOOD 2014 - maximum likelihood with todcor 1e-4 flux ratio double lined spectra**

## 4.5 Direct recovery in the mIR

It was investigated if this differential technique could be extended into the mid-infrared mIR domain. There were two reasons for this, to develop experience with the mIR domain where the contrast ratios are higher and due to the lack of high-resolution nIR spectrographs available at the time, as CRIRES was being upgraded to CRIRES+.

VISIR is a mIR spectrograph on the VLT, offering diffraction-limited imaging at high sensitivity in three mid-infrared (MIR) atmospheric windows: the *M*-band at  $5\text{ }\mu\text{m}$ , the *N*-band between  $8\text{--}13\text{ }\mu\text{m}$  and

the  $Q$ -band between  $17 - 20 \mu\text{m}$ , respectively. We explored the use of VISIR to detect the spectra of Brown Dwarf companions in the mIR. The candidate selected as the best target to investigate was HD 219828 which has a hot-Neptune ( $M_2 \sin i = 0.066 M_{\text{Jup}}$ ) (?) and a recently discovered super Jupiter ( $M_2 \sin i = 15.1 M_{\text{Jup}}$ ) on a long period (13 yr) eccentric orbit ( $e = 0.81$ ) (?).

Based on the spectra of a cool brown dwarfs in the mIR, and the detector configuration available at the time the chosen detector settings were the low resolution mode covering the wavelength region  $8 - 13 \mu\text{m}$ . This wavelength region would have encompassed the  $\text{NH}_4$  signature at  $10.5 \mu\text{m}$  and the edge of a  $\text{CH}_4$  band at  $7.7 \mu\text{m}$ , both large features in the BD mIR spectrum.

After performing flux ratio calculations between the host and companion using the ? models and considering the performance of the VISIR instrument and the exposure time calculator it was determined that observations with VISIR to achieve a SNR of 100 were infeasible, requiring 1 000's of hours observing time to achieve the necessary signal-to-noise level to separate the companion from a blended spectra. As such the direct separation approach was not continued further in the mIR.

...

This method is very similar to Kostogryz et al. (2013) except that they focus on M-dwarfs host stars with the observations taken at the extrema, in which the companion lines are well separated.

They get a result???

## 4.6 Summary

This Chapter presented the observations that were gathered having in mind the application of a differential subtraction method (e.g., Ferluga et al., 1997; Kostogryz et al., 2013) to recover the spectra of the faint BD companions. Due to the poorly separated observation times relative to the long orbital periods, the differential subtraction method presented in Section 4.3 was revealed to be inappropriate for these observations as the RV separation of the companion spectra between observations is significantly smaller than the width of individual spectral lines. The small separation of the companion causes the lines of the companion to also mutually cancel, severely reducing the residual signal to well below the available noise level. The requirement of well separated RVs for the companion spectra was clearly stated in the original proposal but was not satisfied by the observations. **The very large orbital periods of some of the targets would not produce a sufficient RV signal during one semester. This was a possible oversight during the proposal stage.** The largest estimated companion  $\Delta RV$  separation between the observations of each target is provided in the 7th column of Table 4.4. **Radial velocity constraints are also valid for** other studies such as the detection of reflected light from exoplanets Martins et al. (2015).

move

# Chapter 5

## Spectral Companion Recovery

Because the differential subtraction technique was unsuccessful, not being separable in time. A second method was attempted to try and extract something useful out of the spectra.

We develop this new method, preform some tests and then show the results obtained. There were numerous issues encountered and unsuccessful results.

Contrast our result to other works. More phases, longer integration time, higher SNR.

### 5.1 Main Section 1

Model fitting two components.

### 5.2 Binary synthetic spectral recovery

Since the differential method is ineffective for our dataset due to the RV separation between observations, we explored a second approach to detect the presence of the faint companion spectra. This second approach compares the observed spectra to combinations of synthetic spectral models using  $\chi^2$  methods which have been extensively used in the literature (e.g., Astudillo-Defru et al., 2015; Passegger et al., 2016; Zechmeister et al., 2018; Nemravová et al., 2016). **The temperature of synthetic spectra fitted to the companion will provide some indication of the companions spectral type, but will not produce a direct mass constraint that was the original aim of this work.**

#### 5.2.1 Synthetic PHOENIX-ACES models

We use the PHOENIX-ACES (Husser et al., 2013) synthetic spectra library as our reference for the spectral comparison. It uses the most recent version (16) of the PHOENIX code and is suitable for the spectra of cool stars. The full parameter grid space of the PHOENIX-ACES spectra is given in Table 5.1 although we only explore models constrained by the targets explored here.

The spectral model libraries were accessed using the useful “grid tools” interface provided in the *Starfish*<sup>1</sup> Python package (Czekala et al., 2015), which made it efficient to load in the spectra when needed.

<sup>1</sup> <https://github.com/iancze/Starfish>

**Table 5.1:** Full parameter space of the PHOENIX-ACES spectral grid.

	Range	Step size
$T_{\text{eff}}$ [K]	2 300 – 7 000	100
	7 000 – 12,000	200
logg	0.0 – +6.0	0.5
[Fe/H]	-4.0 – -2.0	1.0
	-2.0 – +1.0	0.5
$\alpha/\text{Fe}$	-0.2 – +1.2	0.2

We multiply the synthetic spectra by the wavelength to convert it into photon counts, ignoring multiplicative constants, as done in Figueira et al. (2016)<sup>2</sup>. The spectra were convolved with a Gaussian kernel to match the resolution of the observations ( $R = 50\,000$ ). Due to the distributive property of convolution it is efficient to apply it once to each spectra first, before the spectral pairs are combined.

The PHOENIX-ACES models include dust in equilibrium with the gas phase while ignoring dust opacity and does not include any mixing/settling which is important for cooler BD atmospheres. They set a minimum library  $T_{\text{eff}} = 2\,300\,\text{K}$  to avoid the temperatures at which the modelling of clouds is necessary. This unfortunately limits the use of this library for this technique to the largest mass companions in our sample. For example a  $T_{\text{eff}} = 2\,300\,\text{K}$  corresponds to a BD with  $M \sim 84M_{\text{Jup}}$  at 5 Gyr from the Baraffe et al. (2003) evolutionary models.

There are other models that extend below 2 300 K such as the BT-Settl models (Allard, 2013; Baraffe et al., 2015). These are discussed in Section ??.

### 5.2.2 $\chi^2$ method

The well known  $\chi^2$  technique measures the weighted sum of the squared deviation between the observation ( $O_i$ ) and the computed models ( $C_i$ ), with the minimum  $\chi^2$  value representing the best-fit parameters.

$$\chi^2 = \sum_i (O_i - C_i)^2 / \sigma_i,$$

where  $\sigma_i$  is the error on each measurement. We estimate the  $\sigma$  of each spectrum using the  $\beta\sigma$  method (Czesla et al., 2018), using the MAD (median absolute deviation about the median) robust estimator. This method estimates the spectral noise using numerical derivatives of the spectra. We followed the procedure outlined in Czesla et al. (2018), analyzing the results from successive parameter combinations to settle on an order of approximation (derivative level) of 5, and a jump parameter (pixels skipped to avoid correlations) of 2. We apply the same  $\sigma$  value to all points  $\sigma_i = \sigma$ . The  $\beta\sigma$  method provided  $\sigma$  estimates for the target spectra which correspond inversely to signal-to-noise ratios between 100–500, similar to the values given in Table 4.3 calculated from the continuum of detector 2.

The computed models are described in Section 5.2.3 and result in a multidimensional grid of  $\chi^2$  values for each combination of parameters, namely the spectral temperature, host RV, and companion RV for each detector, observation and target.

We obtain the global minimum of the multidimensional  $\chi^2$ -space to represent the best fit to the observed spectra. We sum the multidimensional  $\chi^2$  across multiple detectors and determine a global minimum  $\chi^2$  for the whole observation  $\chi^2_{\text{obs}} = \sum_{n=1}^N \chi_n^2$ , where  $N$  is the number of detectors used. We

<sup>2</sup> Synthetic models provide the spectral energy distribution ( $\text{erg s}^{-1} \text{cm}^2 \text{cm}^{-1}$ ).

do not, however, combine the  $\chi^2$  values across the separate observations as the RV parameters of the host and companion will vary between each observation. However, since the current observations are insufficiently separated, it may be possible to combine the separate observations; but in general this would not be the case, so was not performed.

The inverse survival function of the  $\chi^2$  distribution is used to determine the confidence levels on the minimum  $\chi^2$  parameters. The inverse survival function returns a  $\Delta\chi^2$  value from the minimum  $\chi^2$  value for a given sigma level and degree of freedom<sup>3</sup>. For example, the  $\Delta\chi^2$  for a single degree of freedom required for the 1-, 2-, and 3- $\sigma$  levels is 1, 4, and 9 respectively (Bevington and Robinson, 2003). This method assumes that the measured flux is observed with a SNR sufficiently high so that the noise on the spectrum is approximately Gaussian, and the  $\chi^2$  method appropriate.

For a given observation, the  $\chi^2_{red}$  is computed by  $\chi^2_{red} = \chi^2/\nu$  where  $\nu = n - m$ , the number of observed pixels,  $n$ , minus the number of parameters of interest,  $m$ <sup>4</sup>, and is performed after the summation over the detectors.

### 5.2.3 Computed model spectra

In this section we detail how we transform the synthetic PHOENIX-ACES spectra into the computed models ( $C_i$ ) to fit to the observations. The spectra have already been converted to the correct unit and resolution.

These synthetic spectra are used individually for the single component model and combined together into a binary model. The results of these models are interpolated to the wavelength grid of the observed spectra and the  $\chi^2$  calculated by comparing the model and observation at each point.

#### 5.2.3.1 Single component model

The single model  $C_i^1$  comprises of a single synthetic spectrum,  $J$ , (with model parameters  $T_{\text{eff}}$ , logg, [Fe/H], [ $\alpha$ /Fe]) and is Doppler shifted by a RV value  $rv_1$ .

$$C_i^1(\lambda) = J(\lambda_0(1 - \frac{rv_1}{c})) \quad (5.1)$$

where  $\lambda$  is the shifted wavelength,  $\lambda_0$ , the model rest wavelength and,  $c$ , the speed of light in a vacuum. The model's flux is then continuum normalized to unity to match the observed spectra, and interpolated to the wavelength grid of the observation.

This single component model analysis is similar to the Passegger et al. (2016)  $\chi^2$  fitting. We apply the same re-normalization (see Section 5.2.4) to account for slight differences in the continuum level and possible linear trends between the normalized observation and model. We do not, however, apply any dynamical masking to sensitive lines to make the the  $\chi^2$  minima more distinct or linearly interpolate the stellar parameters between the grid models to obtain high precision stellar parameters. This is because we are not trying to derive precise stellar parameters but to detect the spectra of the companions. We instead include radial velocity components to the  $\chi^2$  fitting, which is not included in Passegger et al. (2016).

<sup>3</sup> In *Python* with the *scipy* package this is a single line `scipy.stats.chi2(dof).sf(1-p)`, where  $p = 0.68$  for 1- $\sigma$ , and  $dof$  is the degree of freedom.

<sup>4</sup>  $m = 2$  or  $4$  in the examples explored below

### 5.2.3.2 Binary model

In the binary situation we consider the superposition of two synthetic spectral components, one each for the host and companion respectively. Both spectra are Doppler shifted by  $rv_1$  which represents the RV motion of the host star, while the companion spectra is also Doppler shifted by a second RV,  $rv_2$ , representing the RV offset between the host and companion. This choice is arbitrary, but in this way the mean motion of the system relative to Earth is captured only in  $rv_1$ . The two spectra are scaled by their squared radius (see Section 5.2.3.3) then added together, thus fixing the relative amplitude of the two components. Given two spectral components  $J_1$  and  $J_2$  with radii  $R_1, R_2$  this equates to

$$\begin{aligned} C_i^2(\lambda) = & J_1\left(\lambda_0\left(1 - \frac{rv_1}{c}\right)\right) \times R_1^2 + \\ & J_2\left(\lambda_0\left(1 - \frac{rv_1}{c}\right)\left(1 - \frac{rv_2}{c}\right)\right) \times R_2^2 \end{aligned} \quad (5.2)$$

The combined spectra is continuum normalized by dividing by an exponential fitted to the continuum of the combined spectrum, as we assume we are in the Rayleigh-Jeans regime. This assumption here is wavelength dependent and other appropriate continuum normalization techniques are also valid. In the case of a BD companion around an FGK star investigated here, the continuum is dominated by the contribution from the host star as it contributes the majority of the spectrum with flux ratios around 2 110–2 160 nm below  $\sim 1\%$ .

We combine the models in this way to represent the correct absolute flux ratio of the components. The median flux ratio between the two components is calculated for the wavelength range used here as an indication of the flux ratio level.

The binary model should provide meaningful information about the companion parameters (e.g.  $T_{\text{eff}}$ ) and a estimate of the flux ratio of the system. These can be combined with the Baraffe et al. (2003) models to constrain the mass of the companion. However, we need to be careful with this model as the inclusion of extra spectral components and associated parameters could also provide a better fit to observations which do not have a companion, by fitting components of the noise.

The full list of grid parameters for the binary model are  $T_{\text{eff}1}$ ,  $\log g_1$ ,  $[\text{Fe}/\text{H}]_1$ ,  $[\alpha/\text{Fe}]_1$ ,  $rv_1$ ,  $T_{\text{eff}2}$ ,  $\log g_2$ ,  $[\text{Fe}/\text{H}]_2$ ,  $[\alpha/\text{Fe}]_2$ ,  $rv_2$  where the subscripts 1 and 2 indicate the host and companion models respectively.

### 5.2.3.3 Effective radius

To combine the two synthetic spectra with the correct observed flux ratio we need to integrate the emitted flux over the effective surface area of each emitting body respectively. Ignoring the common multiplicative constants that will disappear with normalization, we scale the two synthetic spectra individually by the square of their respective radii,  $R_1$  and  $R_2$ .

In this work we use the effective radius (PHXREFF keyword) of each component from the PHOENIX model headers. This is the radius used in modelling of the stellar atmospheres. We use this radii as it is directly tied to each model spectrum, and already available. The ratio of the radii from the two synthetic spectra in the binary models are provided in Table 5.2.

We are aware that using these radii has its limitations, since as stated previously, there is a degeneracy in BD mass, age, and luminosity of the companion, and in particular a combination of radius-mass and radius-age relationships (Sorahana et al., 2013). Using the PHOENIX-ACES model

effective radius does not allow for any independent age constraints to be incorporated, or allow for any variability in the radii to account for uncertainties.

The targets analysed here do not have transits, but if the radius ratio can be independently determined from the photometric transit method (Deeg, 1998) then this could be used to constrain the radius ratio used when combining the binary model spectra instead.

### 5.2.4 Re-normalization

Slight trends in the continuum level between the observed spectra and computed models were removed using the re-normalization following (Passegger et al., 2016):

$$F_{re-norm}^{obs} = F^{obs} \cdot \frac{\text{continuum fit}_{model}}{\text{continuum fit}_{observations}}. \quad (5.3)$$

The polynomial continuum fits to the normalized observations and models are used to re-normalize the observed spectrum to the continuum of the models. For detectors 1–3 a polynomial of first degree was used, while for detector 4 a quadratic is needed to fit the edge of a strong Hydrogen line (Brackett- $\gamma$ ) at 2166 nm, which lies just off of detector 4. This broad line is only observed in the synthetic spectra and not in the reduced observations. It is assumed that this was normalized out during the reduction process.

For each model we further allow the continuum level to be varied by  $\pm 0.05$  as a free parameter taking the model with the smallest  $\chi^2$  value.

### 5.2.5 Reducing parameters

The high dimensionality of the binary model makes it computationally challenging and difficult to analyse the  $\chi^2$  space. For reference, the multiplicative parameter space is squared when increasing from one spectral component in the single model to a binary model, and therefore becomes computationally expensive. In general the number of possible parameter combinations for  $c$  spectral components each with a grid of  $m$  models increases to  $c^m$ . If the full set of PHOENIX-ACES library spectra (66456) is explored with a binary fit then this naively balloons to over 4.4 billion possible combinations. Half of these are not unique as the host and companion components are swapped. This is the worst case scenario and we implement a number of assumptions to vastly reduce the parameter-space enabling faster computation.

Our first assumption is to restrict ourselves to models with an Alpha element abundance ( $[\alpha/\text{Fe}]$ ) of zero. This is likely a very good approximation as all our targets have solar metallicity and are thus very likely to belong to the thin disk of the Galaxy, where  $[\alpha/\text{Fe}]$  values are close to zero (i.e., solar) – e.g. Adibekyan et al. (2012). Our second is to assume that we can significantly reduce the search space with literature values for the host star. We fix the metallicity of both components to the closest grid to the literature value (usually  $[\text{Fe}/\text{H}] = 0.00$ ). We also fix the logg of the host star to its literature values given in Table 4.1. The uncertainties on the literature measurements for logg ( $\sim 0.1$ ) and metallicity ( $\sim 0.05$ ) are both smaller than the grid steps of 0.5 for these parameters. For the logg of the companion we use the Baraffe et al. (2003, 2015) evolutionary model value for the given companions  $M_2/M_2 \sin i$  and hosts age.

We use the estimated companion temperatures from the Baraffe evolutionary models given the companion  $M_2$  or  $M_2 \sin i$  and stellar age as a starting point for the companion spectra grid computation and extend the grid in each direction, within the model limits. For example we show the companion

**Table 5.2:** Input and recovered parameters on simulations and an observation when applying a single ( $C^1$ ) and binary ( $C^2$ ) models. The logg and metallicity were fixed at  $\log g_1 = 4.50$ ,  $\log g_2 = 5.0$  and  $[\text{Fe}/\text{H}] = 0.0$  equally for both components. Gaussian noise was added to both simulations with a SNR of 150. Here  $m$  and  $n$  are the number of data points and parameters used in each model.

	Simulation 1			Simulation 2			Observed HD 211847		
	Input	Recovered		Input	Recovered		Expected	Recovered	
		$C^1$	$C^2$		$C^1$	$C^2$		$C^1$	$C^2$
$T_{\text{eff}1}$	5 800	5 800	5 800	5 700	5 800	5 700	$5 715 \pm 24$	5 900	5 800
$T_{\text{eff}2}$	4 000	–	3 800	3 200	–	3 100	$\sim 3 200$	–	$> 3 800^{\text{a}}$
$rv_1$	0	0.1	0	6.6	6.6	6.6	$6.6 \pm 0.3$	7	7.6
$rv_2$	10	–	9.8	0.5	–	-1	$0.5 \pm 2$	–	-12.6
$R_1/R_2$	2.57	–	2.71	3.16	–	3.27	3.16	–	$< 2.71^{\text{a}}$
$F_2/F_1$	0.084	–	0.066	0.030	–	0.026	0.030	–	$> 0.066^{\text{a}}$
$m$	–	3 072	3 072	–	3 072	3 072	–	2 612	2 612
$n$	–	2	4	–	2	4	–	2	4
$\chi^2$	–	4 978	3 792	–	3 746	3 630	–	37 688	33 860
$\chi^2_{\text{red}}$	–	1.62	1.24	–	1.22	1.18	–	21.3	19.2
BIC	–	-20 145	-22 315	–	-21 477	-21 377	–	18 281	14 468

<sup>a</sup> At the arbitrary upper limit for companion temperature grid (3 800 K).

temperature grid spanning  $-600$  to  $+400$  K in Figure 5.1 and  $\pm 400$  K in Figs. 5.2 and 5.3.

The large numbers stated above also do not include the RV grid for each component. The RV grid is user defined and the number of spectra /models to consider increases when the RV grid step size is decreased (finer RV resolution). We can reduce the RV grid space significantly by tailoring it to the target being examined. For each target, we use the estimated RV values from the observation time and orbital parameters, given in Table 4.3 as a centre starting point for the  $rv_1$  and  $rv_2$  values and increment the RV within a few FWHM around those values, or out to the targets  $K_1$  and estimated  $K_2$  values.

An iterative process could be implemented to refine the RV grids, starting at a larger grid with lower RV resolution then performing a higher resolution grid about the minimum  $\chi^2$  RV values. This was only done manually but could have been automated. One could expect that a good starting RV grid step be governed by the spectral resolution, e.g. comparable to the FWHM velocity.

For the companions targets with fully resolved orbits the known RV of the host star,  $rv_1$  could also have been fixed. We however left this free to see if the known value would be recovered by the fitting.

### 5.3 Results

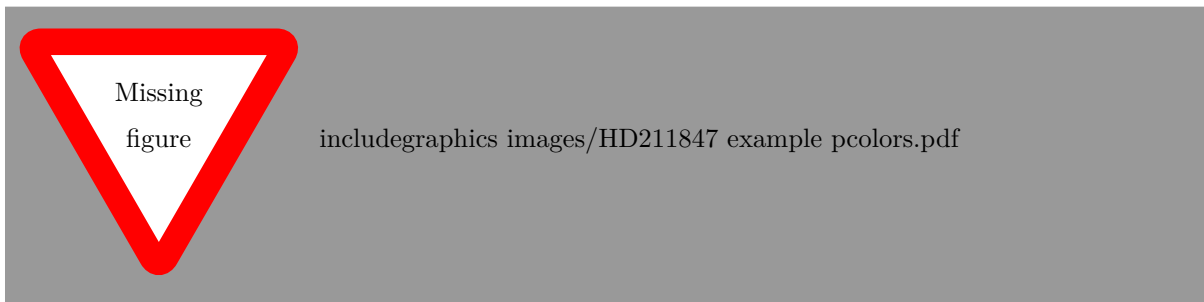


**Figure 5.1:**  $\chi^2$  results for companion recovery of a simulated binary observation of a Sun-like star ( $T_{\text{eff}1} = 5800$  K) with an M-dwarf companion ( $T_{\text{eff}2} = 4000$  K). The top right plot shows the application of a single component model ( $C^1$ ) while the other three are using a binary model ( $C^2$ ). Both left hand panels show the distribution of host temperature and host RV. The top right panel shows the distribution for host and companion temperature, and the bottom right the companion temperature and radial velocity. The red circle and yellow star indicate the location of the simulation input and recovered parameters respectively. The white line shows a  $3-\sigma$  confidence level about the minimum  $\chi^2$  solution grid point. Each box is centred on the parameter values and shows the grid resolution.

**Figure 5.2:** Similar to Figure 5.1,  $\chi^2$  results for companion recovery of a simulated binary observation similar to HD 211847, ( $T_{\text{eff}1} = 5800$  K,  $T_{\text{eff}2} = 3200$  K). The top right plot shows the application of a single component model ( $C^1$ ) while the other three are using a binary model ( $C^2$ ). Both left hand panels show the distribution of host temperature and host RV. The top right panel shows the distribution for host and companion temperature, and the bottom right the companion temperature and radial velocity. The red circle and yellow star indicate the location of the simulation input and recovered parameters respectively. The white line shows a  $3-\sigma$  confidence level about the minimum  $\chi^2$  solution grid point. Each box is centred on the parameter values and shows the grid resolution.



Here we show the results from applying the companion recovery model to simulated observations and to an observation.

### 5.3.1 Simulated binaries

To test the companion recovery method we create simulated binary observations using PHOENIX-ACES spectra. White noise was added with a standard deviation  $\sigma = 1/\text{SNR}$ , for a given signal-to-noise (SNR) level. We then applied the grid-matching recovery technique detailed above and compared the resulting parameters to the inputs.

The results of two example binary simulations are displayed in Figs. 5.1 and 5.2, both simulated with a SNR of 150. The input and recovered parameters for the binary components are indicated by the red circles and yellow stars respectively, and are given in Table 5.2. The  $3-\sigma$  contour is shown in white on the plots to indicate the shape of the confidence level only. The  $1-\sigma$  contours are not shown here as they are much smaller than the temperature grid step and are not easy to visualize at this scale as they are often smaller than the marker shown at the minimum location. Each coloured rectangle is centred on the grid point, with its shape indicating the resolution of the grid space searched.

The first simulation shown in Figure 5.1 is for a Sun-like star with a M-dwarf companion, with a  $T_{\text{eff}2} = 4000$  K. The top-left panel shows the recovered host parameters when the single model is applied

to the simulated binary. The top-right and both bottom panels are the parameters recovered when using the binary model. Both left-hand panels display the parameters for the host component to easily compare between models. With both models the host temperature  $T_{\text{eff}1}$  is correctly recovered. The host RV,  $rv_1$ , is  $0.1 \text{ km s}^{-1}$  (two grid spaces) different from the simulated value for the single component model and is correctly recovered with the binary model.

The minimum  $\chi^2$  location for the companion temperature is 200 K below the simulated value, and the RV of the companion recovered is  $0.2 \text{ km s}^{-1}$  below the input value. The input values for the companion are just outside of the  $3\sigma$  contours shown. The flux ratio for the input is 0.08 while the flux ratio recovered is 0.066.

The second simulation shown in Figure 5.2 is performed with parameters to mimic the observation of our target with highest flux ratio, HD 211847. In this simulation the single component model recovers a host with the correct RV but a temperature 100 K higher than the input value. Again, adding the companion with the binary model recovers the correct host temperature. The companion temperature recovered is 100 K lower than the input temperature and the RV is different by  $2 \text{ km s}^{-1}$  which is around one third the FWHM.

In this case with a companion RV offset,  $rv_2$ , near  $0 \text{ km s}^{-1}$  the host and companion lines are blended. The same spectral lines from both components are trying to match to the same features of the spectra, making it more difficult to recover the companion parameters. In the bottom right panel there appears to be multiple minima for different  $rv_2$  and  $T_{\text{eff}2}$  combinations, which we assume is partially due to the small  $rv_2$ .

In both simulations the reduced  $\chi^2_{\text{red}}$  for the binary model is closer to 1. This is not surprising as the binary model contains extra parameters. As mentioned above, we need to be careful, as the extra components from the binary may just happen to fit components of the noise when a binary is not present, or in our case has a low flux ratio. **We analysis the significance between the two models using the “Bayesian Information Criterion” (BIC)** (Schwarz, 1978);

$$BIC = n \ln(m) - 2 \ln(\hat{L}). \quad (5.4)$$

Here  $n$  and  $m$  are the number of parameters and data points respectively and  $\hat{L}$  is the maximum of the Gaussian likely-hood function

$$\hat{L} = \left( \frac{1}{\sigma \sqrt{2\pi}} \right)^m \exp \left( -\frac{\chi^2}{2} \right), \quad (5.5)$$

written in terms of  $\chi^2$  and a fixed  $\sigma$  for all data points. The maximum likely-hood of a Gaussian distribution is equivalent to minimizing the  $\chi^2$ . In both simulations  $\Delta BIC > 10$  so the preference of the binary model, with the lower BIC value, over the single component model is considered *significant*.

### 5.3.2 HD211847 observation

HD 211847 is the best candidate for detection as it has a  $155 \text{ M}_J$  low-mass star companion Moutou et al. (2017). The angular separation of the two bodies is 222 mas (or 11.3 au). Even though it is not a BD it has the highest estimated flux ratio in our sample, of 0.03 based on the Baraffe et al. (2015) evolution models and the known companion mass (see. Table ??). The angular separation of HD211847B is 222 mas with a projected distance of The result of applying  $\chi^2$  fitting to the second observation of HD 211847

is shown in Figure 5.3.

For this target the metallicity of both components was fixed to 0.0 and the logg for the host was fixed at 4.5. The logg for the companion is fixed to 5.0, based on the Baraffe et al. (2015) evolutionary models for the given companion mass and system age. The orbital solution was used to refine the RV search space of both components. The span RV for the companion was extended until a value inside the RV bounds was found.

Again the top left panel of Figure 5.3 shows the recovery with a single component model with the other three for the binary model. The single component model finds a temperature of 5 900 K for the host with a  $rv_1$  of  $7 \text{ km s}^{-1}$ . This is 200 K and  $0.4 \text{ km s}^{-1}$  different above the expected parameters. The binary model finds a host temperature of 5 800 K, which is the second closest model to the literature value,  $>100$  K different. The host RV value recovered with the binary model is  $7.6 \text{ km s}^{-1}$ , which is  $1 \text{ km s}^{-1}$  higher than expected. For the single component model there is a barely noticeable secondary minima near this  $7.6 \text{ km s}^{-1}$  RV value recovered by the binary model. Again these RV differences are smaller than the FWHM of the lines. The  $3\sigma$  contour is small, just visible on the right hand side of the star in the bottom left panel, and hidden behind the markers in the other panels.

For the companion in the binary model, on the right side of Figure 5.3, the minimum  $\chi^2$  for the companion temperature is at the upper temperature limit of the grid shown. If we extend the grid of companion temperature towards higher temperatures the best fit location continues to increase in temperature, continually hitting the upper limit until it is close to the host temperature,  $>2000$  K above the expected companion temperature. When the companion temperature becomes this high it also affects the recovered parameters for the host star to offset the features of the brighter companion.

The  $\chi^2_{red}$  values for the single and binary models are 21 and 19 respectively, far from 1, indicating that both models are a poor fit to the observations. **The  $\Delta BIC = 3812 > 10$  indicating that binary model is still preferred.** We plot the binary model for the best fit solution alongside the observed spectra in Figure 5.4. We see that there is a large spectral mismatch between the synthetic models and the observation. Extra wavelength masking was applied to many of the largest mismatched synthetic lines to remove their influence. The grey areas mark regions which have been masked out, either from the centres of deep telluric lines (the thin masks matching spectral gaps), or the more prominent mismatched lines in the synthetic spectrum excluded from the  $\chi^2$  analysis. One clear example of a mismatched line is a synthetic line at 2 132.5 nm that is clearly not observed in detector 2 (top right). Even with the majority of the mismatched lines removed the detection of the companion was still unsuccessful.

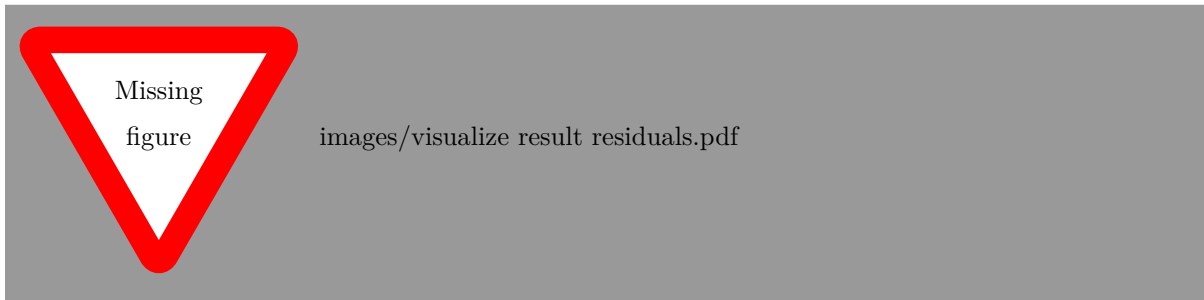
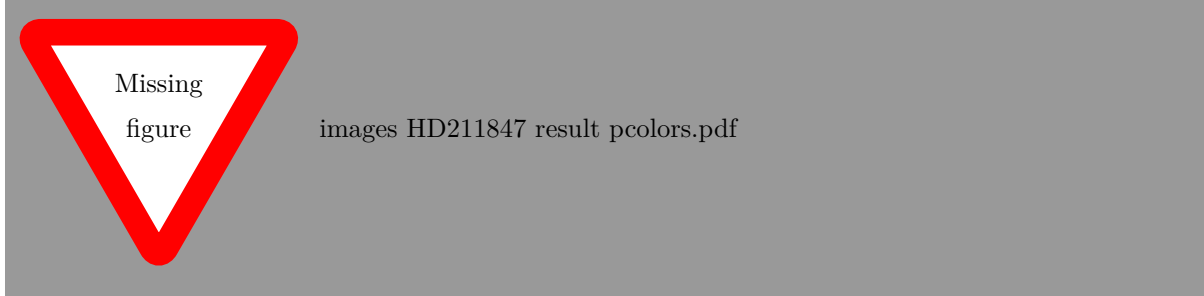
For detectors 1 and 2 it appears that the synthetic spectra contain many more deeper lines than observed. For detector 3 the red half of the detector was masked out as there appears to be an offset between the observed lines. With 3–4 lines that appear to be consistently offset from the observation it could be a wavelength calibration issue, although the telluric lines appear to be sufficiently corrected in this region, attesting for the quality of the wavelength calibration, and making it incompatible with the offset. For detector 4 the observed lines do not agree at all with the models. With many observed lines not in the model and only one line with some agreement in wavelength, detector 4 is masked out completely and not used in the  $\chi^2$  fit. Individual inspection of the  $\chi^2$  results for each detector also revealed that there was a large discrepancy between the 4th detector and the other three, with a different RV value for the host star and a  $\chi^2$  values an order of magnitude higher. The edge of a deep Hydrogen line (Brackett- $\gamma$ ) off the edge of the detector 4 is also clearly seen in the continuum of the model  $>2162$  nm.

We applied this same method to the remaining targets, with similar results. In brief, we conclude

**Figure 5.3:**  $\chi^2$  result grid for observation 2 of HD 211847, similar to Figs. 5.1 and 5.2. The top right plot shows the application of a single component model ( $C^1$ ) while the other three are using a binary model ( $C^2$ ). Both left hand panels show the distribution of host temperature and host RV. The top right panel shows the distribution for host and companion temperature, and the bottom right the companion temperature and radial velocity. The red circles indicate the literature values or calculated parameters for the target while the yellow star indicates the minimum  $\chi^2$  solution. The error bar on the  $T_{\text{eff}1}$  is from the literature while the error bars on  $rv_1$  and  $rv_2$  are calculated by propagating the orbital parameter uncertainties through the radial velocity equation. The white line shows a  $3\sigma$  confidence level about the minimum  $\chi^2$  solution grid point, not always visible here due to the large  $\chi^2$  values.

**Figure 5.4:** Comparison between the observed HD 211847 spectrum (blue) and the best fit synthetic binary model (orange dashed) for each detector. The bottom section of each panel shows the residuals between the parts of the observation used in the  $\chi^2$  fit and recovered binary model ( $O - C^2$ ) in purple. The red dashed line shows the difference between the recovered binary model and the binary model with the exact same parameters except for the estimated companion temperature of 3 200 K ( $C^2[3200 \text{ K}] - C^2$ ). The grey shading indicated the wavelength regions where masking has been applied. The thinner masked regions that match with cuts in the observed spectra are where the centres of deep ( $>5\%$ ) telluric lines that have been masked out are.

that the companion spectra cannot be correctly detected in our data using this method.



### 5.3.3 Companion injection-recovery

To determine the detection limits for this method we employ an injection-recovery approach. We take the observed spectra and inject onto them a synthetic companion, at the absolute flux ratio to which it would have been added to a synthetic host with the same parameters. The injected companion RV is set

to  $100 \text{ km s}^{-1}$  so that the companion lines are well separated from the lines of the host. This separation chosen is slightly larger than what we have with our observations,  $rv_2$  given in Table 4.3.

We restrict the search space by fixing the host parameters  $T_{\text{eff}1}$  and  $\log g_1$  to those recovered fitting the non-injected spectra by a single component model. The wavelength masking is used to reduce the level of mismatch between synthetic and observed spectra.

We apply the recovery method developed above on the injected spectrum, leaving only the companion  $T_{\text{eff}2}$  and  $rv_2$  parameters free, to recover the injected companion. We repeated this for injected companions with temperatures below 5 000 K.

We also perform the injection-recovery with synthetic host spectra, representing each target. The wavelength range of the synthetic spectra used for this is three sections interpolated to 1 024 values in the wavelength span of detectors 1, 2, and 3. For each section, Gaussian noise is added at the level measured in the corresponding detector for the in the observation of the target being represented.

In Figure 5.5 we show the results of the injection-recovery on HD 30501. The blue dots represent the recovered companion temperature when injected into real observations, while the orange triangles represent injection into a synthetic host. Error bars of  $\pm 100 \text{ K}$  are included to indicate the grid size, and do not come from the recovery itself. The black dashed diagonal is the temperature 1:1 relation, where a correctly recovered companion should lie.

The grey shaded region indicates the  $\pm 1000 \text{ K}$  temperature range explored for the injection-recovery of the companion. This shows how the bounds of the grid are recovered at low temperatures.

For HD 30501 the injection onto synthetic and observed spectra produce similar results. At temperatures above 3 800 K in both the real and synthetic the injected companion is recovered within 100 K. For injected companion temperatures below 3 800 K the temperature recovered is systematically higher than the injected value. This indicates that the companion is not correctly recovered and is affected by the added noise. We determine this temperature to be the upper temperature limit for the recovery. For the other stars we could not conclude on the upper limit due to spectral mismatch issues. In these cases we use the results from the synthetic injection to derive a temperature recovery cut-off for each target, each simulated with the closest host star spectrum.

In Figure 5.6 we show the minimum  $\chi^2$  for each companion temperature in the recovery grid. We do this for 7 different injected companion temperatures between 2 500 and 4 500 K. For the higher temperature companions, the  $\chi^2$  is parabolic in shape, recovering the correct temperature, as expected. At lower temperatures there is a strong asymmetry in the  $\chi^2$  with it flattening out on the lower temperature side. The 1-, 2-, 3- $\sigma$  values (with 2 degrees of freedom) of 2, 6 and 11 above the minimum  $\chi^2$  are not shown in the bottom panel of Figure 5.6 which is a close-up around the minimum  $\chi^2$  as are indistinguishable in the top panel due to the  $\chi^2$  y-scale. The black vertical line indicates the 2 300 K temperature limit of the PHOENIX-ACES models.

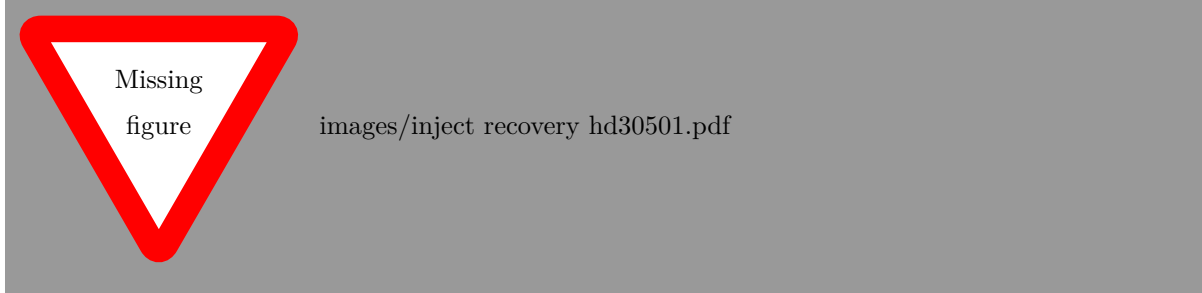
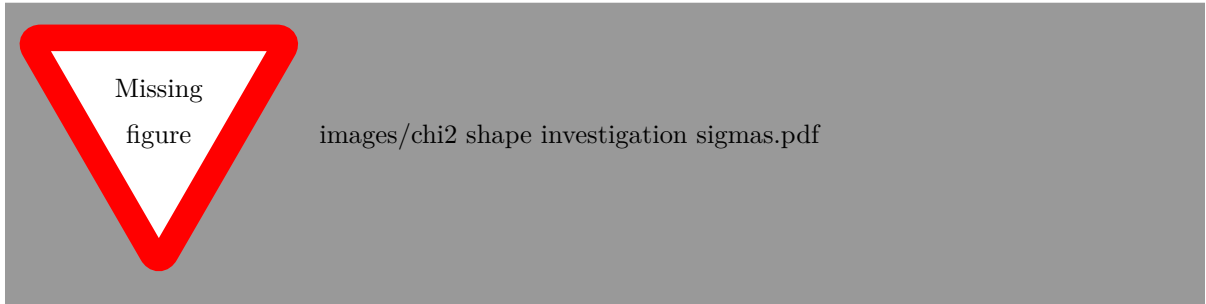


**Figure 5.5:** Result of simulated injection-recovery of synthetic companions on HD 30501. The blue dots and orange triangles indicate the recovered companion temperature for the observed and synthetic spectra respectively. The  $\pm 100$  K error bars are the grid step of the synthetic models. The black dashed diagonal shows the 1:1 temperature relation. The grey shaded region indicates the  $\pm 1\,000$  K temperature range explored. Gaussian noise added to the synthetic spectra was derived from the observed spectra.

**Figure 5.6:** (top) Companion temperature versus  $\chi^2$  for simulations with different injected companion temperatures. Other fixed parameters for these fully synthetic simulations was  $T_{\text{eff}1} = 5\,200$  K,  $\log g_1 = 4.5$ ,  $\log g_2 = 5.0$ , and both  $[\text{Fe}/\text{H}] = 0.0$ . A fixed Gaussian noise corresponding to a SNR of 300 was used. (bottom) A close up view of  $\chi^2 < 15$ . The three horizontal grey lines indicate the 1, 2, 3 sigma with 2 degrees of freedom. The vertical dotted lines indicate the location of the minimum  $\chi^2$  recovered for each companion. The black solid vertical in both panels shows the 2\,300 K cut-off of the PHOENIX-ACES models



Using the temperature cut-off values, we derive an upper mass limit for the companions around our stars using the Baraffe et al. (2015) evolutionary models, finding the closest point matching the spectral temperature cut-off and  $\log g = 5.0$ . These values are given in Table 5.3 and are between 560 and 618  $M_{\text{Jup}}$ . The flux ratio between the cut-off and the host star are also provided for, being between 5 and 15% in this wavelength span.

Hoeijmakers et al. (2015) Context. The spectral signature of an exoplanet can be separated from the spectrum of its host star using high-resolution spectroscopy. During these observations, the radial component of the planet's orbital velocity changes, resulting in a significant Doppler shift that allows its spectral features to be extracted.

Aims: In this work, we aim to detect TiO in the optical transmission spectrum of HD 209458b. Gaseous TiO has been suggested as the cause of the thermal inversion layer invoked to explain the dayside spectrum of this planet.

Methods: We used archival data from the 8.2 m Subaru telescope taken with the High Dispersion Spectrograph of a transit of HD 209458b in 2002. We created model transmission spectra that include absorption by TiO, and cross-correlated them with the residual spectral data after removal of the dominating stellar absorption features. We subsequently co-added the correlation signal in time, taking the change in Doppler shift due to the orbit of the planet into account.

Results: We detect no significant cross-correlation signal due to TiO, though artificial injection of our template spectra into the data indicates a sensitivity down to a volume-mixing ratio of  $\sim 10^{-10}$ . However, cross-correlating the template spectra with a HARPS spectrum of Barnard's star yields only a weak

**Table 5.3:** Upper mass limits of target companions assuming a companion  $\log g=5.0$ . Masses are derived from Baraffe et al. (2015) evolutionary models using  $T_{\text{eff}}$  and  $\log g$ . The flux ratio  $F_2/F_1$  is the absolute flux ratio between the cut-off temperature and the target host star.

Target	$T_{\text{eff}}$ cut-off (K)	$F_2/F_1$	Mass limit ( $M_{\text{Jup}}$ )
HD 4747	3 900	0.084	598
HD 162020	3 900	0.147	598
HD 167665	3 800	0.054	560
HD 168443	4 000	0.094	618
HD 202206	3 900	0.075	598
HD 211847	3 900	0.079	598
HD 30501	3 800 <sup>a</sup>	0.106	560

<sup>a</sup> From observed spectra

wavelength-dependent correlation, even though Barnard’s star is an M4V dwarf that exhibits clear TiO absorption. We infer that the TiO line list poorly matches the real positions of TiO lines at spectral resolutions of  $\sim 100\,000$ . Similar line lists are also used in the PHOENIX and Kurucz stellar atmosphere suites and we show that their synthetic M-dwarf spectra also correlate poorly with the HARPS spectra of Barnard’s star and five other M dwarfs. We conclude that the lack of an accurate TiO line list is currently critically hampering this high-resolution retrieval technique.,

### 5.3.4 Junk from paper about BT-settl

Alot of this section needs to be cut out, lots of repeats and it is not well structured. Basically it will say there is this other model that is better for BDs as it differs “like this” but Fig. ref fig:hd211847-models show that it will also have strong mismatch to make it difficult to recover.

The BT-Settl (allard et al 2009, 2010 2011 2012 baraffe2015) models, a different flavour of Phoenix models, are more suitable for BD atmospheres as they include the formation of dust/cloud and hydrodynamical modelling atmospheric mixing/settling for atmospheres with  $T_{\text{eff}}$  below  $\sim 2600\text{ K}$ . These are valid across the regime from stars to BDs as cool as 400 K. The PHOENIX-ACES models completely avoid the modeling of clouds and settling by the lower temperature restriction of 2300 K.

The PHOENIX-ACES models dust in equilibrium with the gas phase but ignores the dust opacity and does not include any settling. It does however include a new Astrophysical Chemical Equilibrium Solver (ACES, Barman 2012); adds parametrisations for the mass and mixing-length; and uses the Asplund et al. (2009) solar abundances. All these modifications together make it difficult to quantify the spectral changes from each individual change.

The two of the recent “flavors” are the BT-Settl (Allard et al., 2010; Baraffe et al., 2015) and the PHOENIX-ACES (Husser et al., 2013) which use versions 15.5 and 16 of the PHOENIX code respectively.

Even though the BT-Settl models are more suited for the entire range of BD temperatures, we restrict ourselves to the PHOENIX-ACES synthetic spectra for a number of reasons. The ease of use and availability from the spectral library webpage<sup>5</sup>. The ease of use using the Starfish tools, a wide parameter

<sup>5</sup> [http://phoenix.astro.physik.uni-goettingen.de/?page\\_id=15](http://phoenix.astro.physik.uni-goettingen.de/?page_id=15)

range and fairly consistent parameter grid span, and the effective radius of the modelled star provided in the fits header.

These were not used in this instance for a couple of reasons, the ineffectiveness to produce a reliable detection on the observations using PHOENIX ACES spectra for our largest companions, which fall well within the PHOENIX ACES temperature limit.

The PHOENIX-ACES models also provide dimensions of effective radius of the star, in the header. This is required for the method presented here as we need to scale the spectra by their respective surface area when combining together. This PHOENIX-ACES lower temperature limit restricts its use to only the higher mass BD companions in our sample ( $> 0.08M_{\odot}$  at 5 Gyr from the Baraffe et al. (2003) models).

The most recent BT-Settl spectral library designated CIFIST2011\_2015<sup>6</sup> (Baraffe et al., 2015) is only available for 1 200–7 000 Klogg=2.5 to 5.5 and a fixed metallicity and alpha of 0 and includes newer Caffau et al. (2011) solar abundances.

The newer PHOENIX-ACES models are limited to  $T_{\text{eff}} > 2300$  K which only cover the larger BDs. To evaluate the lower mass BDs we use the **other model**, more suitable for cooler BDs and low mass star as they incorporate modeling of dust, clouds etc...

The spectral model libraries were accessed using the useful “grid tools” provided in the Starfish<sup>7</sup> Python package(Czekala et al., 2015).

Both sets of synthetic models do not handle the affects of radiation from a neighbouring star, which may have an affect on the binary orbits here.

PHOENIX-ACES models dust in equilibrium with gas phase but ignores the dust opacity and does not include any mixing/settling in cooler atmospheres. This is avoided by having a minimum library  $T_{\text{eff}} = 2300$  K. This unfortunately limits the use of this library for this technique to the larger mass companions in our sample. For example a  $T_{\text{eff}} = 2300$  K corresponds to a BD with  $M \sim 0.08M_{\odot}$  at 5 Gyr from the Baraffe et al. (2003) evolutionary models.

Even though the BT-Settl models are more suited for the entire range of BD temperatures down to 400 K, through hydrodynamically modeling the mixing and settling of dust/clouds, we restrict ourselves to the PHOENIX-ACES synthetic spectra in this work for a number of reasons. The ease of use and availability from the spectral library webpage<sup>8</sup>. The effective radius of the modelled star are provided in the fits header and required for the calculation of the flux ratio.

The most recent BT-Settl spectral library designated CIFIST2011\_2015<sup>9</sup> (Baraffe et al., 2015) is only available for 1 200–7 000 Klogg=2.5 to 5.5 and a fixed metallicity and alpha of 0 and includes newer Caffau et al. (2011) solar abundances.

The BT-Settl grids were harder to obtain and use.

As we do not recover suitable results for HD211847 which is supposed to have a temperature around 3 400 K we suspect that it is not possible for lower temperature either so don’t try to extend to the BT-Settl models.

**PHOENIX ACES defines grid as Teff,logg and Mass which can then be used to determine Radii. See (Husser et al., 2013) section 2.3.1 Mass.**

Both BT-Settl and aces are spherical ...

<sup>6</sup> [https://phoenix.ens-lyon.fr/Grids/{BT-Settl}/CIFIST2011\\_2015/](https://phoenix.ens-lyon.fr/Grids/{BT-Settl}/CIFIST2011_2015/)

<sup>7</sup> <https://github.com/iancz/Starfish>

<sup>8</sup> [http://phoenix.astro.physik.uni-goettingen.de/?page\\_id=15](http://phoenix.astro.physik.uni-goettingen.de/?page_id=15)

<sup>9</sup> [https://phoenix.ens-lyon.fr/Grids/{BT-Settl}/CIFIST2011\\_2015/](https://phoenix.ens-lyon.fr/Grids/{BT-Settl}/CIFIST2011_2015/)

### 5.3.5 Incremental changes

#### incremental changes in models are small

We took the synthetic models and investigated how the synthetic binary changed as the model parameters were incremented. For the temperature of the companion to be incremented by 100 K this resulted in change to the spectrum with a std of XXX. This is around a SNR of around 500. The change in the models with incremental changes in temperature is small, Changes in log and feh are larger but we fixed these for the application above.

### 5.3.6 Note about a target - discussion of results

Another example is HD 162020, which has the lowest orbital period (8.4 days) of our targets. It should have been possible to obtain an optimal pair of observations in one semester, but the second observation was taken immediately following the first. This means that the  $\delta\text{RV} = 0.363 \text{ km s}^{-1}$  between the two observations, is comparable to the  $\Delta\text{RV}$  that occurs during each individual observation. With tighter scheduling restrictions this target could have been observed with the optimal RV separation at the extrema of  $\Delta\text{RV} = 2K_2$ ). Whether the flux ratio of  $7e^{-6}$  for this target and the interaction of different spectral lines would have made it possible to recover companion mass is a separate issue.

#### 5.3.6.1 Wavelength range

The wavelength choice for the spectra analysed here, observed with the intention to apply the spectral differential technique, was selected due to the location of the  $K$ -band telluric absorption window. This wavelength range, with a narrow wavelength range  $\sim 50 \text{ nm}$  set by the CRIRES instrument. This wavelength range is likely not the best choice for the proposed study. [may contribute to the poor results](#) [finish this line](#)

For instance Passegger et al. (2016) used four different spectral regions for the precise parameter determination of M-dwarfs. Specific lines from the different wavelength regions are affected differently by the model parameters:  $T_{\text{eff}}$ ,  $\log g$ , and [Fe/H]; and are used to break degeneracies in the PHOENIX-ACES parameter space.

Changing the wavelength coverage to regions with lines sensitive to stellar parameters for both stars and BDs, as well as using a larger wavelength range that will be achieved by CRIRES+, may help to improve the recovery results of the companion recovery technique presented here. We note that if the wavelength range is increased by taking separate observations at different wavelengths, not covered by a single exposure, then changes in the RV of both components between the different wavelength observations may need to be accounted for.

Try some Cross-correlations on simulations.

[finish this line](#)

Try my simulations with much larger wavelength range. 50, 100, 600 nanometres?

Try cross correlation at a different wavelength 2.3 micron?

Try cross correlation with much larger wavelength range. 50, 100, 600, 1 000 nanometres?

# Chapter 6

## NIR information

### 6.1 Overview

The pursuit of detecting exoplanets, especially “habitable” and “Earth-like” planets, requires state-of-the-art instrumentation with high precision. One of the key detection methods, the Radial Velocity (RV) method, measures the wobble induced on the Star by the planet as they orbit their common barycentre .

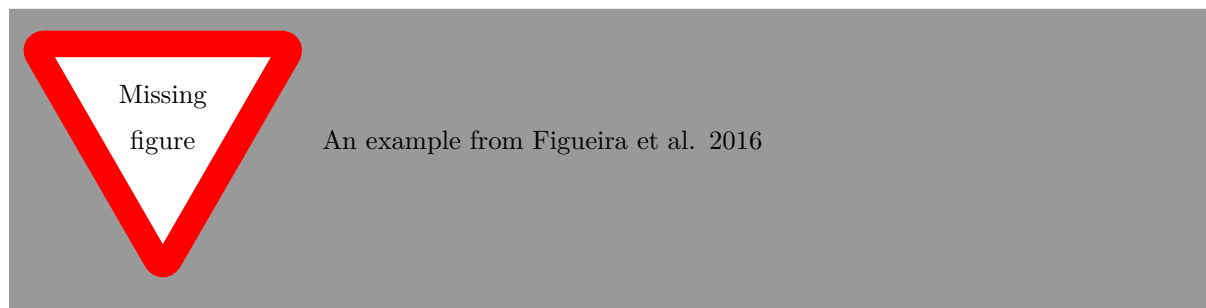
rv method

add Some stuff about mass and period from pedros paper

A increase in the number of nIR spectrographs is increasing to focus on cooler M-dwarfs stars which have a easier\* chance of detecting Earth-like planets in the habitable zone. SPIRou, NIRPS and CARMENES. Also CRIRES+... This work continues the assessment of RV precision levels possible in this domain. A more precise measurement can be achieved from X band then the Y-band... or in order XYZ of precision.

Check mission statements for these

For example from Figueira 2016 see figure



This work is not directly related to detecting exoplanet atmospheres themselves but investigates the theoretical and observed RV precision of M-dwarf spectra in the nIR. This has previously helped the aid the direction of instrument design by identifying the wavelength regions with the best RV precision (Figueira et al., 2016) but can also help in the planning of observations, by understanding how the precision changes with spectral type and observed SNR. This can help in detecting the presence of “habitable Earth-like” planets around M-dwarfs which will likely have their atmospheres eventually probed.

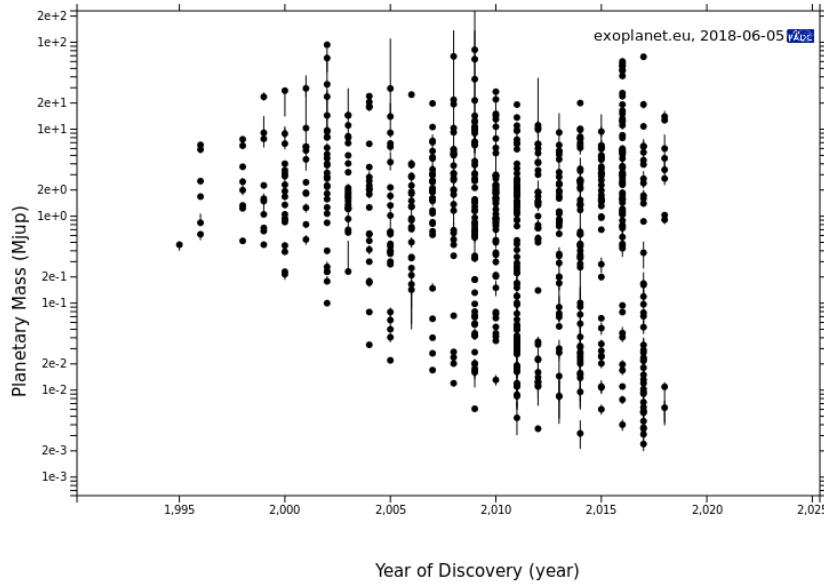


**Figure 6.1:** Mass of discovered planets verse year. From Exoplanet.eu

## 6.2 Radial velocity precision

The first detections of planets with the RV technique **Queloz 2995** discovered the mass and close in hot-Jupiter planets. These are the easiest to detect with the highest RV amplitude.

Over the years the community has push the limits of this technique to smaller and smaller planetary masses. An example is shown in Figure 6.1.

RV amplitude scales with mass of the star  $M_\star^{-2/3}$  and with the planetary orbital period  $P_{\text{orb}}^{-2/3}$ .

The detection of an Earth-mass planet inside the habitable zone around a solar-type star, the RV amplitude is  $10 \text{ cm s}^{-1}$ . If that a planet with the same characteristics is instead orbiting a M-dwarf, the RV amplitude is larger than  $1 \text{ m s}^{-1}$ . This is due to two factors, the smaller mass of the host star, and the closer habitable zone, due to a lower luminosity output of the host.

Artigau et al. (2018) recently compared archival spectra of Barnard's Star, an M-dwarf, and found that state-of-the-art atmosphere models over-predict the *Y*- and *J*-band RV content by more than a factor of  $\sim 2$ , while under-predicting the *H* and *K*-band content by half. **in this work we find similar?**

We are currently aiming to extend this work over the whole M-dwarf range, from M0-M9.

**History of Precision calculations:** Connes 1985 - Bouchy et al. 2001 - photon noise limit on rv measurements. Figueira et al. (2016) - focus on m-dwarfs parameter range to specify new instrumentation windows to focus. Reiners 2017 - CARMENES sample. Some precision pedros school section other precision source  $r^{1.5}$

History of Precision calculations

### 6.2.1 Fundamental photon noise limitation

A optimum technique to calculate the radial velocity precision of a spectrum using the full spectral information is proposed by Connes (1985). Here we provide the radial velocity precision derivation

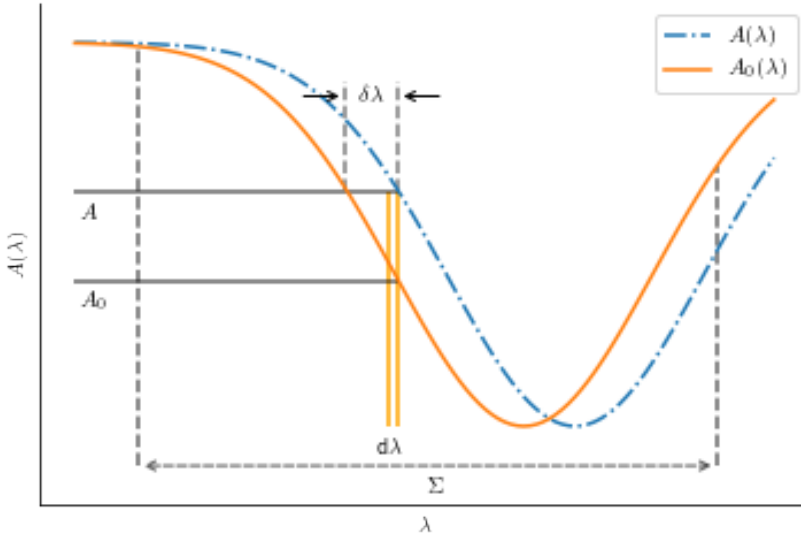


**Figure 6.2:** Arbitrary spectral line with a shift  $\delta\lambda$ , inspired by Connes (1985).  $\Lambda$  is the wavelength range considered.

following Connes (1985); Bouchy et al. (2001); Figueira et al. (2016). A majority of this derivation comes from Bouchy et al. (2001) with some extra notes added to improve the clarity.

For each spectrum there is assigned a quality factor,  $Q$ , to compute the fundamental uncertainty on the radial velocity measurements due to noise. *i am not sure what i am trying to say in this sentence*

The Doppler shift of a spectrum is given by:

$$\frac{\delta V}{c} = \frac{\delta\lambda}{\lambda}. \quad (6.1)$$

Here  $c$  is the speed of light in a vacuum, and  $\delta\lambda$  is the observed shift in wavelength  $\lambda$  caused by the velocity  $\delta V$

Using basic calculus  $\delta y = \frac{\partial y}{\partial x}\delta x$ , and for a Doppler shift that is small compared to the line-width<sup>1</sup>, the observable intensity change at a given pixel can be expressed by:

$$\delta A(i) = A(i) - A_0(i) \simeq \frac{\partial A_0(i)}{\partial \lambda} \delta\lambda \quad (6.2)$$

Rearranging Equation 6.2 for  $\delta\lambda$  and putting it into Equation 6.1, the Doppler shift of then becomes:

$$\frac{\delta V(i)}{c} = \frac{A(i) - A_0(i)}{\lambda(i)(\partial A_0(i)/\partial \lambda(i))} \quad (6.3)$$

This equation shows that the changes in velocity is measured through a change in intensity in the recorded spectrum,  $A(i) - A_0(i)$ , and inversely proportional to the slope of the spectrum,  $\partial A_0(i)/\partial \lambda(i)$ . This equation provides a measurement of the radial velocity shift for each pixel ( $i$ ) in the spectrum. The whole available spectral range,  $\Sigma$ , should be used to increase the sensitivity of the measurement and decrease the noise. This is achieved by summing the contribution of all pixels using an optimal weight

Change picture spectral range to capital lambda  $\Lambda$

<sup>1</sup> Although Connes (1985) show that this approximation in Eq. 6.2 is adequate under all circumstances

$W(i)$ .

$$\frac{\delta V}{c} = \frac{\sum \frac{\delta V(i)}{c} W(i)}{\sum W(i)} \quad (6.4)$$

Statistically, the optimal weights are proportional to the inverse square of the individual dispersion,

$$W(i) = \frac{1}{\left(\frac{\delta V_{RMS}(i)}{c}\right)^2}, \quad (6.5)$$

where  $X_{RMS}$  is the dispersion on the quantity  $X$ .

The individual dispersion of the velocity change measure  $\delta V_{RMS}(i)$  is the dispersion of radial velocity resulting from several measurements of the reference spectrum all with the same Doppler shift (e.g. zero). Equation 6.3 thus becomes:

$$\frac{\delta V(i)}{c} = \frac{[A(i) - A_0(i)]_{RMS}}{\lambda(i)(\partial A_0(i)/\partial \lambda(i))} \quad (6.6)$$

The noise of the spectrum  $A$  is the quadratic sum of the photon noise  $\sqrt{A}$  and the detector noise  $\sigma_D$ . The spectrum  $A_0$  is considered noise free.

$$[A(i) - A_0(i)]_{RMS} = [A(i)]_{RMS} = \sqrt{\sqrt{A(i)}^2 + \sigma_D^2} \quad (6.7)$$

We can set  $A = A_0$  if we consider the Doppler shift is small and that  $A$  and  $A_0$  have the same intensity level. Using Equations 6.5, 6.3 and 6.7 the optimum weights then become solely dependent on the reference spectrum.

$$W(i) = \frac{\lambda^2(i)(\partial A_0(i)/\partial \lambda(i))^2}{A(i) + \sigma_D^2} \quad (6.8)$$

This weighting function can be modified to mask out and eliminate unwanted lines in the spectrum. For instance in the removal of telluric absorption lines in observed spectra. This is achieved by setting the particular pixel weights to zero.

With the optimal weights set the velocity change measured from the full spectral range  $\Lambda$ , is given by:

Change picture  
spectral range

$$\frac{\delta V(i)}{c} = \frac{\sum \frac{A(i) - A_0(i)}{\lambda(i)(\partial A_0(i)/\partial \lambda(i))} W(i)}{\sum W(i)} \quad (6.9)$$

$$= \frac{\sum \left( \frac{A(i) - A_0(i)}{\lambda(i)(\partial A_0(i)/\partial \lambda(i))} \right) \frac{\lambda^2(i)(\partial A_0(i)/\partial \lambda(i))^2}{A(i) + \sigma_D^2}}{\sum \frac{\lambda^2(i)(\partial A_0(i)/\partial \lambda(i))^2}{A(i) + \sigma_D^2}} \quad (6.10)$$

$$= \quad (6.11)$$

The important quantity for RV measurements is not only the velocity value itself but the dispersion

Finish this  
equation (9 of  
bouchy 2001)

Try the sym-  
bolic package  
from PC

on the measured velocity or the precision,  $\delta V_{RMS}$ . From Equation 6.5 the dispersion is given by:

$$\frac{\delta V_{RMS}}{c} = \frac{1}{\Sigma W(i)} = \frac{1}{Q \Sigma A_0(i)} \quad (6.12)$$

With this the velocity precision is inversely proportional to the sum of the optimal pixel weights.

A spectral quality factor, Q, is defined as for the pure photon noise case, as in Connes (1985); Connes et al. (1996).

$$Q = \frac{\sqrt{\Sigma W(i)}}{\sqrt{\Sigma A_0(i)}}. \quad (6.13)$$

This factor is flux independent and is purely a function of the spectral profile within the spectral range considered. It is a measure of the line richness. For example a spectra with many sharp lines will have a high Q. This quality factor is valid for the pure photon noise case only.

With this quality factor the uncertainty in the velocity change can be rearranged in terms of the spectral quality;

$$\delta V_{RMS} = \frac{c}{Q \sqrt{\Sigma A_0(i)}} = \frac{c}{Q \sqrt{N_{e^-}}}, \quad (6.14)$$

where  $\Sigma A_0(i) = N_{e^-}$  is considered to be the total number of photo electrons  $N_{e^-}$  counted in the whole spectral range considered. From the spectral quality factor and the number of photons collect the fundamental velocity precision can be determined.

The spectral quality depends on the spectral profile of the target as well as the instrumental resolution of the spectrograph (which induces line broadening). The number of photoelectrons counted  $N_{e^-}$  depends on the stellar magnitude, detector efficiency and integration time. It can be estimated using

$$N_{e^-} = P_{avg} * S_{tel} * T_{exp} * \alpha * \Lambda, \quad (6.15)$$

where  $P_{avg}$  is the average monochromatic stellar brightness across the wavelength range  $\Lambda$  in  $\text{photons s}^{-1} \text{cm}^{-2} \text{cm}^{-1}$ ,

$S_{tel}$  is the telescope collecting area in  $\text{cm}^2$ ,

$T_{exp}$  is the integration time in s,

and  $\alpha$  the overall efficiency (including atmosphere, telescope, spectrograph and detector).

This can be used to determine the RV precision for a given instrument, and be useful in exposure time calculators for planning observations.

In the case of several  $\delta V$  measurements computed for  $k$  spectral slices (or spectral orders) then the error on the average  $\delta V$  is given by the error on a weighted average:

$$\overline{\delta V_{RMS}} = \frac{1}{\sqrt{\sum_k \left( \frac{1}{\delta V_{RMS}(k)} \right)^2}} \quad (6.16)$$

We follow Figueira et al. (2016) by exclusively considering a high signal-to-noise regime in which

$A(i) + D^2 \sim A(i)$  can be approximated.

<sup>2</sup>

The in the photon noise limited case we assume that all measurements have same RV then the the object has not Connes (1985) show that the optimal weights for photon limited noise is given by finish this

There is also a optimal weight for detector noise but we are always assume we are in high SNR case and are photon noise limited.

This technique has been tested and demonstrated on observations by Connes et al. (1996) and been used to determine predict the accuracy or performance limits of spectrograph instrumentation Connes (1985); Bouchy et al. (2001) and can influence the design (or use) of spectrographs (e.g. SPIROU (Artigau et al., 2014; Figueira et al., 2016))

Considering that  $\Sigma A_0(i) = N_{e^-}$  is the total number of photoelectrons counted over the whole spectral range then the uncertainty in the velocity change is finally given by:

Does spectrograph pipelines such as HARPS use these equations to measure estimate/precision?

$$\delta V_{RMS} = \frac{c}{Q\sqrt{N_{e^-}}} \approx \frac{c}{Q(S/N)}, \quad (6.17)$$

where the  $SNR = \sqrt{N_{e^-}}$  for large N.

It is convenient to use this version when comparing observed spectra with different S/N.?

### 6.2.2 Prepare phoenix aces models

: # see Figueira et al. (2016)

Convert SED to counts.

Scale to 100 SNR per resolution element in *J*-band.

Convolutions

### 6.2.3 Rotation convolution

Rotation is applied to a non-rotating spectrum by convolution with a rotation kernel. The stellar rotational kernel used is derived in ? ;

$$G(\Delta\lambda) = \frac{2(1-\varepsilon)[1 - (\Delta\lambda/\Delta\lambda_L)^2]^{1/2} + \frac{1}{2}\pi\varepsilon[1 - (\Delta\lambda/\Delta\lambda_L)^2]}{\pi(1-\varepsilon/3)v \sin i} \quad (6.18)$$

$$= c_1[1 - (\Delta\lambda/\Delta\lambda_L)^2]^{1/2} + c_2[1 - (\Delta\lambda/\Delta\lambda_L)^2] \quad (6.19)$$

where

$$c_1 = \frac{2(1-\varepsilon)}{\pi(1-\varepsilon/3)v \sin i}, \quad c_2 = \frac{\frac{1}{2}\pi\varepsilon}{\pi(1-\varepsilon/3)v \sin i}, \quad (6.20)$$

are constants which depend on the rotational velocity  $v \sin i$ .

Here  $\Delta\lambda$  is the wavelength position from the line centre,  $\Delta\lambda_L$  is the maximum lineshift of the line centre at the edge of the stellar disk at which point the Doppler shift is  $v \sin i$ ;  $\Delta\lambda_L = \lambda \frac{v \sin i}{c}$ .

<sup>2</sup> pure detector noise the fluctuation are independent of the spectrum  $A$  and the quality factor for pure detector noise is  $Q_D = \frac{\Sigma \lambda^2 (\partial A_0(i)/\partial \lambda(i))^2}{\Sigma A_0(i)}$  as derived by Connes (1985).

This kernel arises from integrating the rotational velocity profile across the surface of the stellar disk and as such the rotation kernel is bounded in the range  $[-\Delta\lambda_L, \Delta\lambda_L]$  from the line centre. This kernel also accounts for limb-darkening on the stellar disk with the linear limb darkening coefficient used in this work fixed at  $\varepsilon = 0.6$  as done in Figueira et al. (2016).

Since the synthetic models do not have a consistent wavelength grid, the discretization of the convolution kernel onto the changing wavelength grid causes each pixel to be multiplied by a slightly different kernel area. We therefore divide the result by a convolution of a spectrum of ones with the same wavelength resolution to normalize the convolution.

As the Doppler shift  $v \sin i$  is transformed into wavelength by multiplication of  $\lambda/c$  there is a wavelength dependence on the rotation kernel shape.

#### 6.2.4 Instrumental Convolution

Following the rotational convolution the spectra are convolved with Gaussian instrumental profile (IP) with the FWHM constrained by the spectral resolution R,  $\text{FWHM} = \lambda/R$ .

The Gaussian convolution kernel is of the form

$$IP(\Delta\lambda) = \frac{1}{\sigma\sqrt{2\pi}} \exp^{-\frac{\Delta\lambda^2}{2\sigma^2}} \quad (6.21)$$

with  $\sigma = \frac{\text{FWHM}}{2\sqrt{2\ln(2)}}$ , and  $\Delta\lambda$  again the difference from the line centre (normally this would be written as  $(x - \mu)$  where  $\mu$  is the Gaussian centre).

This assumes that the instrument profile of a particular instrument is in-fact Gaussian. This assumption of a Gaussian instrumental profile is a good starting point for high-resolution spectrographs, and shown to be valid for CRIRES (Seifahrt et al., 2010). If the IP of a particular instrument is well characterized, then it could replace the Gaussian IP used here.

For instance Artigau et al. (2018) state that the instrumental profile of a (circular) fibre-fed spectrograph such as HARPS is mathematically equivalent to a cosine between  $-\frac{\pi}{2}$  and  $\frac{\pi}{2}$  with a width equivalent to the Gaussian FWHM.

The integration of a circular fibre is given by

$$IP_{\text{fibre}}(\Delta\lambda) = \cos(B \cdot \Delta\lambda), \quad [-\pi/2B, \pi/2B] \quad (6.22)$$

where  $B = \frac{\text{FWHM}_0}{\text{FWHM}}$  is a scales to give the same area? following the description from Artigau et al. (2018). They also mention that the result using this  $IP_{\text{fibre}}$  are all consistent with the Gaussian kernel.

define fwhm0

CHECKTHISREUSU

#### 6.2.5 Numerical Convolution

In this work the stellar models undergo broadening by convolution with rotation and instrumental profile kernels (Equations 6.19 and 6.21). The convolutions are performed by analysing a single pixel at a time, and selecting the neighbouring pixels that fall within the convolution window<sup>3</sup> for that pixel. The value of the convolution kernel is calculated at the position of each pixel selected, multiplied by the flux of each pixel and then summed to provide the new value at the selected single pixel\*. The shape of the convolution kernels and the size of convolution window are wavelength dependant ( $\text{FWHM} = \lambda/R$  and

<sup>3</sup> Region in which the convolution kernel will affect this particular pixel

$\Delta\lambda_L = \lambda \frac{v \sin i}{c}$ ) and must be calculated separately for each pixel, making the convolution computationally expensive.

However, the computation of the convolution of individual pixels is an “embarrassingly parallel”<sup>4</sup> problem. What this means is that convolution result for pixel  $i + 1$  does not depend on the convolution result obtained for pixel  $i$ . Therefore, parallel processing was implemented to improve the performance of the convolution, roughly dividing the convolution time by the number of processors used.

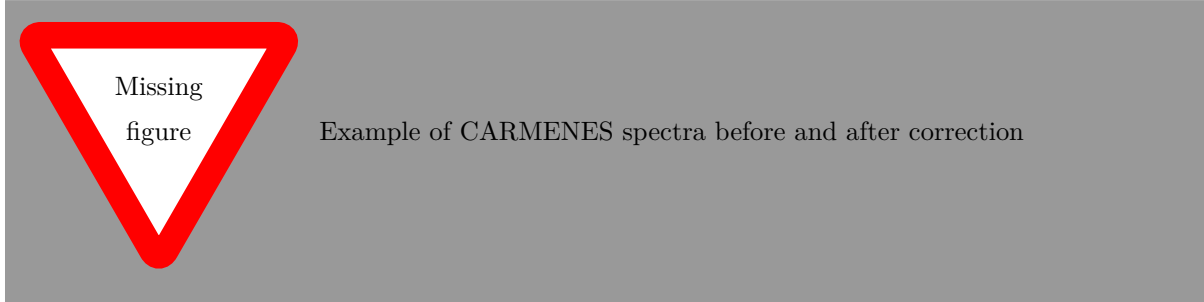
The python package *PyAstronomy* also contains functions that perform rotational and instrumental broadening. Those functions however require that the spectrum have uniformly spaced  $x$ -coordinate spacing which is not a requirement for the implementation of *eniric* used here. *PyAstronomy*, while implemented a “slow” full version of the rotational convolution, with a wavelength dependent kernel, they also provide “fast” convolution kernels that are fixed, taking the central wavelength value. These are significantly faster but are only valid for very short wavelength regions, in which the kernels do not significantly change. They are not suitable for use in this work due to the large wavelength span of spectroscopic bands and the wavelength dependant spacing of the spectra. A comparison of the performance between *PyAstronomy* convolution and the convolutions implemented in *eniric* and used here are given in a *Jupyter* notebook in the repository of “eniric”, basically they fall in between the “fast” and “slow” implementation of *PyAstronomy*.

One factor the needs consideration when convolving with a non-uniformly spaced spectrum is effect of the sampling on the convolution. For instance the number of point inside the convolution, as well as their location will effect the area of the convolution kernel. To normalize the convolution result it is divided by the convolution of a unitary spectrum of ones, with the same spacing. Figueira et al. (2016) performed this unitary convolution separately and applied the normalization afterwards. In the improved implementation the convolution normalization is performed directly after the convolution kernel multiplication at \*. For example for the rotational convolution result of the value for pixel  $i$  becomes  $A'(\lambda_i) = \frac{\sum A(\Delta\lambda_i) \cdot G(\Delta\lambda_i)}{\sum G(\Delta\lambda_i)}$ , where  $\Delta\lambda_i$  are the values between in the range  $\lambda_i(1 - \frac{v \sin i}{c}) \leq \lambda_i \leq \lambda_i(1 + \frac{v \sin i}{c})$ , instead of only  $A'(\lambda_i) = \sum A(\Delta\lambda_i) \cdot G(\Delta\lambda_i)$

By default edge effects are avoided by providing an input spectra sufficiently wider than the desired output spectrum to prevent edge effects on the portion of the spectrum desired. Since two convolutions are preformed one after the other the original input spectrum is selected wider than needed so that no edge effects will be present after both addition of rotation and instrumental broadening by  $v \sin i$  and R.

## 6.3

Preparation of CARMENES spectra.



<sup>4</sup> [https://en.wikipedia.org/wiki/Embarrassingly\\_parallel](https://en.wikipedia.org/wiki/Embarrassingly_parallel)

**Table 6.1:** The wavelength ranges of the nIR spectral bands.

Band	Range ( $\mu\text{m}$ )
Z	0.83 – 0.93
Y	1.00 – 1.10
J	1.17 – 1.33
H	1.50 – 1.75
K	2.07 – 2.35

### 6.3.1 Bands

The bands are selected based on the strong water absorption. This can be seen in the CARMENES spectra in Figure . The wavelength ranges used in this work Figueira et al. (2016) and used in this work are given in Table 6.1.

Add figure here

Add figure here

### 6.3.2 Comparing models to CARMENES.

Already somewhat done in Reiners. (use all spectra). They measured the precision obtained in the spectra.

Band by band like Figueira et al. (2016)? Certain% steps like Bouchy or Artigau

Can do Barnard's star in CARMENES. compared to models in Artigau.

finish this

**Table 6.2:** CARMENES library target selection spanning the M-Dwarf spectral range.

Karmn	Name	SpT	SNR <sub>NIR</sub>	Temp (K)	logg	[Fe/H]	v sin i ( $\text{km s}^{-1}$ )
J20533+621	BD+61 2068	M0.5	257	3772	NaN	-0.01	2.66
J04290+219	BD+21 652	M0.5	212	4037	3.99	-0.21	1.11
J07274+052	Luyten's Star	M3.5	254	3467	NaN	-0.11	NaN
J17578+046	Barnard's Star	M3.5	236	3247	NaN	-0.32	NaN
J11055+435	WX UMa	M5.5	140	3304	NaN	NaN	NaN
J10564+070	CN Leo	M6.0	133	2960	NaN	NaN	NaN
J18356+329	LSR J1835+3259	M8.5	50	2578	NaN	-0.4	37.6
J04198+425	LSR J0419+4233	M8.5	42	NaN	NaN	0.22	NaN

**Table 6.3:** csv2tex table

Karmn	Name	SpT	NIR-SNR	Teff	NaN	FeH	ROT-Vsini
J20533+621	BD+61 2068	M0.5	257	3772.0	-	-0.01	2.66
J04290+219	BD+21 652	M0.5	212	4037.0	3.99	-0.21	1.11
J07274+052	Luyten's Star	M3.5	254	3467.0	-	-0.11	-
J17578+046	Barnard's Star	M3.5	236	3247.0	-	-0.32	-
J11055+435	WX UMa	M5.5	140	3304.0	-	-	-
J10564+070	CN Leo	M6.0	133	2960.0	-	-	-
J18356+329	LSR J1835+3259	M8.5	50	2578.0	-	-0.40	37.60
J04198+425	LSR J0419+4233	M8.5	42	-	-	0.22	-

## 6.4 Metallicity NaN effects

We explore the effect of metallicity and NaN on the spectral quality of spectra in the PHOENIX-ACES library by extending the quality factor and precisions computation to [Fe/H] between -1 – 1 and NaN of 4.0 – 5.5. In Figure 6.3 the variation of quality factor with broadening of  $R=100\,000$  and  $v \sin i = 1.0 \text{ km s}^{-1}$  across the M-dwarf spectral types and the nIR bands is shown. We observed multiple different effects present.

The  $Z$ -band has a large separation in spectral quality due to spectral type, this is because the continuum the  $Z$ -band is severely eroded in the spectra of late M's as they cool. Each spectral type also behaves very differently to a change in [Fe/H] and NaN. For M0 and M3 there is an increase with [Fe/H] below solar metallicity, above solar metallicity the slopes of the lines dramatically increase, especially for M3. For M6 and M9 there is a step slope with [Fe/H] below solar metallicity, which flattens off at solar metallicity, and even decreases for the M9 spectra above solar metallicity. As NaN increases in the  $Z$ -band there is a decrease in quality. There is a consistently large separation between early and late M's that. The quality for M6 is very shallow, while for M9 the quality is nearly flat for NaN=4.0 and 4.5 but then decreases sharply at higher NaN.

$Y$ -band -

$J$ -band -

For the  $H$  and  $K$ -band there is fairly consistent linear trend for all spectral types, with the quality factor increasing with an increase in [Fe/H] and decreasing with an increase in NaN. There is also only a relatively small variation in quality factor due to the spectral type.

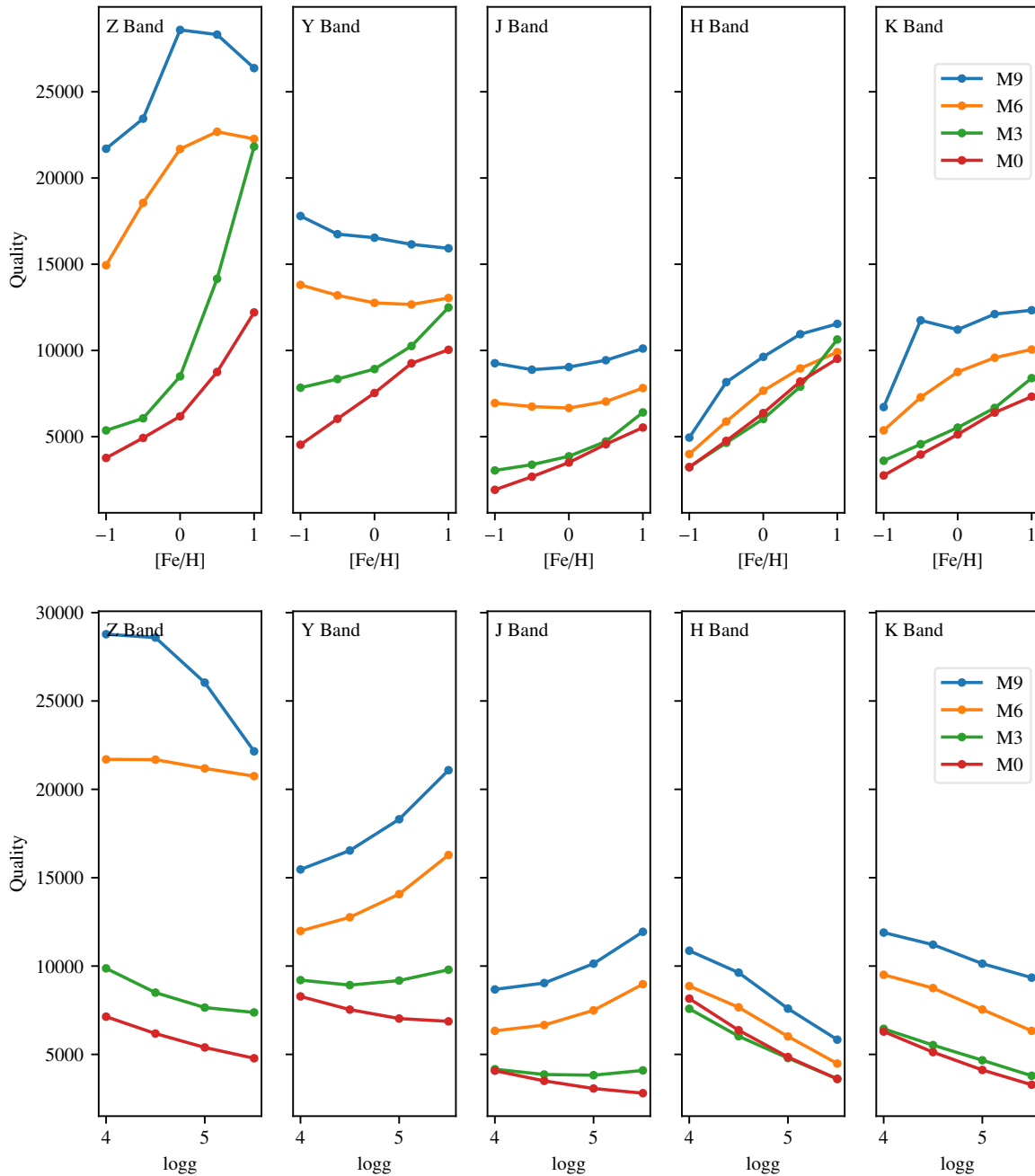


**Figure 6.3:** Quality factor changes across spectral type and bands for variations in  $[Fe/H]$  and  $NaN$ . Broadening values are  $R=100\,000$  and  $v \sin i = 1.0 \text{ km s}^{-1}$ . Top: Quality factor variation of  $[Fe/H]$  between -1.0 to 1.0 at a fixed  $NaN=4.5$ . Bottom: Quality factor variation of  $NaN$  between 4 and 5.5 with fixed  $[Fe/H]=0.0$ . Note a higher quality factor corresponds to an increased RV precision.

## 6.5 Updating RV precision software

To undertake the calculation of RV precisions A large section of this work involved optimizing the original code used in Figueira et al. (2016). Care needs to be taken to optimize the code. The original code used in Figueira et al. (2016) was slow, taking around 2 hours per simulation, this led to multiple weeks of processing time to compute the precision's for the original paper.

In this section we document the changes made to the code in the course of attempting to improving it. Features that change the derived RV precision are specifically documented in detail, with relative precision changes provided.

This work resulted in a submitted software publication Neal et al 2018. with the code available [giuthub](#)

### 6.5.1 Automated testing

To insure that any changes made to the code did not change the underling results. This involved writing automatic tests for the software. This practice is crucial in computer science ins commercial software development but seldom done in research but is becoming more popular. [Some work focused on testing](#) ideology from computer science. Although not perfect implementation I began by adding automated tests to the code to check individual parts of it. Before making changes I created automated tests that would confirm the functionality of pieces of the code. I could then make changes to the code, to improve the performance without worrying that the results were different. Namely that the same precision were calculated in the end.

Functional test and unit tests.

works of software testing in research.

### 6.5.2 Atmospheric masking bug

One thing that was revealed in testing was that there was an error in the application of Condition #2. When the telluric mask was shifted to account for barycentric motion of the earth, and the condition of 3 consecutive pixels in the telluric spectra being lower than the limit (due to the higher sampling) there was an software bug,

A check for this issue was discovered using this unit test.

**Listing 6.1:** Example unit test to catch masking bug.

```
def test_telluric_masking(wavelength, transmission):
    mask = telluric_mask(transmission, depth=0.98)
    mask = barycenter_shift(mask)

    # Checks that the mask is still masking out all telluric lines.
    assert np.all(transmission[mask] > 0.98)
```

The assert statements checks that when the mask is applied to the transmission spectrum again all of the values are outside of any deep telluric regions. A test like this would have caught this bug.

This bug means that all the RV precision values for Condition #2 published in Figueira et al. (2016) incorrect. As the applied masking was unevenly applied Figueira et al. (2016) the new values RV precision values do not all change in the same proportion or direction. Some specific wavelengths and resolutions

are essentially unchanged while other results change by over  $20 \text{ m s}^{-1}$ . Even though there is an error with condition #2 they do not change the overall conclusions of the paper. These are \_\_\_\_\_

add conclusions not affected

### 6.5.3 Performance

There was a major performance bottleneck in the convolution stage, which increased the performance around 250 X itself. The algorithm looped through the pixels in the spectrum, selecting out the necessary section around a given pixel with a comprehension list (for loop if inside range). Turning the result into a numpy array, performing the sum for that pixel and appending it to a list. The performance issue was a python implementation detail to do with applying a comprehension list to a numpy array, then slicing the numpy array with the ends of the list, then converting it back into a numpy array, all of which is preformed on a very large spectrum array. Creating a numpy boolean mask instead of the comprehension list, and applying the boolean mask to the array is much faster. Remaining entirely in the compiled numpy code and not converting between lists and numpy arrays (with involve type checking overhead). This slow operation was done for every pixel/wavelength in the spectrum twice, once for each convolution.

caching convolution result to prevent recomputing the same values. *Joblib*. Also embarrassingly parallel so added multiprocessing support.

The convolution is still the slowest part. There are other methods that work on uniform spectra, which have not been tried to see how they affect the performance or RV precision results. **Insert code samples.**

### 6.5.4 Model extension

The solution is to iterate over each pixel but create a mask array and use numpy indexing to select the required pixel span. (this remains in numpy) These operations all remain in numpy so do not waste time converting between lists and numpy arrays, in which Python need to constantly check and convert the type of each item.

This shows a lesson in the usefulness of test driven development, or testing of code in science.

An normalization step was originally done after the convolution, to normalize out the effect of the convolution on a spectrum of 1s, due to the changing wavelength grids sampling. This was brought inside the main convolution by dividing the pixel by the convolution of a spectrum of ones at the same time. (again in numpy so it is quick)

Parallelization as embarrassingly parallel, the result of each pixel is independent of result of neighbours.

This is not a criticism of the work done by the original author (my supervisor). It is easier to modify a working system then to create one from scratch.

Computer code is not the important part in scientific exploration., although becoming more important in open source and reproducibility efforts. Often forgotten in

```
# Handle any phoenix aces models.
```

## 6.6 Numerical Gradient

One of the key insights from Equations 6.8 and 6.12 is that the radial velocity error is inversely proportional gradient of the spectra, In numerically computing the RV precision, the result is dependent on the numerical method used to compute the gradient. In original code used in Figueira et al. (2016) the

gradient or slope is approximated using the forward finite difference method. The numpy package provides a function to calculate the gradient using a more advanced methods that compute a more precise gradient. In this section we explore the affect of improving the precision of the numerical gradient on the final RV precision.

The simplest way to calculate the derivative using finite difference methods (Quarteroni et al., 2000). These arising from the Newton's definition of the derivative for a continuous function  $f(x)$  which should be familiar from introductory calculus:

$$f'(x) = \lim_{h \rightarrow 0} \frac{f(x + h) - f(x)}{h} .$$

There are three common varieties of the finite difference,

$$FFD = \frac{f(x + h) - f(x)}{h}, CFD = \frac{f(x + \frac{1}{2}h) - f(x - \frac{1}{2}h)}{h}, BFD = \frac{f(x) - f(x - h)}{h} ,$$

called the forwards (FFD), central (CFD), and backwards (BFD) finite differences respectively. The order of uncertainty on the FFD/BFD is  $\mathcal{O}(h)$  while for the CFD it is  $\mathcal{O}(h^2)$  (Quarteroni et al., 2000). As the wavelength spacing between samples/pixels ( $h$ ) is small the CFD will a more precise value for the gradient at each pixel.

In our case  $h$  is the difference in wavelength between the two pixels considered. In the FFD case the gradient at pixel  $i$  becomes:

$$\frac{\partial A_0(i)}{\partial \lambda(i)} = \frac{A_0(i+1) - A_0(i)}{\lambda(i+1) - \lambda(i)}, \quad 1 \leq i \leq n-1. \quad (6.23)$$

At each pixel the numerical derivative is evaluated to the average slope between itself and the following pixel and is an approximation to the derivative. This only extends to  $i = n - 1$ , where  $n$  is the number of points in the spectrum, and the last pixel is dropped from the RV calculation.<sup>5</sup>

The *gradient*<sup>6</sup> method provided in Numpy contains a more advanced numerical methods to calculate the derivative. It uses a *compact difference* method (Quarteroni et al., 2000) which expand the finite differences using a Taylor expansion and then selecting coefficients to minimize the *consistency error*. From the Numpy documentation the consistency error here is

$$\eta_i = \partial f(x_i)/\partial x - [\alpha f(x_i) + \beta f(x_i + h_d) + \gamma f(x_i - h_s)],$$

where  $h_s$  and  $h_d$  are the spacing to the left and right of  $i$  respectively. With Taylor expansion this turns into solving a linear system of equations:

$$\begin{cases} \alpha + \beta + \gamma = 0 \\ -\beta h_d + \gamma h_s = 1 \\ \beta h_d^2 + \gamma h_s^2 = 0 \end{cases}$$

which result in the approximation of the gradient of the central values to be

<sup>5</sup> This is important in the case of Condition #2.

<sup>6</sup> Documentation available at <https://docs.scipy.org/doc/numpy/reference/generated/numpy.gradient.html#id1>

$$\frac{\partial f(x_i)}{\partial x} = \frac{h_s^2 f(x_i + h_d) + (h_d^2 - h_s^2) f(x_i) - h_d^2 f(x_i - h_s)}{h_s h_d (h_d + h_s)} + \mathcal{O}\left(\frac{h_d h_s^2 + h_s h_d^2}{h_d + h_s}\right).$$

If the spectrum is evenly spaced  $h_s = h_d$  reduces to the standard second order CFD approximation:

$$\frac{\partial f(x_i)}{\partial x} = \frac{f(x_{i+1}) - f(x_{i-1})}{2h} + \mathcal{O}(h^2)$$

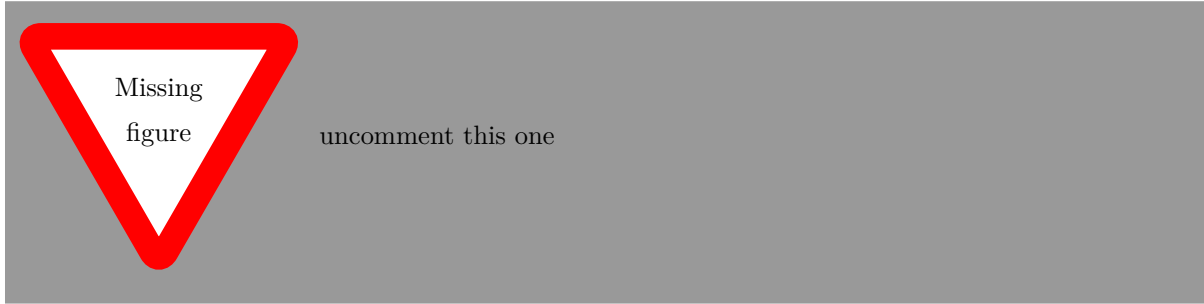
Applying this to our situation, similar to Equation 6.23, we get:

$$\frac{\partial A_0(i)}{\partial \lambda(i)} = \frac{\lambda(i-1)^2 A_0(i+1) + (\lambda(i+1)^2 - \lambda(i-1)^2) A_0(i) - \lambda(i+1)^2 A_0(i-1)}{\lambda(i-1)\lambda(i+1)(\lambda(i+1) + \lambda(i-1))}, \quad 2 \leq i \leq n-1$$

with an uncertainty of  $\mathcal{O}\left(\frac{\lambda(i+1)\lambda(i-1)^2 + \lambda(i-1)\lambda(i+1)^2}{\lambda(i+1) + \lambda(i-1)}\right)$ .

Wavelength spacing  $\delta\lambda$  between pixels is a function of  $\lambda$ , Resolution and sampling choices. Can I do something with this??

The *gradient* function from Numpy implements central differences for the interior points, accurate to second order, and first order accurate one-sided (forward or backward) differences at the boundaries, computed using the same compact difference procedure.



In Figure 6.4 we visualize the gradients of two small spectral regions computed with the original FFD, and the higher precision version incorporated in numpy's gradient function. The top panels contain the spectrum in the small regions shown, indicating a large spectral line and three small lines near the continuum respectively. The derivative of the spectra is shown in the bottom panel with the FFD method shown with *blue squares* and the numpy gradient shown in *green stars*. The *orange circles* are the same as FFD but shifted horizontally to the midpoints between pixels. This is for illustrative purposes and to assess the effect of this offset when calculating the pixel weights.

There are three notable features observed between gradient methods. The first, which is expected from the FFD formulation is that the FFD gradient is offset to the left. The second is that when the horizontal offset is adjusted (orange circles) the gradients lie along the same curve. Both methods are trying to approximate the real gradient function of the spectrum and is again expected. The most important feature observed in this though is that there is a slight over-estimate of the gradient by the FFD method at the peaks. In the bottom panels of Figure 6.4, the points of highest gradient are always from the FFD method (blue/orange). This is the case for all spectral lines and as the optimal pixel weights are proportional to the gradient squared the FFD method will apply slightly higher pixel weights to these

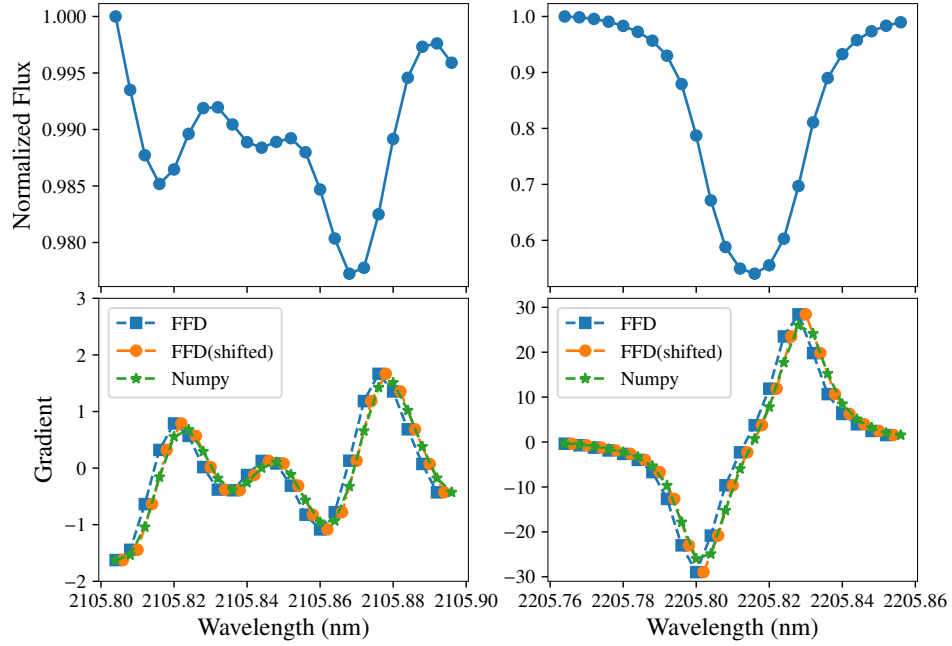


**Figure 6.4:** Visualization of the numerical gradient of some spectral lines. Top: The two spectral regions of a stellar spectrum the left hand slide contains short lines near the normalized continuum while on the right a single deep absorption line is shown. Bottom: The numerical gradients for the spectra shown in the top panels; the original FFD method is displayed with *blue squares* while numpy gradient is shown with *green stars*. The *orange circles* are the FFD version shifted to the mid-points between pixels for illustrative purposes.

**Table 6.4:** The affect of the numerical gradient function on RV precision. The band label VIS and NIR indicate the full visible and nIR bands while CARM<sub>VIS</sub> and CARM<sub>NIR</sub> indicate the two wavelength bands of the CARMENES spectrograph.  $\Delta\lambda$  is a wavelength shift applied to move the FFD values between pixels for this comparison only. The M0 spectra used here had no rotation, or instrument broadening preformed and was normalized to a maximum of 1 in each band. The precision values given here are for accessing the relative precision change due to the different gradient methods.

Gradient method		A	B	C	(B-A)/A	(C-A)/A
Band	$\lambda$ range ( $\mu\text{m}$ )	FFD	FFD+ $\Delta\lambda$ $\delta V_{rms}$ ( $\text{m s}^{-1}$ )	Numpy	$\Delta\delta V$ ratio (%)	$\Delta\delta V$ ratio (%)
VIS	0.38 – 0.78	16.1	16.2	16.9	0.6	4.9
CARM <sub>VIS</sub>	0.52 – 0.96	20.9	21.0	22.0	0.3	5.2
Z	0.83 – 0.93	76.9	77.0	78.8	0.1	2.5
Y	1.00 – 1.10	78.3	78.5	83.8	0.2	7.0
J	1.17 – 1.33	149.3	149.4	156.4	0.1	4.7
H	1.50 – 1.75	119.4	119.5	122.3	0.1	2.5
K	2.07 – 2.35	153.4	153.7	157.7	0.2	2.8
CARM <sub>NIR</sub>	0.96 – 1.71	46.1	46.2	48.0	0.1	4.2
NIR	0.83 – 2.35	36.9	36.9	38.2	0.1	3.6

values, two points per line in the spectrum. The FFD will therefore produce a slightly smaller  $\delta V_{RMS}$  error compared to the more precise gradient function.

In Table 6.4 we calculate the  $\delta V_{RMS}$  using both gradient methods to determine their relative effect on the RV precision.

We took a PHOENIX-ACES spectrum with  $T_{eff}=3900\text{ K}$ , corresponding to M0 spectral type. The full theoretical precision is calculated (no telluric masking applied) with no rotational or instrumental broadening and the maximum of the continuum of each band scaled to 1. In this case the RV precisions are not comparable between bands and are only to assess the direct effect of the changing the numerical gradient. The bands name and the spanned wavelength are given. The columns A, B, C are the RV precision for the different gradient methods. The  $\delta V$  ratios are the relative difference in RV when changing from method A (the original FFD) to methods B and C. In this table column B is the FFD method but with the wavelength shifted to in between pixels, corresponding to the orange circles in Figure 6.4 while column C is the more precise gradient from numpy.

We find that changing to use the gradient from numpy increases the  $\delta V_{RMS}$  by 2.5–7%, (decreasing the RV precision), due to the over-estimated gradient from the FFD method. As the pixel weights Equation 6.8 are also proportional to  $\lambda^2$  column B was computed to assess the effect of the slight wavelength offset on the RV precision, visible in Figure 6.4. This small wavelength shift red-ward does change the RV precision by 0.1–0.6% which is an order of magnitude smaller than the relative change when using numpy’s gradient method.

Changing the method of numerical derivatives will change all the precision values given in the Figueira et al. (2016). This is a small impact on the precision compared to other components of the RV precision. For instance from Equation 6.17 a increase in  $\delta V_{RMS}$  of between 2.5–7% could equally be caused by a small decrease in the SNR from 100 (the value used in Figueira et al. (2016)) to between 95–98.

The current version of the software is now implemented with the gradient method provided by numpy package.

### 6.6.1 Masking Function

Another change made to the software is in the application of the masking function, and the treatment of telluric lines. As suggested in Connes (1985) and Bouchy et al. (2001) a custom masking function can be applied to the individual pixel weights in Equation 6.8, such as:

$$W'(i) = W(i)M(i),$$

where  $M(i)$  is the masking function and  $W'(i)$  are the modified pixel weights. This masking function can be used in particular for the removal of telluric lines, setting those weights to zero and is in essence what is done when wavelength selection is performed; assigning zero weight to all pixels outside the desired wavelength range.

This masking function can be used to easily apply the three conditions presented in Figueira et al. (2016). First the 3 masking functions will be defined, then followed by the quantification of how they differ from the previous implementation. The subscripts on the masking functions correspond to the

three conditions.

$$M_1(i) = 1 \quad (6.24)$$

$$M_2(i) = \begin{cases} 0, & T(i) < \tau \\ 1, & T(i) \geq \tau \end{cases} \quad (6.25)$$

$$M_3(i) = T(i)^2 \quad (6.26)$$

Here,  $T(i)$  is the telluric transmission spectrum, while  $\tau$  is the transmission depth cut-off. For instance to mask out telluric lines deeper than 2%,  $\tau$  would be set at 0.98.

- Condition #1: The first mask,  $M_1$ , is the simplest case in which all pixel weights are treated equally. No telluric line masking is considered.
- Condition #2: In the second mask,  $M_2$ , the telluric line transmission,  $T(i)$  is used to create a boolean mask of 0's and 1's. When applying this mask to the pixel weights, the pixels effected by telluric lines have 0 weight, removing their contribution to the  $RV_{RMS}$ . Accounting for seasonal variation in Earth's barycentric motion can be easily incorporated into this mask, widening the regions masked out.
- Condition #3: The third mask,  $M_3$ , assumes the application of perfect telluric correction consistent with Condition #3. The pixel weights are modified by dividing the flux variance by the square of the transmission spectrum. As the flux variance is the denominator of Equation 6.8, this is equivalent to multiplication of the weights by a mask of the form  $M_3$ .

Having the three masks defined in this way makes the implementation of the RV precision simpler. In the original version there were three separate implementations, one for each condition. With this, as mentioned previously there was an issue with the implementation of Condition #2.

cite the equation when I refer to it

Check this if it is previous

#### 6.6.1.1 Masking order

The order in which the masking is performed is also important. Masking should be applied only after calculation of the pixel weights. As the pixel weights depend on neighbouring points (through the calculation of the gradients), prematurely removing pixels will affect the precision results.

The original implementation of Condition #2 did just this, splitting the spectra into small sections in between the masked off telluric lines. The  $RV_{RMS}$  is calculated for each section and then the results are combined as the weighted error in Equation ?? . Analytically this identical to masking the pixel weights with  $M_2$  but not in practice when numerically implemented.

When the spectrum is split into small sections the number of edges increases and the number of pixels affected by any edge effects increases. Using the FFD method to compute the gradient the last pixel is removed/lost. A spectrum split in  $m$  sub-spectra will therefore lose  $m$  pixels due to edge effects (instead of only 1 pixel with the full spectrum). Even the numpy gradient is not immune to the edge effects in the sub-spectra when splitting the spectrum first. Even though there is no pixels lost, the first and last pixels of each sub-spectra are computed using forward or backward differences, rather than central differences (as they would be in the full spectrum). Hence the gradients and weights of some pixels are slightly changed due to the splitting occurring first.

weighted sum equation

Should I show the working of analytical working out of this in an appendix, or here?

**Table 6.5:** Relative RV precision difference for Condition #2 due to spectral splitting and order of applying the pixel mask. The ratio are the difference between Split and Masked implementations with the same gradient calculation. The last column is the ratio between the Masked versions using the FFD and numpy gradient methods and are consistent with Table 6.4. Results a for an M0 spectral type, with  $v \sin i = 1.0$  and  $R=100\,000$ .

Gradient Band	Split m s <sup>-1</sup>	Masked FFD m s <sup>-1</sup>	ΔRatio %	Split m s <sup>-1</sup>	Masked Numpy m s <sup>-1</sup>	ΔRatio %	Masked ΔRatio %
Z	7.42	7.38	-0.66	7.76	7.77	0.13	5.3
Y	4.75	4.74	-0.22	5.06	5.06	0.06	6.8
J	18.58	18.53	-0.29	19.57	19.57	0.01	5.6
H	6.08	6.05	-0.53	6.25	6.26	0.08	3.5
K	32.21	32.14	-0.22	33.48	33.49	0.05	4.2

We quantify the effect of splitting the spectrum before and after calculating the weights in Table 6.5. The columns label *Split* represents splitting the spectrum before calculating the pixel weights while the *Mask* columns calculate all the pixel weights first and then apply the  $M_2$  mask. The difference in RV precision between both situations and for both gradient methods are given. For the FFD gradient the ordering of masking changes decreases the  $RV_{RMS}$  by 0.2–0.7%, while for the numpy gradient it is increase but an order of magnitude smaller between 0.01–0.13%. The FFD gradient is causes a larger difference as points that were masked out are now included where as with the numpy gradient the end values are always included but their gradients are slightly changed. The last column is the difference ratio between the *Mask* column of both gradient method, this is consistent with Table 6.4 with the differences from two gradient methods between 2–7%. It shows that the difference from changing order of masking is 1-2 orders of magnitude smaller than changing the gradient method.

The code has been adjusted to consistently apply the masking after the pixel weights are calculated. This retains the most pixels, with the more accurate pixel weights. It has also been changed to just apply  $M_2$  rather than splitting and performing the weighted error calculation. This simplifies the implementation did I check this was equivalent in calculating the RV precision.

The results from these spectra for conditions #1 and #3 are consistent with Figueira et al. 2016.

For Condition #2 in which there was an error there is no meaningful relation between the new and old values.

## 6.6.2 SNR scaling

To analyse the relative precision of different spectra they need to normalized to a common reference point. In this section we detail how this was originally done and how this was changed to be adaptable to any library spectra and any reference band.

In the original code this was selected to be a SNR per pixel of 100 at the centre of the *J*-band at 1.25μm. The normalization values for each band,  $v \sin i$  and resolution combination were hard-coded into the analysis. This made it impossible to easily adapt the code to other spectra or parameter combinations.

An automated SNR scaling procedure was created to remove the hard-coded values. This updated code finds the centre point of the band of reference for the given spectrum. Totals the photon count across one resolution element,  $\delta\lambda$ , and then takes the square root. This is using the definition of the SNR as  $SNR = \sqrt{N}$  for large N. This value is then used to scale the spectrum such that the SNR at the

put this some where

put this line elsewhere,

reference point is the desired value.

$$SF = \frac{\sqrt{\sum \delta \lambda A}}{SNR_{desired}} \quad (6.27)$$

$SF$  where  $SF$  is the scaling factor,  $\sum \delta \lambda A$  is the sum of the point in one resolution element and  $SNR_{desired}$  is the desired SNR level requested.

This automated procedure enabled 4 different features.

- The ability to analysis other spectral models, not just corresponding to M0, M3, M6, M9 spectral types. - Scaling to a SNR per pixel level other than 100.
- A SNR per pixel other than 100 can be selected. - Allowing for other sampling levels (if desired)
- Not restricted to a model with 3 samples per resolution element.
- Different reference bands available. Results are not limited to being referenced from the  $J$ -band. For instance the RV precision can now be calculated for a given SNR at the centre of the  $K$ -band. This was one the features requested for the Exposure Time Calculators precision values. For NIRPS we provided precision values relative to each individual band, while for SPIRou they were relative to the J- and H-bands.

The default values for the SNR scaling a still 100 at the centre of the  $J$ -band, but there is now options to easily change these values.

The centre of each band was visually checked to ensure that there were no spectral lines at the reference locations> If a line was present at the reference point its depth variability across spectral types would affect the SNR scaling levels at a greater than the normal change in continuum amplitude/shape. is this needed

As shown in Equation ?? the RV precision is inversely proportional to the SNR level. To access the RV precision of any of the values in Table at a different SNR level you can apply the following

$$RV_{SNR2} = RV_{SNR1} * \frac{SNR1}{SNR2} \quad (6.28)$$

## 6.7 SPIRou and NIRPS ETC

Having this tool to calculate RV precisions efficiently lead to contributions to the Exposure Time Calculators (ETC) for both the SPIRou and NIRPS spectrographs.

In September 2017 we were requested to provide precision calculations for the SPIRou ETC<sup>7</sup>. These were the same table as Figueira et al. (2016) but with a each band referenced to 100 SNR in its own band. The modification to use the centre of any band was made to fulfil this request. Notes on the telluric correction issue affect on Condition 2.

In May 2018 we were requested to provide precision calculations for the NIRPS ETC. This extended the spectral range from M0, M3, M6, M9 at 3 900, 3 500, 2 800, 2 600 K respectively, but to all temperatures between 2 500 and 4 000 K inclusively. This provides a finer resolution coverage over the M spectral type, allowed by the PHOENIX-ACES library. Instrumental resolutions of 75,000 and 100 000 were requested

<sup>7</sup> [http://www.cfht.hawaii.edu/Instruments/SPIRou/SPIRou\\_etc.php](http://www.cfht.hawaii.edu/Instruments/SPIRou/SPIRou_etc.php)

to match the NIRPS instrument. The NaN and metallicity, sampling rate remained at the Figueira et al. (2016) levels of 4.5, 0.0 and 3 respectively. Precisions were provided for SNR of 100 relative to the *J*-, *H*-bands as well as to each band individually. Artigua 2018. (private communication 2018)suggested the truly relevant value is the SNR in *H*-band for NIRPS radial velocities.

The results can be manually generated using “eniric” with the following incantation (after installation and configuration of phoenix library spectra.) **A table of the precisions created for the NIRPS ETC are provided as an online table to our publication *Neal et al. 2018b (in prep.)*<sup>8</sup>**

These values were both calculated and provided using the FFD gradient and with the incorrect masking order for Condition #2, splitting before calculating the pixel weights. As we demonstrated in Section 6.6 and 6.6.1.1 these have a RV precision  $\sim$ 2–7% better than what would be computed with the current implementation.

Check how to  
cite priv com-  
munication  
properly

Include correct  
links

---

<sup>8</sup> Available at [blah](#)

# Chapter 7

## Conclusions

### 7.1 Conclusions from Paper

This work explored two methods to try and detect the faint spectra of stellar companions, using high resolution near-infrared spectra. Two different methods were explored with many limitations uncovered.

The objective of the observations acquired in this program was to apply the differential technique. For the differential technique the observations need to be sufficiently separated, such that the RV of the companion is greater than the FWHM to avoid spectral cancellation of the companion. Unfortunately, due to operational reasons, this condition was not met. As such we employed an alternative method, that we termed the spectral recovery, which ended up revealing different difficulties.

For the spectral recovery the host-companion RV separation should also ideally be greater than the FWHM to avoid blended lines. The spectral mismatch between models and reality in the nIR negatively affects the performance of the synthetic recovery technique on the observed spectra. With all these effects we are unsuccessful in the detection of the nIRspectra of BD companions, with the mass upper-limits set at  $600 M_{\text{Jup}}$  from the synthetic recovery technique.

This work highlights many of the difficulties when dealing with the spectral recovery of nIRspectra. The obstacles to overcome are the data reduction of nIRCMOS detectors, that are not yet at the level of visible CCDs, along with a precise telluric correction and wavelength calibration (two interrelated aspects, as thoroughly discussed). Another important aspect is the mismatch between nIRhigh-resolution spectra and the observed spectra. In spite of the continuous effort of the modelling community, our work, along with several cited contemporary ones, shows that this mismatch is still one of the main factors preventing us from performing spectral recovery in the nIR. This work highlights that this is a compound problem for Brown Dwarfs, for which the spectral models are worse informed due to lack of observations at high-resolution.

Other than the improvement of the spectral models, the observing community can increase their odds of success by paying attention to the scheduling of observations and the wavelength domains to explore. Our work shows that observing in the areas of lower telluric absorption, as is frequently done, is not a guarantee of success due to the scarcity of deep lines in cold objects. Moreover, due to the mismatch between models and observations, the ability to obtain a first spectra before settling on a wavelength range, or changing settings on the fly, is extremely useful for the success of these campaigns.

We hope that this work can act as a guide for the planning of future observations of targets with faint BD and planetary companions with the upcoming generation of high resolution spectrographs in the near- and mid-infrared such as CRIRES+ and JWST observations.

Finish off this

NIR analysis  
work

## 7.2 Future Work

Future of RV precision

---

Precision table  
needs fixed up

# Appendix A

## Artefacts in Optimal Extraction

As mentioned in Section 3.3.3.1 there were artefacts observed from the optimal reduction of the DRACS pipeline. A list of all specific nods of each observation and detector that were observed to contain artefacts and were replaced with the method developed are provided in Table A.1.

With 8 nods per observation, and 4 detectors for the 17 observation there are 544 individual nod spectra. Table A.1 identifies 79 individual nods that contain artefacts which is 14.5%. Only 16/68 (23.5%) detector observations have nods without any artefacts and no single observation has no artefacts in any nod spectra across the 4 detectors.

In Table A.2 a tally is provided of the frequency of artefacts occurring within each nod in the nod cycle. There is a higher number of artefacts occurring in the last two nod, indicating that there may be something to do with the length of the observation. . There is also a larger number of artefacts occurring on the second detector. This maybe coincidence as it is easier to identify the artefacts with a low number of spectral lines from the target, or possibly something physical to do with detector 2. This is beyond the scope of this work,

In this appendix we also provide more example images of the artefacts observed from the optimal reduction of the DRACS pipeline. We have selected one observation and detector for each observed target to show a variety of the artefacts observed.

In each image the top panel contains the 8 nod spectra extracted using the optimal method, including variance weighting. The middle panel contains the rectangular extraction (sum of the aperture), including the bad pixels.

It is clear that the large extracted artefacts occur due to single spikes observed in the rectangular extraction. What is unclear is why it only occurs some of the time.

summary of examples::: they show... almost random big and large spikes but not all.

Maybe transpose Table A.1 to be shorter?

CHANGE # into the ESO identification number 1b 2a etc

Is this significant??

is detector two significant as well?

THESE need to be properly selected and a caption given, one without any artefacts also?

Style needs to be tweaked also

change scale on delta flux of HD 162020-2 chip 1 (it is too large atm)

**Table A.1:** Identification of all the optimally reduced nod spectra which had artefacts that were replaced by the rectangular extractions, corrected for bad pixels. The numbers represent the position in the nod cycle ABBAABBA. The number of the observation for each target is given by #.

Target	#	Detector				Total
		1	2	3	4	
HD 4747	1	8	5, 8	8	1, 5, 8	7
HD 162020	1	-	7, 8	-	-	2
HD 162020	2	-	2	-	8	2
HD 167665	1	2, 4	8	1, 6	4, 5	7
HD 167665	2	2	3	1	8	4
HD 167665	3	6	3, 7	-	8	4
HD 168443	1	-	-	-	7, 8	2
HD 168443	2	-	2, 4	6	8	4
HD 202206	1	-	6, 7	1	-	3
HD 202206	2	5	-	7, 8	-	3
HD 202206	3	8	3	6	6	4
HD 211847	1	-	5, 7	2	4	4
HD 211847	2	2	1, 7	7	8	5
HD 30501	1	7	7	-	8	3
HD 30501	2	7, 8	3, 5, 7, 8	2, 7	2, 3	10
HD 30501	3	4, 8	2, 6, 7	4, 8	7	8
HD 30501	4	1, 2, 4	3	5, 6	6	7
		16	27	17	19	79/544

**Table A.2:** Tally of nod cycle positions in which their optimally reduced spectra were affected and were replaced.

Order Number	1	2	3	4	5	6	7	8	Total
Nod Position	A	B	B	A	A	B	B	A	
Tally	6	10	6	7	7	9	15	19	79

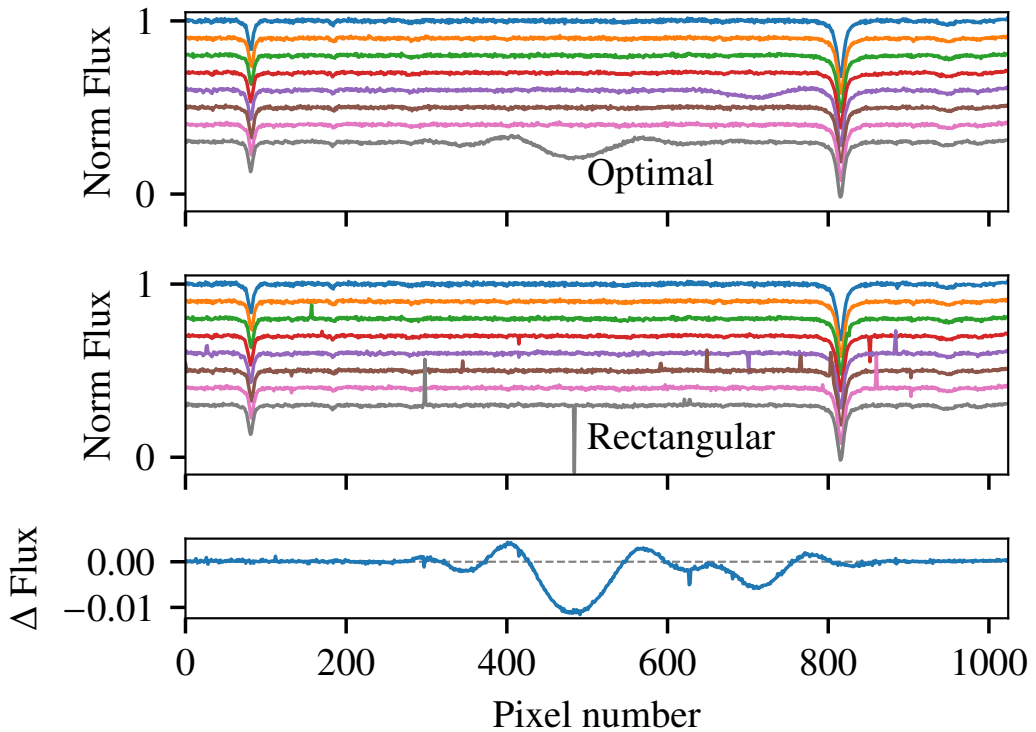


**Figure A.1:** Artefact example for the second detector of HD 4747. The top panel contains the eight normalized nod spectra obtained using optimal extraction. The middle panel shows nod spectra using only rectangular extraction. The bottom panel shows the difference between a combined spectrum using optimal nods only and a combined spectrum in which the identified nods are replaced with their rectangular counterparts as per Section 3.3.3.1. A vertical offset is included between each spectra for clarity. The nod spectra are in observation order from top to bottom. In this example there are artefacts in the 5th (purple) and eighth (grey) nod spectra around 700 and 500 pixels respectively.

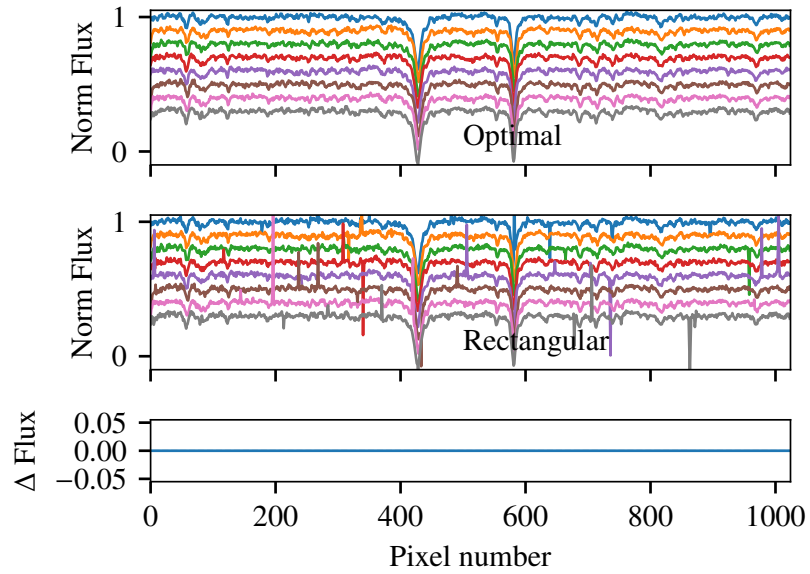


**Figure A.2:** Same as Figure A.1 but for the first detector of the second observation of HD 162020. In this example there are several large spikes observed in the rectangular extraction but they do not appear to effect the optimally extracted nods. [reduce scale of delta flux \(to large atm\)](#).

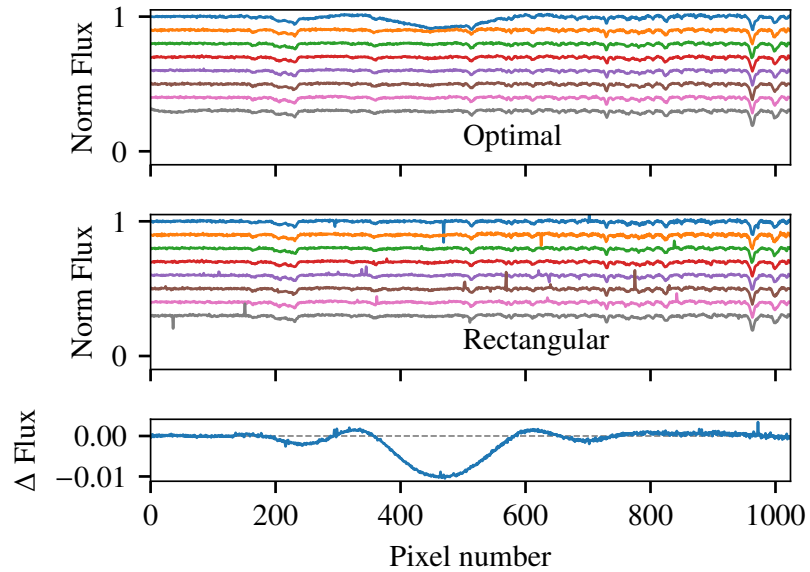


**Figure A.3:** Same as Figure A.1 but for the third detector of the second observation of HD 167665. In this example a small spike in the first spectrum (blue) around pixel 450 causes a extended dip in the optimally extracted nod.

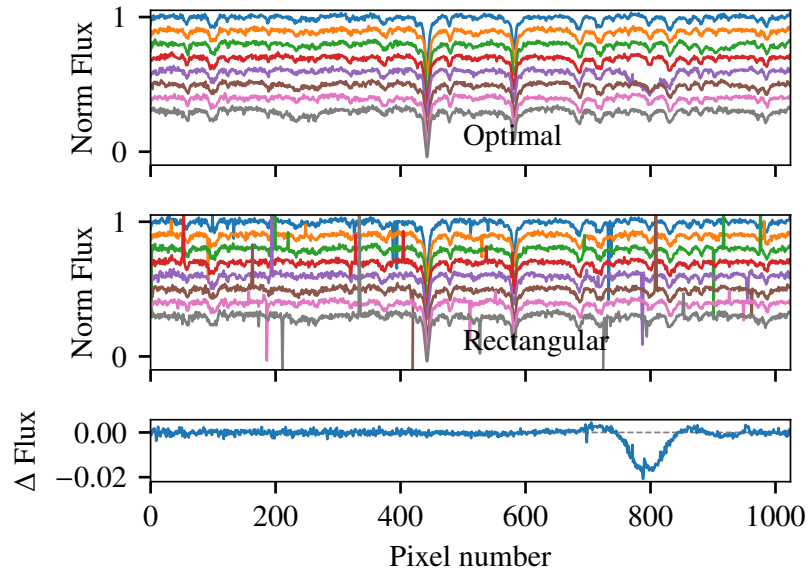


**Figure A.4:** Same as Figure A.1 but for the 1st detector of the second observation of HD 202206. In this example there are several large spike but only one produces an artefact. This is on the 5th nod (purple) around pixel 800.

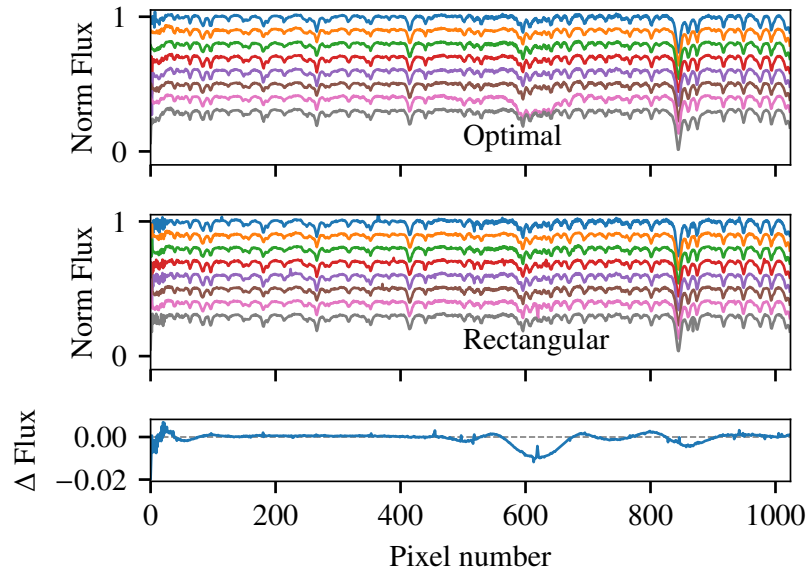


**Figure A.5:** Same as Figure A.1 but for the fourth detector of the first observation of HD 168443. In this example a barely visible spike on the 7th nod (pink) causes a deviation in the optimal nod around pixel 610. There is also a second small spike on the eighth nod (grey) around pixel 850, between two spectral lines.

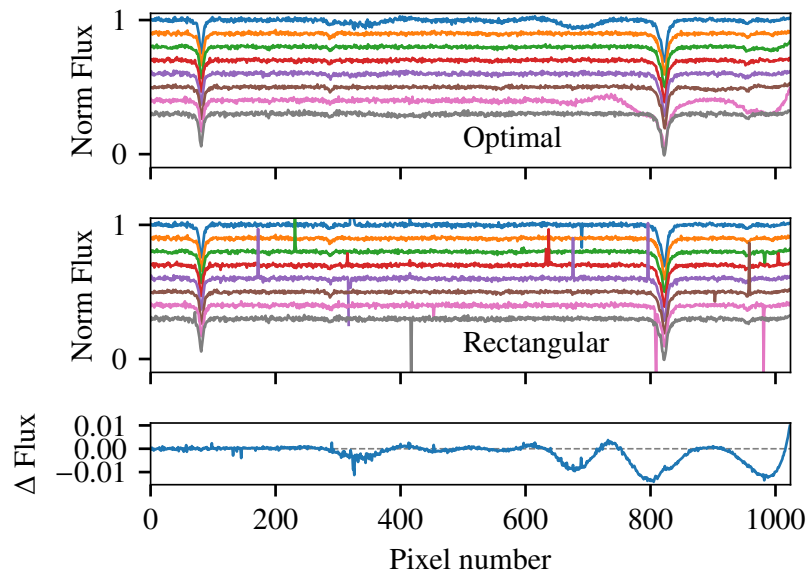


**Figure A.6:** Same as Figure A.1 but for the second detector of the second observation of HD 211847. In this example two large spikes around 800 and 1000 in the 7th nod (pink) create large deviations in the optimally reduced spectra. A spike in the first nod (blue) around pixel 700 also causes a bump. There is also some extra noise in the first nod around pixel 350.

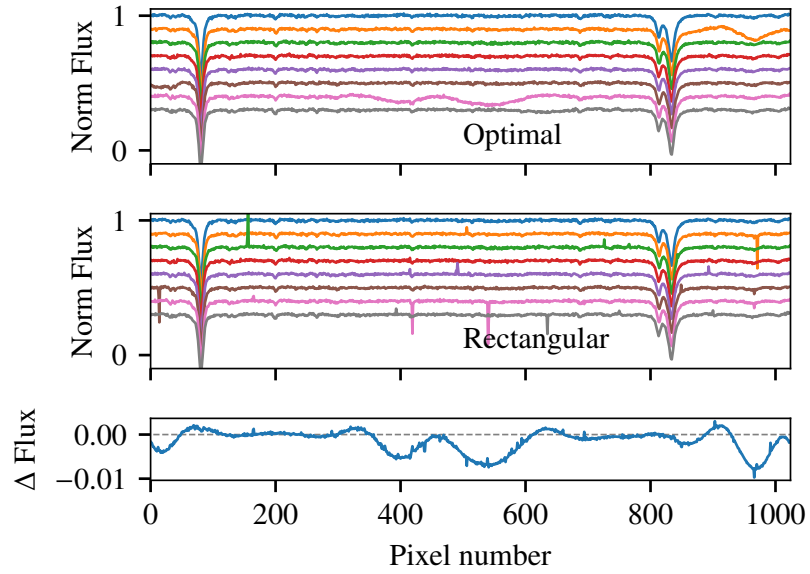
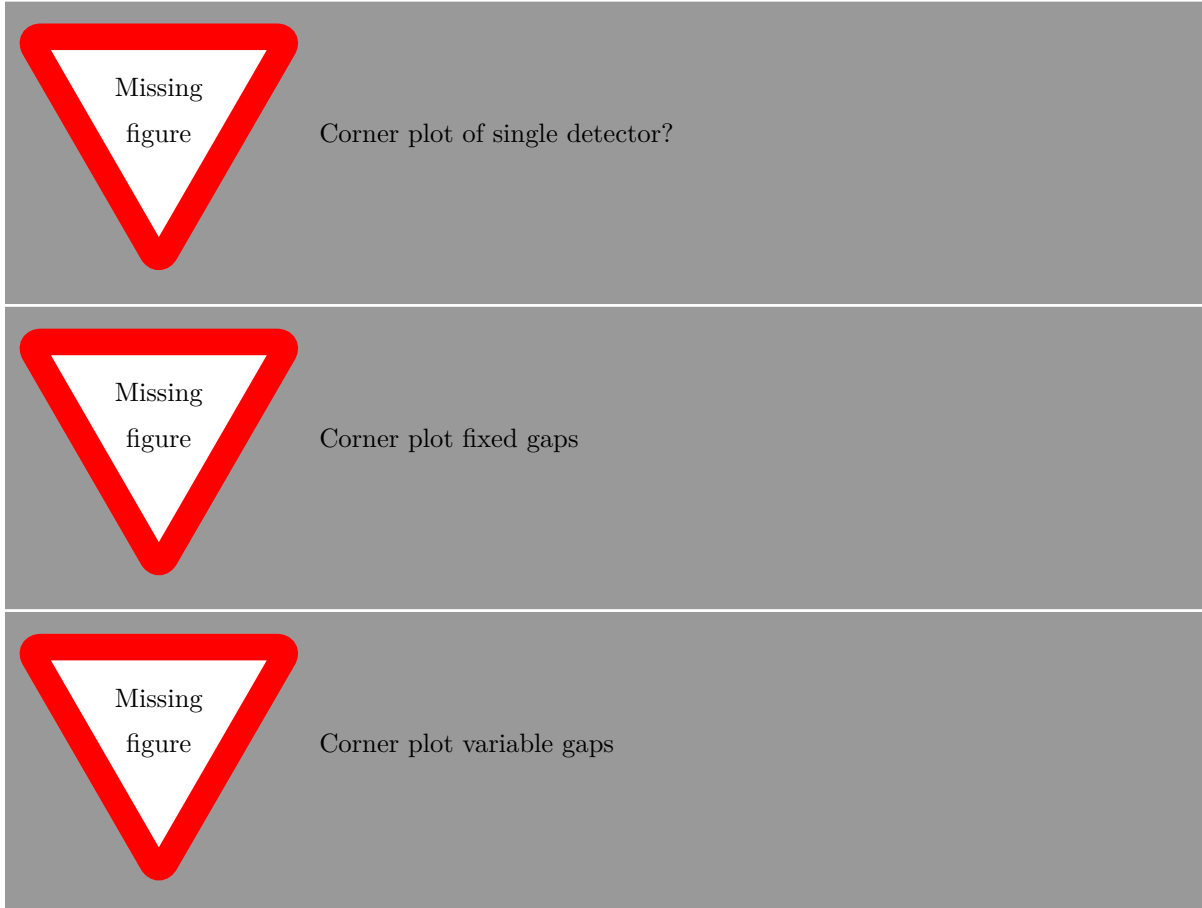


**Figure A.7:** Same as Figure A.1 but for the second detector of the second observation of HD 30501. In this example there are artefact causing spikes in four places. The second nod (orange) around pixel 950, the 6th nod (brown) around pixel 20 and two spikes in the 7th nod (pink) around pixels 400 and 550.

# Appendix B

## Multi-detector wavelength calibration

In this Appendix we provide an example of multi-detector wavelength calibration. To try and improve the wavelength calibration on detectors in which limited number of telluric lines fall.



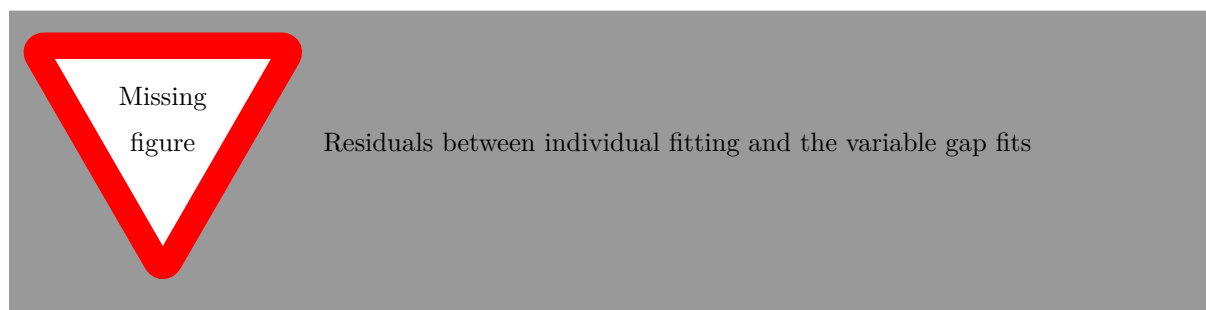
This example does not take the 2d position of the spectrum along the detector or any detector miss-alignments

Table B.1 shows the parameters obtained as well as fit statistics for quadratic and cubic fitting. BIC shows that

[remove vertical lines](#)  
[fill in table](#)

**Table B.1:** Example fitting parameters obtained for HD30501 observation 2 under different scenarios.

	Individual Detectors								Combined		
	#1	#2	#3	#4	Fixed Gaps		Variable Gaps				
a3 (u)	-	1e-4	-	-	-	-	-	-	-	-	blah
a2 (q)											blah
a1 (m)											blah
a0 (b)	2111	2111	2111	2111	2111	2111	2111	2111	2111	2111	blah
Gap1								1367	1367		x
Gap2								2700	2700		x
Gap3								3900	3900		x
$\chi^2$											blah
BIC	-234	-234	-234	-234	-234	-234		-234	-234	-234	blah



## PhD output

This section lists the activities in which I have been involved over the duration of my doctoral training.

In summary, over the duration of my doctoral training:

- I authored 1 first author articles – of which zero got accepted cite and another is currently undergoing the reviewing process cite. Fix up at end
- I also got involved as a co-author in 5 more articles (Figueira et al., 2016; Barros et al., 2017; Santerne et al., 2018; Lillo-Box et al., 2018; Ulmer-Moll et al., 2018),
- I also had the opportunity to attend 1 international conferences, 2 international schools and 1 national conference, in which I presented 1 oral contribution 1 poster.
- I tutored at the 11<sup>th</sup>, 12<sup>th</sup>, and 13<sup>th</sup> edition of the Physics Summer School from the Faculty of Science of the University of Porto.
- I was invited to be a proofreader for an outreach book Figueira and Neves (2015).
- I also gained experience as an observer, with 1 observing run.

I now proceed to list all the above in detail.

## C.1 Publications

A&A 586, A101 (2016)  
 DOI: 10.1051/0004-6361/201526900  
 © ESO 2016

**Astronomy  
 &  
 Astrophysics**

### Radial velocity information content of M dwarf spectra in the near-infrared

P. Figueira<sup>1</sup>, V. Zh. Adibekyan<sup>1</sup>, M. Oshagh<sup>1</sup>, J. J. Neal<sup>1,2</sup>, B. Rojas-Ayala<sup>1</sup>, C. Lovis<sup>3</sup>, C. Melo<sup>4</sup>, F. Pepe<sup>3</sup>, N. C. Santos<sup>1,2</sup>, and M. Tsantaki<sup>1</sup>

<sup>1</sup> Instituto de Astrofísica e Ciências do Espaço, Universidade do Porto, CAUP, Rua das Estrelas, 4150-762 Porto, Portugal  
 e-mail: pedro.figueira@astro.up.pt

<sup>2</sup> Departamento de Física e Astronomia, Faculdade de Ciências, Universidade do Porto, Portugal

<sup>3</sup> Observatoire Astronomique de l'Université de Genève, 51 Ch. des Maillettes, – Sauverny – 1290 Versoix, Suisse

<sup>4</sup> European Southern Observatory, Alonso de Córdova 3107, Vitacura, Casilla 19001, Santiago 19, Chile

Received 6 July 2015 / Accepted 16 October 2015

#### ABSTRACT

**Aims.** We evaluate the radial velocity (RV) information content and achievable precision on M0–M9 spectra covering the ZYJHK bands. We do so while considering both a perfect atmospheric transmission correction and discarding areas polluted by deep telluric features, as done in previous works.

**Methods.** To simulate the M-dwarf spectra, PHOENIX-ACES model spectra were employed; they were convolved with rotational kernels and instrumental profiles to reproduce stars with a  $v \sin i$  of 1.0, 5.0, and 10.0 km s<sup>-1</sup> when observed at resolutions of 60 000, 80 000, and 100 000. We considered the RV precision as calculated on the whole spectra, after discarding strongly polluted areas, and after applying a perfect telluric correction. In the latter option, we took into account the reduction in the number of recorded photons due to a transmittance lower than unity and considered its effect on the noise of the recorded spectra. In our simulations we paid particular attention to the details of the convolution and sampling of the spectra, and we discuss their impact on the final spectra.

**Results.** Our simulations show that the most important parameter ruling the difference in attainable precision between the considered bands is the spectral type. For M0–M3 stars, the bands that deliver the most precise RV measurements are the Z, Y, and H band, with relative merits depending on the parameters of the simulation. For M6–M9 stars, the bands show a difference in precision that is within a factor of ~2 and does not clearly depend on the band; this difference is reduced to a factor smaller than ~1.5 if we consider a non-rotating star seen at high resolution. We also show that an M6–M9 spectrum will deliver a precision about two times better as an M0–M3 spectra with the same signal-to-noise ratio. Finally, we note that the details of modeling the Earth atmosphere and interpreting the results have a significant impact on which wavelength regions are discarded when setting a limit threshold at 2–3%. The resolution element sampling on the observed spectra plays an important role in the atmospheric transmission characterization. As a result of the multiparameter nature of the problem, it is very difficult to precisely quantify the impact of absorption by the telluric lines on the RV precision, but it is an important limiting factor to the achievable RV precision.

**Key words.** techniques: radial velocities – instrumentation: spectrographs – methods: data analysis – stars: low-mass

#### 1. Introduction

The technique of spectroscopy is central to the study of stars and has allowed astronomy to gather a significant body of knowledge from the few photons a star provides us. During the past 20 years, spectroscopy was extensively applied in an emerging field in astronomy: the study of extrasolar planets. Following the discovery of 51 Peg b in 1995 (Mayor & Queloz 1995), more than 1900 planets were discovered, with masses and radii down to those of Earth (e.g., Dumusque et al. 2012; Barclay et al. 2013; Pepe et al. 2013). The radial velocity (RV) technique, with which the very first planet around a solar-type star was found, is still one of the most widely used detection methods; it is the main contributor to our knowledge of the mass of known exoplanets. The hunt for the exoplanet with the lowest mass pushed the RV precision down to the subm/s domain and motivated the construction of instruments such as ESPRESSO, which aims at a precision of 10 cm/s (Mégevand et al. 2012; Pepe et al. 2014b).

The RV signature of a planet scales with the mass of the star with  $M_*^{-2/3}$  and with the planetary orbital period with  $P_{\text{orb}}^{-1/3}$ . For an Earth-mass planet orbiting inside the habitable zone around a solar-type star, the RV amplitude is 10 cm/s, while for a planet with the same characteristics but orbiting an M7 dwarf, the RV amplitude is larger than 1 m/s. This is due to both a lower host mass and a closer habitable zone (a consequence of the lower luminosity output of these hosts). This relatively high amplitude contributed to an increased interest in the search for exoplanets around the low-mass M-dwarf (0.5–0.08  $M_\odot$ ) and led to the first estimates of the fraction of M dwarfs hosting Earth-mass planets inside the habitable zone (Bonfils et al. 2013). The intrinsic faintness of the stars in the visible domain limited these surveys to the brightest one hundred stars of our neighborhood and, along with activity, photon noise contribution to the noise budget proved to be the limiting factor. Spurred by the abundance of exoplanets, the exoplanet hunters did not rest in their efforts, and in the last several years, a new research direction

## Precise masses for the transiting planetary system HD 106315 with HARPS $\star$

S. C. C. Barros<sup>1,2\*</sup>, H. Gosselin<sup>2,23</sup>, J. Lillo-Box<sup>3</sup>, D. Bayliss<sup>4</sup>, E. Delgado Mena<sup>1</sup>, B. Brugger<sup>2</sup>, A. Santerne<sup>2</sup>, D. J. Armstrong<sup>5</sup>, V. Adibekyan<sup>1</sup>, J. D. Armstrong<sup>6</sup>, D. Barrado<sup>7</sup>, J. Bento<sup>8</sup>, I. Boisse<sup>2</sup>, A. S. Bonomo<sup>9</sup>, F. Bouchy<sup>4</sup>, D. J. A. Brown<sup>5</sup>, W. D. Cochran<sup>10</sup>, A. Collier Cameron<sup>11</sup>, M. Deleuil<sup>2</sup>, O. Demangeon<sup>1</sup>, R. F. Diaz<sup>4,12,13</sup>, A. Doyle<sup>5</sup>, X. Dumusque<sup>4</sup>, D. Ehrenreich<sup>4</sup>, N. Espinoza<sup>14,15</sup>, F. Faedi<sup>5</sup>, J. P. Faria<sup>1,16</sup>, P. Figueira<sup>1</sup>, E. Foxell<sup>5</sup>, G. Hébrard<sup>17,18</sup>, S. Hojjatpanah<sup>1,16</sup>, J. Jackman<sup>5</sup>, M. Lendl<sup>19</sup>, R. Ligi<sup>2</sup>, C. Lovis<sup>4</sup>, C. Melo<sup>3</sup>, O. Mousis<sup>2</sup>, J. J. Neal<sup>1,16</sup>, H. P. Osborn<sup>5</sup>, D. Pollacco<sup>5</sup>, N. C. Santos<sup>1,16</sup>, R. Sefako<sup>20</sup>, A. Shporer<sup>21</sup>, S. G. Sousa<sup>1</sup>, A. H. M. J. Triaud<sup>22</sup>, S. Udry<sup>4</sup>, A. Vigan<sup>2</sup>, and A. Wyttenbach<sup>4</sup>

<sup>1</sup> Instituto de Astrofísica e Ciências do Espaço, Universidade do Porto, CAUP, Rua das Estrelas, PT4150-762 Porto, Portugal e-mail: susana.barros@astro.up.pt

<sup>2</sup> Aix Marseille Univ, CNRS, LAM, Laboratoire d'Astrophysique de Marseille, Marseille, France

<sup>3</sup> European Southern Observatory (ESO), Alonso de Cordova 3107, Vitacura, Casilla 19001, Santiago de Chile, Chile

<sup>4</sup> Observatoire Astronomique de l'Université de Genève, 51 Chemin des Maillettes, 1290 Versoix, Switzerland

<sup>5</sup> Department of Physics, University of Warwick, Gibbet Hill Road, Coventry, CV4 7AL, UK

<sup>6</sup> Institute for Astronomy, University of Hawaii, 34 Ohia Ku Street, Pukalani, Maui, Hawaii 96790

<sup>7</sup> Depto. de Astrofísica, Centro de Astrobiología (CSIC-INTA), ESAC campus 28692 Villanueva de la Cañada (Madrid), Spain

<sup>8</sup> Research School of Astronomy and Astrophysics, Australian National University, Mount Stromlo Observatory, Cotter Road, Weston Creek, ACT 2611, Australia

<sup>9</sup> INAF – Osservatorio Astrofisico di Torino, Strada Osservatorio 20, I-10025, Pino Torinese (TO), Italy

<sup>10</sup> McDonald Observatory and Department of Astronomy, The University of Texas at Austin, Austin Texas USA

<sup>11</sup> Centre for Exoplanet Science, SUPA School of Physics & Astronomy, University of St Andrews, North Haugh ST ANDREWS, Fife, KY16 9SS

<sup>12</sup> Universidad de Buenos Aires, Facultad de Ciencias Exactas y Naturales, Buenos Aires, Argentina

<sup>13</sup> CONICET - Universidad de Buenos Aires, Instituto de Astronomía y Física del Espacio (IAFE), Buenos Aires, Argentina.

<sup>14</sup> Instituto de Astrofísica, Facultad de Física, Pontificia Universidad Católica de Chile, Av. Vicuña Mackenna 4860, 782-0436 Macul, Santiago, Chile

<sup>15</sup> Millennium Institute of Astrophysics, Av. Vicuña Mackenna 4860, 782-0436 Macul, Santiago, Chile

<sup>16</sup> Departamento de Física e Astronomia, Faculdade de Ciências, Universidade do Porto, Rua Campo Alegre, 4169-007 Porto, Portugal

<sup>17</sup> Institut d'Astrophysique de Paris, UMR7095 CNRS, Université Pierre & Marie Curie, 98bis boulevard Arago, 75014 Paris, France

<sup>18</sup> Aix Marseille Univ, CNRS, OHP, Observatoire de Haute Provence, Saint Michel l'Observatoire, France

<sup>19</sup> Space Research Institute, Austrian Academy of Sciences, Schmiedlstr. 6, 8042, Graz, Austria

<sup>20</sup> South African Astronomical Observatory, PO Box 9, Observatory, 7935

<sup>21</sup> Division of Geological and Planetary Sciences, California Institute of Technology, Pasadena, CA 91125, USA

<sup>22</sup> Institute of Astronomy, University of Cambridge, Madingley Road, CB3 0HA, Cambridge, United Kingdom

<sup>23</sup> Université de Toulouse, UPS-OMP, IRAP, Toulouse, France

Received ??, ??; accepted ??

### ABSTRACT

**Context.** The multi-planetary system HD 106315 was recently found in K2 data. The planets have periods of  $P_b \sim 9.55$  and  $P_c \sim 21.06$  days, and radii of  $r_b = 2.44 \pm 0.17 R_\oplus$  and  $r_c = 4.35 \pm 0.23 R_\oplus$ . The brightness of the host star ( $V=9.0$  mag) makes it an excellent target for transmission spectroscopy. However, to interpret transmission spectra it is crucial to measure the planetary masses.

**Aims.** We obtained high successional radial velocities for HD 106315 to determine the mass of the two transiting planets discovered with Kepler K2. Our successful observation strategy was carefully tailored to mitigate the effect of stellar variability.

**Methods.** We modelled the new radial velocity data together with the K2 transit photometry and a new ground-based partial transit of HD 106315c to derive system parameters.

**Results.** We estimate the mass of HD 106315b to be  $12.6 \pm 3.2 M_\oplus$  and the density to be  $4.7 \pm 1.7 g cm^{-3}$ , while for HD 106315c we estimate a mass of  $15.2 \pm 3.7 M_\oplus$  and a density of  $1.01 \pm 0.29 g cm^{-3}$ . Hence, despite planet c having a radius almost twice as large as planet b, their masses are consistent with one another.

**Conclusions.** We conclude that HD 106315c has a thick hydrogen-helium gaseous envelope. A detailed investigation of HD 106315b using a planetary interior model constrains the core mass fraction to be 5–29%, and the water mass fraction to be 10–50%. An alternative, not considered by our model, is that HD 106315b is composed of a large rocky core with a thick H-He envelope. Transmission spectroscopy of these planets will give insight into their atmospheric compositions and also help constrain their core compositions.

**Key words.** planetary systems: detection – planetary systems: fundamental parameters – planetary systems: composition— stars: individual HD 106315, EPIC 201437844 – techniques: photometric – techniques: radial velocities

## An Earth-sized exoplanet with a Mercury-like composition

A. Santerne<sup>1</sup>, B. Brugger<sup>1</sup>, D. J. Armstrong<sup>2</sup>, V. Adibekyan<sup>3</sup>, J. Lillo-Box<sup>4</sup>, H. Gosselin<sup>1,5</sup>, A. Aguichine<sup>1,6</sup>, J.-M. Almenara<sup>7</sup>, D. Barrado<sup>8</sup>, S. C. C. Barros<sup>3</sup>, D. Bayliss<sup>7</sup>, I. Boisse<sup>1</sup>, A. S. Bonomo<sup>9</sup>, F. Bouchy<sup>7</sup>, D. J. A. Brown<sup>2</sup>, M. Deleuil<sup>1</sup>, E. Delgado Mena<sup>3</sup>, O. Demangeon<sup>3</sup>, R. F. Díaz<sup>10,11,7</sup>, A. Doyle<sup>2</sup>, X. Dumusque<sup>7</sup>, F. Faedi<sup>2,12</sup>, J. P. Faria<sup>3,13</sup>, P. Figueira<sup>4,3</sup>, E. Foxell<sup>2</sup>, H. Giles<sup>7</sup>, G. Hébrard<sup>14,15</sup>, S. Hojjatpanah<sup>3,13</sup>, M. Hobson<sup>1</sup>, J. Jackman<sup>2</sup>, G. King<sup>2</sup>, J. Kirk<sup>2</sup>, K. W. F. Lam<sup>2</sup>, R. Ligi<sup>1</sup>, C. Lovis<sup>7</sup>, T. Louden<sup>2</sup>, J. McCormac<sup>2</sup>, O. Mousis<sup>1</sup>, J. J. Neal<sup>3,13</sup>, H. P. Osborn<sup>2,1</sup>, F. Pepe<sup>7</sup>, D. Pollacco<sup>2</sup>, N. C. Santos<sup>3,13</sup>, S. G. Sousa<sup>3</sup>, S. Udry<sup>7</sup> & A. Vigan<sup>1</sup>

<sup>1</sup>*Aix Marseille Univ, CNRS, CNES, LAM, Marseille, France*

<sup>2</sup>*Department of Physics, University of Warwick, Gibbet Hill Road, Coventry, CV4 7AL, UK*

<sup>3</sup>*Instituto de Astrofísica e Ciências do Espaço, Universidade do Porto, CAUP, Rua das Estrelas, 4150-762 Porto, Portugal*

<sup>4</sup>*European Southern Observatory (ESO), Alonso de Cordova 3107, Vitacura, Casilla 19001, Santiago de Chile, Chile*

<sup>5</sup>*Université de Toulouse, UPS-OMP, IRAP, Toulouse, France*

<sup>6</sup>*Paris-Saclay Université, ENS Cachan, 61 av. du Président Wilson, 94230 Cachan, France*

<sup>7</sup>*Observatoire Astronomique de l'Université de Genève, 51 Chemin des Maillettes, 1290 Versoix, Switzerland*

<sup>8</sup>*Dept. de Astrofísica, Centro de Astrobiología (CSIC-INTA), ESAC campus 28692 Villanueva de la Cañada (Madrid), Spain*

<sup>9</sup>*INAF – Osservatorio Astrofisico di Torino, Strada Osservatorio 20, I-10025, Pino Torinese (TO), Italy*

<sup>10</sup>*Universidad de Buenos Aires, Facultad de Ciencias Exactas y Naturales. Buenos Aires, Argentina*

<sup>11</sup>*CONICET - Universidad de Buenos Aires. Instituto de Astronomía y Física del Espacio (IAFE). Buenos Aires, Argentina*

<sup>12</sup>*INAF – Osservatorio Atrofisico di Catania, via S. Sofia 78, 95123, Catania, Italy*

<sup>13</sup>*Departamento de Física e Astronomia, Faculdade de Ciencias, Universidade do Porto, Rua Campo Alegre, 4169-007 Porto, Portugal*

<sup>14</sup>*Institut d’Astrophysique de Paris, UMR7095 CNRS, Universite Pierre & Marie Curie, 98bis boulevard Arago, 75014 Paris, France*

<sup>15</sup>*Aix Marseille Univ, CNRS, OHP, Observatoire de Haute Provence, Saint Michel l’Observatoire, France*

The Earth, Venus, Mars, and some extrasolar terrestrial planets<sup>1</sup> have a mass and radius that is consistent with a mass fraction of about 30% metallic core and 70% silicate mantle<sup>2</sup>. At the inner frontier of the solar system, Mercury has a completely different composition, with a mass fraction of about 70% metallic core and 30% silicate mantle<sup>3</sup>. Several formation or evolution scenarios are proposed to explain this metal-rich composition, such as a

## The *TROY* project: II. Multi-technique constraints on exotrojans in nine planetary systems ★,★★,★★★

J. Lillo-Box<sup>1</sup>, A. Leleu<sup>2</sup>, H. Parviainen<sup>3,4,5</sup>, P. Figueira<sup>1,6</sup>, M. Mallonn<sup>7</sup>, A.C.M. Correia<sup>8,9,10</sup>, N.C. Santos<sup>6,11</sup>, P. Robutel<sup>8</sup>, M. Lendl<sup>12</sup>, H.M.J. Boffin<sup>13</sup>, J.P. Faria<sup>6,11</sup>, D. Barrado<sup>14</sup>, J. Neal<sup>6,11</sup>

<sup>1</sup> European Southern Observatory (ESO), Alonso de Cordova 3107, Vitacura Casilla 19001, Santiago 19, Chile  
 e-mail: jllollobo@eso.org

<sup>2</sup> Physics Institute, Space Research and Planetary Sciences, Center for Space and Habitability - NCCR PlanetS, University of Bern, Bern, Switzerland

<sup>3</sup> Instituto de Astrofísica de Canarias (IAC), E-38200 La Laguna, Tenerife, Spain

<sup>4</sup> Dept. Astrofísica, Universidad de La Laguna (ULL), E-38206 La Laguna, Tenerife, Spain

<sup>5</sup> Sub-department of Astrophysics, Department of Physics, University of Oxford, Oxford, OX1 3RH, UK

<sup>6</sup> Instituto de Astrofísica e Ciências do Espaço, Universidade do Porto, CAUP, Rua das Estrelas, PT4150-762 Porto, Portugal

<sup>7</sup> Leibniz-Institut für Astrophysik Potsdam, An der Sternwarte 16, D-14482 Potsdam, Germany

<sup>8</sup> IMCCE, Observatoire de Paris - PSL Research University, UPMC Univ. Paris 06, Univ. Lille 1, CNRS, 77 Avenue Denfert-Rochereau, 75014 Paris, France

<sup>9</sup> Department of Physics, University of Coimbra, 3004-516 Coimbra, Portugal

<sup>10</sup> CIDMA, Departamento de Física, Universidade de Aveiro, Campus de Santiago, 3810-193 Aveiro, Portugal

<sup>11</sup> Departamento de Física e Astronomia, Faculdade de Ciências, Universidade do Porto, Portugal

<sup>12</sup> Space Research Institute, Austrian Academy of Sciences, Schmiedlstr. 6, 8042 Graz, Austria

<sup>13</sup> ESO, Karl Schwarzschild Strasse 2, 85748 Garching, Germany

<sup>14</sup> Depto. de Astrofísica, Centro de Astrobiología (CSIC-INTA), ESAC campus 28692 Villanueva de la Cañada (Madrid), Spain

In preparation

### ABSTRACT

**Context.** Co-orbital bodies are the byproduct of planet formation and evolution, as we know from the Solar System. Although planet-size co-orbitals do not exist in our planetary system, dynamical studies show that they can remain stable for long periods of time in the gravitational well of massive planets. Should they exist, their detection is feasible with the current instrumentation.

**Aims.** In this paper, we present new ground-based observations searching for these bodies co-orbiting with nine close-in ( $P < 5$  days) planets, using different observing techniques. The combination of all of them allows us to restrict the parameter space of any possible trojan in the system.

**Methods.** We use multi-technique observations (radial velocity, precision photometry and transit timing variations), both newly acquired in the context of the *TROY* project and publicly available, to constrain the presence of planet-size trojans in the Lagrangian points of nine known exoplanets.

**Results.** We find no clear evidence of trojans in these nine systems through any of the techniques used down to the precision of the observations. However, this allows us to constrain the presence of any potential trojan in the system, specially in the trojan mass/radius versus libration amplitude plane. In particular, we can set upper mass limits in the super-Earth mass regime for six of the studied systems.

**Key words.** Planets and satellites: gaseous planets, fundamental parameters; Techniques: radial velocity, transits; Minor planets, asteroids: general

### 1. Introduction

The development of state-of-the-art instrumentation and space-based facilities in the past decades boosted the discovery of extrasolar planets up to several thousands of detections<sup>1</sup>. This

plethora has shown the wide diversity of intrinsic and orbital properties that planets can have. Exoplanet research is currently focused on the deep understanding of the planet composition, structure and atmosphere, in parallel to the search for Earth analogues. From our own system, we know that extrasolar systems should also host other components that also played an important role in moulding the architecture and properties of the planets. In the Solar System, moons and more recently trojans (e.g., Lucy mission, Levison et al. 2017) are targets for *in situ* exploration since they contain clues on the formation and early evolution of our planetary system (e.g., Morbidelli et al. 2005; Borisov et al. 2017).

Trojan bodies co-rotate with planets in a wide variety of orbital configurations, mainly in tadpole (orbiting the gravity

\* Based on observations collected at the Centro Astronómico Hispano Alemán (CAHA) at Calar Alto, operated jointly by the Max-Planck Institut für Astronomie and the Instituto de Astrofísica de Andalucía (CSIC).

\*\* Partly based on data obtained with the STELLA robotic telescopes in Tenerife, an AIP facility jointly operated by AIP and IAC.

\*\*\* Based on observations collected at the European Organisation for Astronomical Research in the Southern Hemisphere under ESO programmes 297.C-5051, 098.C-0440(A), and 298.C-5009

<sup>1</sup> <http://exoplanet.eu>

## C.2 Talks and Seminars

TALK

### Towards exoplanetary atmospheres: new data reduction techniques for the nIR.

**Location:** XXVI Encontro Nacional de Astronomia e Astrofísica (ENAA), Aveiro, Portugal    **Date:** 2016, Sept. 09  
**File:** <http://gravitation.web.ua.pt/enaa2016/index2a62.html?q=node/3>

**Abstract:**

Exoplanetary atmospheres are one of the forefronts of exoplanet science. The measurement of exoplanet atmospheres can help break degeneracies in the mass-radius relationship for solid exoplanets allowing proper derivation of the planets properties, and may provide important clues to the origin and evolution of planets. The technological breakthrough of high-resolution spectrographs ( $\Delta\lambda/\lambda = 100,000$ ) allow for the separation and wavelength tracking of individual molecular spectral features. This allows for the separation of the stationary telluric absorption lines from the moving planet-star spectral lines. We focus our initial investigation on extracting the atmospheric signal of brown dwarfs, which are interesting objects between giant planets and small stars. Brown dwarf targets are good candidates to begin our investigation as their larger mass induces larger radial velocity shifts to the atmospheric lines and their larger radius (and surface area) produce a stronger signal compared to smaller planets. In this talk I will discuss the ongoing work of my PhD towards extracting the signal of brown dwarf atmospheres from high-resolution nIRspectra. I will discuss the methodology and techniques developed towards extracting the spectral lines of the atmospheres and show some of our current results.

### C.3 Posters

POSTER

#### Towards Exoplanet Atmospheres: new data reduction for the nIR

**Location:** *IVth Azores International Advanced School in Space Sciences*, Horta, Faial, Azores Islands, Portugal

**Date:** 2014, July 17–27

**Abstract:**

In this poster I outline the goal of the direct subtraction technique, detailing the data preparation and correct steps needed. It shows the first results of applying the direct subtraction on our observations. The poster is provided on the next page.

POSTER

#### Towards Exoplanet Atmospheres: new data reduction for the nIR

**Location:** *XXVI Encontro Nacional de Astronomia e Astrofísica (ENAA)*, Aveiro, Portugal

**Date:** 2016, Sept. 09

**File:**

<http://gravitation.web.ua.pt/enaa2016/index2a62.html?q=node/3>

**Abstract:**

I presented the same poster at ENAA as I did at the IVth Azores International Advanced School in Space Sciences.



# Towards Exoplanet Atmospheres: new data reduction for the nIR

Jason J. Neal, P. Figueira, N. C. Santos, C. H. F. Melo

## 1) Objective

- Reduce near-Infrared CRIRES spectra with high fidelity
- Extract spectra of exoplanetary atmospheres

## 2) Methods

- CRIRES reduction with in-house IRAF pipeline: Data Reduction Algorithm for CRIRES Spectra (DRACS).
- Obtain models of atmospheric absorption spectra from TAPAS web-service [Bertaux *et al.* 2014, A&A, 564, A96].

$$I_{tell}(\lambda) = 1 - \sum_{j=1}^m \text{Telluric lines} \quad (1)$$

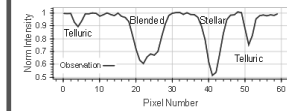
- Wavelength calibrate the observations using the telluric absorption spectrum imprinted by the atmosphere.

$$I_{obs}(pix) = 1 - \left( \sum_{j=1}^m \text{Telluric} \times \sum_{k=1}^n \text{Stellar} \right) \quad (2)$$

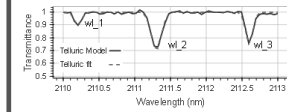
- Correct observations for telluric absorption by dividing by the same TAPAS telluric absorption models.
- Correct for Earth's barycentric motion then subtract two observations to cancel out the stellar absorption lines.

## 3) Calibration

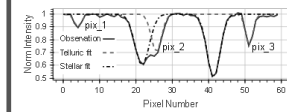
Simulated observation of 2 stellar and 3 telluric lines



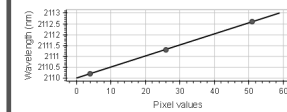
Fit Eq. 1 to telluric model to obtain the line centers in wavelength space ( $wl_i$ ).



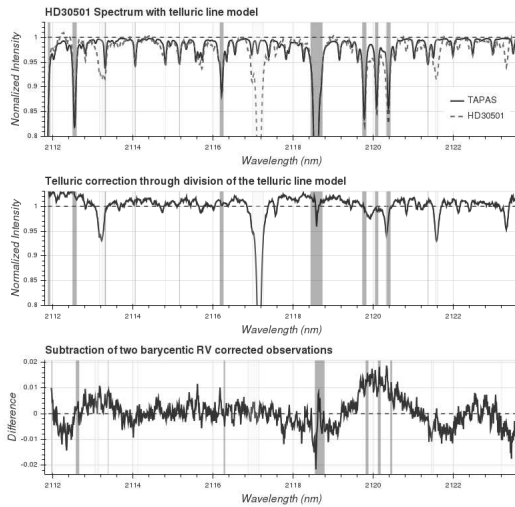
Fit Eq. 2 to the observation to obtain the telluric line centers in pixel space ( $pix_i$ ).



A second order polynomial is applied to the fitted gaussian line centers  $wl_i$  and  $pix_i$ .



## 4) Results



## 5) Future Work

- Model and extract the exoplanetary lines in the subtracted spectra.
- Apply these tools to 7 stars that host brown dwarf companions.



## C.4 Attended Conferences and Schools

### CONFERENCE

#### Towards Other Earths II:The star-planet connection

**Location:** Porto, Portugal

**Date:** 2014, Sept. 15–19

**Website** <http://www.astro.up.pt/investigacao/conferencias/toe2014/>

##### Description:

The study of extrasolar planets is one of the most active areas of research of modern astronomy. The number of discoveries attests for the importance of a topic that reaches out and captivates the imagination of scientists and public alike. This conference aims at reviewing the state of the art of star-planet connection, with some focus on the detection and characterization of Earth like planets orbiting other stars. We propose to debate how the field of extrasolar planets will evolve in respect to this and how it will face the challenges of the upcoming years.

### CONFERENCE

#### I Vietri Advanced School on Exoplanetary Science

**Location:** 2015, May 25–29

**Date:** Vietri sul Mare  
(Salerno), Italy

**Website** <http://www.iiassvietri.it/en/asex2015.html>

##### Description:

The School is aimed to provide a comprehensive, state-of-the-art picture of a variety of relevant aspects of the fast-developing, highly interdisciplinary field of extrasolar planets research. The Lecture topics of the 1st year of School will be focused on exoplanet detection with the Radial Velocity, Photometric Transits, Gravitational Microlensing, and Direct Imaging techniques. The Lectures will be delivered by four senior researchers to an audience of graduate students, Ph.D. students and young post-docs.

## IVth Azores International Advanced School in Space Sciences

**Location:** 2016, July 17–27

**Date:** Horta, Faial, Azores Islands, Portugal

**Website** <http://www.iastro.pt/research/conferences/faial2016/>

### Description:

This International Advanced School addresses the topics at the forefront of scientific research being conducted in the fields of stellar physics and exoplanetary science. It is mainly aimed at PhD and MSc students (although postdocs are also encouraged to apply) in any field of Astrophysics.

Students will be given the opportunity to present their own research work by bringing a poster to the School. The School provides an opportunity for the young researchers to network with fellow students and lecturers, thereby promoting awareness of areas outside the main specialization of the student, and potential cross-fertilization of techniques and concepts.

The School covers two scientific topics that share many synergies and resources: Asteroseismology and Exoplanets. Therefore, the program aims at building opportunities for cooperation and sharing of methods that will benefit both communities. This cooperation has experienced great success in the context of past space missions such as CoRoT and Kepler. Upcoming photometry and astrometry from space, as well as complementary data from ground-based networks, will continue to foster this cooperation. Observations of bright stars and clusters in the ecliptic plane are being made by the repurposed K2 mission, and NASA's TESS and ESA's CHEOPS missions will soon start obtaining similar data over the entire sky. ESA's PLATO mission will then build upon these successes by providing photometric light curves on a wealth of stars. Ground-based spectroscopy from the Stellar Observations Network Group (SONG) will complement the satellite data for the brightest stars in the sky, as will also be the case with the new generation of high-precision spectrographs being developed for the ESO, like the Echelle SPectrograph for Rocky Exoplanets and Stable Spectroscopic Observations (ESPRESSO).

## XXVI Encontro Nacional de Astronomia e Astrofísica

**Location:** Aveiro, Portugal

**Date:** 2016, Sept. 08–09

**File:** <http://gravitation.web.ua.pt/enaa2016/index2a62.html?q=node/3>

### Abstract:

The main goal of this national meeting is to present a general overview of the international state of the art research done in Astronomy and Astrophysics. ENAA also allows for researchers to get together and discuss scientific ideas and policies, strengthen the collaboration between national researchers and integrate young researchers in the community through the presentation of their work.

## C.5 Outreach

### ROOF READING

#### Astro Homus

**Location:** 2015 May

**Date:** Porto, Portugal

**Website** <http://astrohomus.astro.up.pt/livro>

##### Description:

Was involved in proofreading the outreach book *Astro Homus* (Figueira and Neves, 2015) which highlights the people working in Astronomy.

## C.6 Other

TEACHING

### Monitor at the 11<sup>th</sup>, 12<sup>th</sup>, 13<sup>th</sup> Physics Summer School

**Location:** Faculty of Science, University of Porto, Portugal    **Date:** 2015–2017

**Website** <http://e-fisica.fc.up.pt/edicoes/>

**Description:**

Instructing and monitoring 4–5 secondary school students through activities related to planet detection and characterization. One week per year.

*Na sua Edição a Escola desafia os participantes com o programa mais radical de sempre com projectos envolvendo lasers, supercondutores, nanotecnologias, física espacial, fibras ópticas, biosensores e astrofísica. Projectos que abrangem as três grandes áreas de investigação do DFA, Física, Astronomia e Engenharia Física. Assim, se tens apetência pelo conhecimento e pelo processo de investigação que permite inquirir a Natureza e testar hipóteses acerca das causas das coisas, então deixa-te arrastar pelo encantamento da experimentação e do entendimento das ideias mais profundas e abrangentes. O DFA garante uma viagem através do Universo, do microcosmo ao macrocosmo, inserindo-te num projecto que te dilatará a imaginação. Tens coragem? Aparece!*

OBSERVING

### HARPS-N@Telescopio Nazionale Galileo observing run

**Location:** La Palma, Spain

**Date:** 2017 Feb. 6–8

**Website** N/A

**Description:**

Observing runs are an essential part of the training of any astronomer. During my PhD I had the opportunity to observe for 3 nights on HARPS-N. These were for the *TROY* project, which some IA-Porto researchers were collaborating. These observations were to fill in the phase curve of previously detected low-mass exoplanets to further constrain their masses. These observations were used in a recent publication Lillo-Box et al. (2018).

I hope to perform observations in Chile in early 2019 also.

# Bibliography

Adibekyan, V. Z., Sousa, S. G., Santos, N. C., Mena, E. D., Hernández, J. I. G., Israeliian, G., Mayor, M., and Khachatryan, G.: 2012, *Astronomy and Astrophysics* **545**, A32

Allard, F.: 2013, *Proceedings of the International Astronomical Union* **8**(S299), 271, 00007

Allard, F., Homeier, D., and Freytag, B.: 2010, *arXiv:1011.5405 [astro-ph]*, 00066

Andreasen, D. T., Sousa, S. G., Delgado Mena, E., Santos, N. C., Tsantaki, M., Rojas-Ayala, B., and Neves, V.: 2016, *Astronomy and Astrophysics* **585**, A143

Artigau, E., Kouach, D., Donati, J.-F., Doyon, R., Delfosse, X., Baratchart, S., Lacombe, M., Moutou, C., Rabou, P., Parès, L. P., Micheau, Y., Thibault, S., Reshetov, V. A., Dubois, B., Hernandez, O., Vallée, P., Wang, S.-Y., Dolon, F., Pepe, F. A., Bouchy, F., Striebig, N., Hénault, F., Loop, D., Saddlemeyer, L., Barrick, G., Vermeulen, T., Dupieux, M., Hébrard, G., Boisse, I., Martioli, E., Alencar, S. H. P., do Nascimento, J.-D., and Figueira, P.: 2014, in *Proc. SPIE*, Vol. 9147, p. 914715, International Society for Optics and Photonics, 00047

Artigau, E., Malo, L., Doyon, R., Figueira, P., Delfosse, X., and Astudillo-Defru, N.: 2018, *The Astronomical Journal* **155**, 198

Asplund, M., Grevesse, N., Sauval, A. J., and Scott, P.: 2009, *Annual Review of Astronomy and Astrophysics* **47**, 481

Astudillo-Defru, N., Bonfils, X., Delfosse, X., Ségransan, D., Forveille, T., Bouchy, F., Gillon, M., Lovis, C., Mayor, M., Neves, V., Pepe, F., Perrier, C., Queloz, D., Rojo, P., Santos, N. C., and Udry, S.: 2015, *Astronomy and Astrophysics* **575**, A119

Baraffe, I., Chabrier, G., Barman, T., Allard, F., and Hauschildt, P. H.: 2003, *Astronomy and Astrophysics* **402**(2), 701, 00000

Baraffe, I., Homeier, D., Allard, F., and Chabrier, G.: 2015, *Astronomy and Astrophysics* **577**, A42, 00280

Barnes, J. R., Barman, T. S., Jones, H. R. A., Leigh, C. J., Cameron, A. C., Barber, R. J., and Pinfield, D. J.: 2008, *Monthly Notices of the Royal Astronomical Society* **390**(3), 1258

- Barros, S. C. C., Gosselin, H., Lillo-Box, J., Bayliss, D., Mena, E. D., Brugger, B., Santerne, A., Armstrong, D. J., Adibekyan, V., Armstrong, J. D., Barrado, D., Bento, J., Boisse, I., Bonomo, A. S., Bouchy, F., Brown, D. J. A., Cochran, W. D., Cameron, A. C., Deleuil, M., Demangeon, O., Díaz, R. F., Doyle, A., Dumusque, X., Ehrenreich, D., Espinoza, N., Faedi, F., Faria, J. P., Figueira, P., Foxell, E., Hébrard, G., Hojjatpanah, S., Jackman, J., Lendl, M., Ligi, R., Lovis, C., Melo, C., Mousis, O., Neal, J. J., Osborn, H. P., Pollacco, D., Santos, N. C., Sefako, R., Shporer, A., Sousa, S. G., Triaud, A. H. M. J., Udry, S., Vigan, A., and Wyttenbach, A.: 2017, *Astronomy & Astrophysics* **608**, A25
- Bean, J. L., Miller-Ricci Kempton, E., and Homeier, D.: 2010, *Nature* **468**, 669, 00283
- Benedict, G. F. and Harrison, T. E.: 2017, *The Astronomical Journal* **153**, 258
- Bertaux, J. L., Lallement, R., Ferron, S., Boonne, C., and Bodichon, R.: 2014, *Astronomy and Astrophysics* **564**, A46, 00041
- Bevington, P. R. and Robinson, D. K.: 2003, *Data Reduction and Error Analysis for the Physical Sciences*, McGraw-Hill, p.g. 208-212
- Birkby, J. L., de Kok, R. J., Brogi, M., Schwarz, H., and Snellen, I. a. G.: 2017, *The Astronomical Journal* **153**(3), 138
- Bonfanti, A., Ortolani, S., and Nascimbeni, V.: 2016, *Astronomy and Astrophysics* **585**, A5
- Bouchy, F., Doyon, R., Artigau, E., Melo, C., Hernandez, O., Wildi, F., Delfosse, X., Lovis, C., Figueira, P., Canto Martins, B. L., González Hernández, J. I., Thibault, S., Reshetov, V., Pepe, F., Santos, N. C., de Medeiros, J. R., Rebolo, R., Abreu, M., Adibekyan, V. Z., Bandy, T., Benz, W., Blind, N., Bohlender, D., Boisse, I., Bovay, S., Broeg, C., Brouseau, D., Cabral, A., Chazelas, B., Cloutier, R., Coelho, J., Conod, U., Cumming, A., Delabre, B., Genolet, L., Hagelberg, J., Jayawardhana, R., Käufli, H.-U., Lafrenière, D., de Castro Leão, I., Malo, L., de Medeiros Martins, A., Matthews, J. M., Metchev, S., Oshagh, M., Ouellet, M., Parro, V. C., Rasilla Piñeiro, J. L., Santos, P., Sarajlic, M., Segovia, A., Sordet, M., Udry, S., Valencia, D., Vallée, P., Venn, K., Wade, G. A., and Saddlemyer, L.: 2017, *The Messenger* **169**, 21, 00000
- Bouchy, F., Pepe, F., and Queloz, D.: 2001, *Astronomy and Astrophysics* **374**(2), 733, 00258
- Brogi, M., de Kok, R. J., Albrecht, S., Snellen, I. A. G., Birkby, J. L., and Schwarz, H.: 2016, *The Astrophysical Journal* **817**(2), 106, 00000
- Brogi, M., de Kok, R. J., Birkby, J. L., Schwarz, H., and Snellen, I. A. G.: 2014, *Astronomy and Astrophysics* **565**, A124, 00000
- Brogi, M., Snellen, I. A. G., de Kok, R. J., Albrecht, S., Birkby, J., and de Mooij, E. J. W.: 2012, *Nature* **486**, 502, 00000
- Burrows, A., Marley, M., Hubbard, W. B., Lunine, J. I., Guillot, T., Saumon, D., Freedman, R., Sudarsky, D., and Sharp, C.: 1997, *The Astrophysical Journal* **491**, 856
- Chabrier, G. and Baraffe, I.: 2000, *Annual Review of Astronomy and Astrophysics* **38**(1), 337, 00483
- Chen, J. and Kipping, D. M.: 2016, *The Astrophysical Journal* **834**(1), 17

- Ciddor, P. E.: 1996, *Applied Optics* **35**(9), 1566
- Clough, S. A. and Iacono, M. J.: 1995, *Journal of Geophysical Research: Atmospheres* **100**(D8), 16519, 00002
- Collaboration, G., Brown, A. G. A., Vallenari, A., Prusti, T., Bruijne, D., J. J. H., Babusiaux, C., and Bailer-Jones, C. a. L.: 2018, *ArXiv e-prints* p. arXiv:1804.09365
- Connes, P.: 1985, *Astrophysics and Space Science* **110**(2), 211
- Connes, P., Martic, M., and Schmitt, J.: 1996, *Astrophysics and Space Science* **241**(1), 61
- Correia, A. C. M., Udry, S., Mayor, M., Laskar, J., Naef, D., Pepe, F., Queloz, D., and Santos, N. C.: 2005, *aap* **440**, 751, 00000
- Cotton, D. V., Bailey, J., and Kedziora-Chudczer, L.: 2014, *Monthly Notices of the Royal Astronomical Society* **439**, 387, 00007
- Crepp, J. R., Gonzales, E. J., Bechter, E. B., Montet, B. T., Johnson, J. A., Piskorz, D., Howard, A. W., and Isaacson, H.: 2016, *The Astrophysical Journal* **831**, 00004
- Czekala, I., Andrews, S. M., Mandel, K. S., Hogg, D. W., and Green, G. M.: 2015, *The Astrophysical Journal* **812**(2), 128, 00022
- Czesla, S., Molle, T., and Schmitt, J. H. M. M.: 2018, *Astronomy and Astrophysics* **609**, A39
- de Kok, R. J., Brogi, M., Snellen, I. A., Birkby, J., Albrecht, S., and de Mooij, E. J.: 2013, *Astronomy and Astrophysics* **554**, A82, 00086
- Deeg, H.: 1998, in *Brown Dwarfs and Extrasolar Planets*, Vol. 134 of *ASP Conference Series* #134, p. 216
- Dorn, R. J., Finger, G., Huster, G., Kaeufl, H.-U., Lizon, J.-L., Mehrgan, L., Meyer, M., Pirard, J.-F., Silber, A., Stegmeier, J., and Moorwood, A. F. M.: 2004, in *Optical and Infrared Detectors for Astronomy*, Vol. 5499, pp 510–518, International Society for Optics and Photonics
- Dorn, R. J., Follert, R., Bristow, P., Cumani, C., Eschbaumer, S., Grunhut, J., Haimerl, A., Hatzes, A., Heiter, U., and Hinterschuster, R.: 2016, in *Ground-Based and Airborne Instrumentation for Astronomy VI*, Vol. 9908, p. 99080I, International Society for Optics and Photonics, 00002
- Edlén, B.: 1953, *JOSA* **43**(5), 339
- ESO: 2017, *ESO Call for Proposals - P101*
- Ferluga, S., Floreano, L., Bravar, U., and Bédalo, C.: 1997, *Astronomy and Astrophysics Supplement Series* **121**(1), 201, 00012
- Figueira, P., Adibekyan, V. Z., Oshagh, M., Neal, J. J., Rojas-Ayala, B., Lovis, C., Melo, C., Pepe, F., Santos, N. C., and Tsantaki, M.: 2016, *Astronomy and Astrophysics* **586**, A101, 00002
- Figueira, P. and Neves, S.: 2015, *Astro Homus*, CAUP

- Figueira, P., Pepe, F., Melo, C. H. F., Santos, N. C., Lovis, C., Mayor, M., Queloz, D., Smette, A., and Udry, S.: 2010, *Astronomy and Astrophysics* **511**, A55, 00057
- Freudling, W., Romaniello, M., Bramich, D. M., Ballester, P., Forchi, V., García-Dabló, C. E., Moehler, S., and Neeser, M. J.: 2013, *Astronomy and Astrophysics* **559**, A96
- Gullikson, K., Dodson-Robinson, S., and Kraus, A.: 2014, *The Astronomical Journal* **148**(3), 53, 00015
- Hadrava, P.: 2009, *arXiv:0909.0172 [astro-ph]*, 00013
- Halbwachs, J.-L., Arenou, F., Mayor, M., Udry, S., and Queloz, D.: 2000, *Astronomy and Astrophysics* **355**, 581, 00198
- Hatzes, A. P. and Rauer, H.: 2015, *The Astrophysical Journal Letters* **810**, L25
- Hoeijmakers, H. J., Kok, D., J. R., Snellen, I. a. G., Brogi, M., Birkby, J. L., and Schwarz, H.: 2015, *Astronomy and Astrophysics* **575**, A20
- Horne, K.: 1986, *Publications of the Astronomical Society of the Pacific* **98**, 609, 01548
- Husser, T.-O., von Berg, S. W., Dreizler, S., Homeier, D., Reiners, A., Barman, T., and Hauschildt, P. H.: 2013, *Astronomy and Astrophysics* **553**, A6, 00243
- Kaeufl, H.-U., Ballester, P., Biereichel, P., Delabre, B., Donaldson, R., Dorn, R., Fedrigo, E., Finger, G., Fischer, G., Franz, F., Gojak, D., Huster, G., Jung, Y., Lizon, J.-L., Mehrgan, L., Meyer, M., Moorwood, A., Pirard, J.-F., Paufique, J., Pozna, E., Siebenmorgen, R., Silber, A., Stegmeier, J., and Wegerer, S.: 2004, *Ground-based Instrumentation for Astronomy* **5492**, 1218, 00000
- Kerber, F., Nave, G., Sansonetti, C. J., and Bristow, P.: 2009, *Physica Scripta* **2009**(T134), 014007, 00009
- Kolbl, R., Marcy, G. W., Isaacson, H., and Howard, A. W.: 2015, *The Astronomical Journal* **149**, 18
- Kostogryz, N., Kürster, M., Yakobchuk, T., Lyubchik, Y., and Kuznetsov, M.: 2013, *Astronomische Nachrichten* **334**(7), 648, 00000
- Ku, H. H.: 1966, *Notes on the Use of Propagation of Error Formulas*, National Bureau of Standards
- Lillo-Box, J., Leleu, A., Parviainen, H., Figueira, P., Mallonn, M., Correia, A. C. M., Santos, N. C., Robutel, P., Lendl, M., Boffin, H. M. J., Faria, J. P., Barrado, D., and Neal, J.: 2018, *arXiv:1807.00773 [astro-ph]*
- Maldonado, J. and Villaver, E.: 2017, *Astronomy and Astrophysics* **602**, A38
- Martins, J. H. C., Santos, N. C., Figueira, P., Faria, J. P., Montalto, M., Boisse, I., Ehrenreich, D., Lovis, C., Mayor, M., Melo, C., Pepe, F., Sousa, S. G., Udry, S., and Cunha, D.: 2015, *Astronomy and Astrophysics* **576**, A134
- Mathar, R. J.: 2007, *Journal of Optics A: Pure and Applied Optics* **9**(5), 470
- Meier, R. J.: 2005, *Vibrational Spectroscopy* **39**(2), 266

- Moutou, C., Vigan, A., Mesa, D., Desidera, S., Thébault, P., Zurlo, A., and Salter, G.: 2017, *Astronomy and Astrophysics* **602**, A87, 00001
- Murray, C. D. and Correia, A. C. M.: 2010, in S. Seager (ed.), *Exoplanets*, pp 15–23, University of Arizona Press, 00000
- Nemravová, J. A., Harmanec, P., Brož, M., Vokrouhlický, D., Mourard, D., Hummel, C. A., Cameron, C., Matthews, J. M., Bolton, C. T., Božić, H., Chini, R., Dembsky, T., Engle, S., Farrington, C., Grunhut, J. H., Guenther, D. B., Guinan, E. F., Korčáková, D., Koubek, P., Kříček, R., Kuschnig, R., Mayer, P., McCook, G. P., Moffat, A. F. J., Nardetto, N., Prša, A., Ribeiro, J., Rowe, J., Rucinski, S., Škoda, P., Šlechta, M., Tallon-Bosc, I., Votruba, V., Weiss, W. W., Wolf, M., Zasche, P., and Zavala, R. T.: 2016, *Astronomy and Astrophysics* **594**, A55
- Nicholls, C. P., Lebzelter, T., Smette, A., Wolff, B., Hartman, H., Käufl, H.-U., Przybilla, N., Ramsay, S., Uttenthaler, S., Wahlgren, G. M., and others: 2017, *Astronomy and Astrophysics* **598**, A79, 00000
- Passegger, V. M., Berg, S. W.-v., and Reiners, A.: 2016, *Astronomy and Astrophysics* **587**, A19, 00006
- Peck, E. R. and Reeder, K.: 1972, *JOSA* **62**(8), 958
- Pilyavsky, G., Mahadevan, S., Kane, S. R., Howard, A. W., Ciardi, D. R., de Pree, C., Dragomir, D., Fischer, D., Henry, G. W., Jensen, E. L. N., Laughlin, G., Marlowe, H., Rabus, M., von Braun, K., Wright, J. T., and Wang, X. X.: 2011, *apj* **743**, 162, 00014
- Piskorz, D., Benneke, B., Crockett, N. R., Lockwood, A. C., Blake, G. A., Barman, T. S., Bender, C. F., Bryan, M. L., Carr, J. S., Fischer, D. A., Howard, A. W., Isaacson, H., and Johnson, J. A.: 2016, *The Astrophysical Journal* **832**(2), 131
- Piskunov, N. E. and Valenti, J. A.: 2002, *Astronomy and Astrophysics* **385**(3), 1095, 00257
- Quarteroni, A., Sacco, R., and Saleri, F.: 2000, *Numerical Mathematics*, No. 37 in Texts in applied mathematics, Springer, New York
- Quirrenbach, A., Amado, P. J., Caballero, J. A., Mundt, R., Reiners, A., Ribas, I., Seifert, W., Abril, M., Aceituno, J., Alonso-Floriano, F. J., Ammler-von Eiff, M., Antona Jiménez, R., Anwand-Heerwart, H., Azzaro, M., Bauer, F., Barrado, D., Becerril, S., Béjar, V. J. S., Benítez, D., Berdiñas, Z. M., Cárdenas, M. C., Casal, E., Claret, A., Colomé, J., Cortés-Contreras, M., Czesla, S., Doellinger, M., Dreizler, S., Feiz, C., Fernández, M., Galadí, D., Gálvez-Ortiz, M. C., García-Piquer, A., García-Vargas, M. L., Garrido, R., Gesa, L., Gómez Galera, V., González Álvarez, E., González Hernández, J. I., Grözinger, U., Guàrdia, J., Guenther, E. W., de Guindos, E., Gutiérrez-Soto, J., Hagen, H.-J., Hatzes, A. P., Hauschildt, P. H., Helmling, J., Henning, T., Hermann, D., Hernández Castaño, L., Herrero, E., Hidalgo, D., Holgado, G., Huber, A., Huber, K. F., Jeffers, S., Joergens, V., de Juan, E., Kehr, M., Klein, R., Kürster, M., Lamert, A., Lalitha, S., Laun, W., Lemke, U., Lenzen, R., López del Fresno, M., López Martí, B., López-Santiago, J., Mall, U., Mandel, H., Martín, E. L., Martín-Ruiz, S., Martínez-Rodríguez, H., Marvin, C. J., Mathar, R. J., Mirabet, E., Montes, D., Morales Muñoz, R., Moya, A., Naranjo, V., Ofir, A., Oreiro, R., Pallé, E., Panduro, J., Passegger, V.-M., Pérez-Calpena, A., Pérez Medialdea, D., Perger, M., Pluto, M., Ramón, A., Rebolo, R., Redondo, P., Reffert, S., Reinhardt, S., Rhode, P., Rix, H.-W., Rodler, F., Rodríguez, E., Rodríguez-López, C., Rodríguez-Pérez, E., Rohloff,

- R.-R., Rosich, A., Sánchez-Blanco, E., Sánchez Carrasco, M. A., Sanz-Forcada, J., Sarmiento, L. F., Schäfer, S., Schiller, J., Schmidt, C., Schmitt, J. H. M. M., Solano, E., Stahl, O., Storz, C., Stürmer, J., Suárez, J. C., Ulbrich, R. G., Veredas, G., Wagner, K., Winkler, J., Zapatero Osorio, M. R., Zechmeister, M., Abellán de Paco, F. J., Anglada-Escudé, G., del Burgo, C., Klutsch, A., Lizon, J. L., López-Morales, M., Morales, J. C., Perryman, M. A. C., Tulloch, S. M., and Xu, W.: 2014, in *Proceedings of SPIE: Ground-Based and Airborne Instrumentation for Astronomy V*, Vol. 9147, p. 91471F
- Rodler, F., Lopez-Morales, M., and Ribas, I.: 2012, *The Astrophysical Journal Letters* **753**(1), L25, 00077
- Rothman, L., Gordon, I., Babikov, Y., Barbe, A., Chris Benner, D., Bernath, P., Birk, M., Bizzocchi, L., Boudon, V., Brown, L., Campargue, A., Chance, K., Cohen, E., Coudert, L., Devi, V., Drouin, B., Fayt, A., Flaud, J.-M., Gamache, R., Harrison, J., Hartmann, J.-M., Hill, C., Hodges, J., Jacquemart, D., Jolly, A., Lamouroux, J., Le Roy, R., Li, G., Long, D., Lyulin, O., Mackie, C., Massie, S., Mikhailenko, S., Müller, H., Naumenko, O., Nikitin, A., Orphal, J., Perevalov, V., Perrin, A., Polovtseva, E., Richard, C., Smith, M., Starikova, E., Sung, K., Tashkun, S., Tennyson, J., Toon, G., Tyuterev, V., and Wagner, G.: 2013, *Journal of Quantitative Spectroscopy and Radiative Transfer* **130**, 4, 01706
- Rothman, L., Gordon, I., Barbe, A., Benner, D., Bernath, P., Birk, M., Boudon, V., Brown, L., Campargue, A., Champion, J.-P., Chance, K., Coudert, L., Dana, V., Devi, V., Fally, S., Flaud, J.-M., Gamache, R., Goldman, A., Jacquemart, D., Kleiner, I., Lacome, N., Lafferty, W., Mandin, J.-Y., Massie, S., Mikhailenko, S., Miller, C., Moazzen-Ahmadi, N., Naumenko, O., Nikitin, A., Orphal, J., Perevalov, V., Perrin, A., Predoi-Cross, A., Rinsland, C., Rotger, M., Šimečková, M., Smith, M., Sung, K., Tashkun, S., Tennyson, J., Toth, R., Vandaele, A., and Vander Auwera, J.: 2009, *Journal of Quantitative Spectroscopy and Radiative Transfer* **110**(9-10), 533, 00000
- Sahlmann, J., Segransan, D., Queloz, D., Udry, S., Santos, N. C., Marmier, M., Mayor, M., Naef, D., Pepe, F., and Zucker, S.: 2011, *Astronomy and Astrophysics* **525**, A95, 00115
- Santerne, A., Brugger, B., Armstrong, D. J., Adibekyan, V., Lillo-Box, J., Gosselin, H., Aguichine, A., Almenara, J.-M., Barrado, D., Barros, S. C. C., Bayliss, D., Boisse, I., Bonomo, A. S., Bouchy, F., Brown, D. J. A., Deleuil, M., Mena, E. D., Demangeon, O., Díaz, R. F., Doyle, A., Dumusque, X., Faedi, F., Faria, J. P., Figueira, P., Foxell, E., Giles, H., Hébrard, G., Hojjatpanah, S., Hobson, M., Jackman, J., King, G., Kirk, J., Lam, K. W. F., Ligi, R., Lovis, C., Louden, T., McCormac, J., Mousis, O., Neal, J. J., Osborn, H. P., Pepe, F., Pollacco, D., Santos, N. C., Sousa, S. G., Udry, S., and Vigan, A.: 2018, *Nature Astronomy* **2**(5), 393
- Santerne, A., Díaz, R. F., Moutou, C., Bouchy, F., Hébrard, G., Almenara, J.-M., Bonomo, A. S., Deleuil, M., and Santos, N. C.: 2012, *Astronomy and Astrophysics* **545**, A76
- Santos, N. C., Adibekyan, V., Figueira, P., Andreasen, D. T., Barros, S. C. C., Delgado-Mena, E., Demangeon, O., Faria, J. P., Oshagh, M., Sousa, S. G., Viana, P. T. P., and Ferreira, A. C. S.: 2017, *Astronomy and Astrophysics* **603**, A30, 00001
- Santos, N. C., Israelian, G., and Mayor, M.: 2004, *aap* **415**, 1153, 00000
- Santos, N. C., Israelian, G., Mayor, M., Bento, J. P., Almeida, P. C., Sousa, S. G., and Ecuvillon, A.: 2005, *aap* **437**, 1127, 00000

- Schlaufman, K. C.: 2018, *The Astrophysical Journal* **853**, 37
- Schwarz, G.: 1978, *The Annals of Statistics* **6**(2), 461
- Seifahrt, A., Käufl, H. U., Zängl, G., Bean, J. L., Richter, M. J., and Siebenmorgen, R.: 2010, *Astronomy and Astrophysics* **524**, A11
- Skrutskie, M. F., Cutri, R. M., Stiening, R., Weinberg, M. D., Schneider, S., Carpenter, J. M., Beichman, C., Capps, R., Chester, T., Elias, J., Huchra, J., Liebert, J., Lonsdale, C., Monet, D. G., Price, S., Seitzer, P., Jarrett, T., Kirkpatrick, J. D., Gizis, J. E., Howard, E., Evans, T., Fowler, J., Fullmer, L., Hurt, R., Light, R., Kopan, E. L., Marsh, K. A., McCallon, H. L., Tam, R., Van Dyk, S., and Wheelock, S.: 2006, *The Astronomical Journal* **131**, 1163
- Smette, A., Sana, H., Noll, S., Horst, H., Kausch, W., Kimeswenger, S., Barden, M., Szyszka, C., Jones, A. M., Gallenne, A., Vinther, J., Ballester, P., and Taylor, J.: 2015, *Astronomy and Astrophysics* **576**, A77, 00067
- Snellen, I. A. G., Brandl, B. R., Kok, D., J, R., Brogi, M., Birkby, J., and Schwarz, H.: 2014, *Nature* **509**, 63, 00000
- Snellen, I. A. G., Kok, D., J, R., Mooij, D., W, E. J., and Albrecht, S.: 2010, *Nature* **465**(7301), 1049
- Soderblom, D. R.: 2010, *Annual Review of Astronomy and Astrophysics* **48**, 581, 00241
- Sorahana, S., Yamamura, I., and Murakami, H.: 2013, *The Astrophysical Journal* **767**(1), 77
- Sousa, S. G., Santos, N. C., Mayor, M., Udry, S., Casagrande, L., Israelian, G., Pepe, F., Queloz, D., and Monteiro, M. J. P. F. G.: 2008, *aap* **487**, 373, 00390
- Tody, D.: 1993, in R. J. Hanisch, R. J. V. Brissenden, and J. Barnes (eds.), *Astronomical Data Analysis Software and Systems II*, Vol. 52 of *Astronomical Society of the Pacific Conference Series*, p. 173, 00000
- Tsantaki, M., Sousa, S. G., Adibekyan, V. Z., Santos, N. C., Mortier, A., and Israelian, G.: 2013, *aap* **555**, A150, 00077
- Udry, S., Mayor, M., Naef, D., Pepe, F., Queloz, D., Santos, N. C., and Burnet, M.: 2002, *Astronomy and Astrophysics* **390**(1), 267, 00158
- Ulmer-Moll, S., Figueira, P., Neal, J. J., Santos, N. C., and Bonnefoy, M.: 2018, *Astronomy and Astrophysics*, in review
- Vacca, W. D., Cushing, M. C., and Rayner, J. T.: 2003, *Publications of the Astronomical Society of the Pacific* **115**(805), 389, 00000
- Wenger, M., Ochsenbein, F., Egret, D., Dubois, P., Bonnarel, F., Borde, S., Genova, F., Jasniewicz, G., Laloë, S., Lesteven, S., and Monier, R.: 2000, *Astronomy and Astrophysics Supplement Series* **143**, 9
- Whitworth, A., Bate, M. R., Nordlund, A., Reipurth, B., and Zinnecker, H.: 2007, *Protostars and Planets V* pp 459–476, 00087

Zechmeister, M., Reiners, A., Amado, P. J., Azzaro, M., Bauer, F. F., Béjar, V. J. S., Caballero, J. A., Guenther, E. W., Hagen, H.-J., Jeffers, S. V., Kaminski, A., Kürster, M., Launhardt, R., Montes, D., Morales, J. C., Quirrenbach, A., Reffert, S., Ribas, I., Seifert, W., Tal-Or, L., and Wolthoff, V.: 2018, *Astronomy and Astrophysics* **609**, A12

Zucker, S. and Mazeh, T.: 2001, *The Astrophysical Journal* **562**(1), 549, 00060